

**SYNTHESIS AND ELECTROCHEMICAL STUDY OF Pd- AND Pt-
BASED NANOSTRUCTURED MATERIALS**

A Thesis Presented to

The Faculty of Graduate Studies

Lakehead University

By

SHUAI CHEN

In partial fulfillment of the requirements for the degree of

Master of Science

August 2011

© Shuai Chen, 2011

ProQuest Number: 10611950

All rights reserved

INFORMATION TO ALL USERS

The quality of this reproduction is dependent upon the quality of the copy submitted.

In the unlikely event that the author did not send a complete manuscript and there are missing pages, these will be noted. Also, if material had to be removed, a note will indicate the deletion.



ProQuest 10611950

Published by ProQuest LLC (2017). Copyright of the Dissertation is held by the Author.

All rights reserved.

This work is protected against unauthorized copying under Title 17, United States Code
Microform Edition © ProQuest LLC.

ProQuest LLC.
789 East Eisenhower Parkway
P.O. Box 1346
Ann Arbor, MI 48106 - 1346

Abstract

We are currently facing climate change and global warming effects due to the emission of greenhouse gases from our existing energy sources. Proton exchange membrane fuel cells are one of the most efficient alternatives for power generation with the potential for greater than 80% efficiency in combined heat and power systems. Pd- and Pt-based catalysts are deemed to hold great potential in many aspects of energy conversion; from the purification and storage of hydrogen as palladium metal hydride (PdH_x), to harnessing clean energy via fuel cells. In this M.Sc. study, Pd and Pt-based nanomaterials have been synthesized and examined to elucidate their applications in hydrogen storage and for fuel cell catalysis. The surface properties of the synthesized Pd and Pt-based nanomaterials were characterized by scanning electron microscopy (SEM), energy dispersive X-ray spectrometry (EDS), X-ray diffraction (XRD), and X-ray photoelectron spectroscopy (XPS). Electrochemical analysis of the fabricated nanomaterials was performed using cyclic voltammetry (CV), linear sweep voltammetry (LSV), chronoamperometry (CA), and electrochemical impedance spectroscopy (EIS).

Novel nanoporous Pd-Ag electrocatalysts were synthesized utilizing a facile hydrothermal method. The Ag content of the Pd-Ag alloy varied from 0 to 40%. EDS, XPS and inductively coupled plasma (ICP) were used to directly and indirectly characterize the composition of the formed Pd-Ag nanostructures. XRD analysis confirmed that the Pd-Ag nanomaterials were alloys that contained a face-centered cubic structure. The nanoporous Pd-Ag alloy having 20% Ag possessed the highest capacity for α phase hydrogen sorption, which was shown to be four times higher than that of pure nanoporous Pd. The combination of enhanced α phase hydrogen sorption capacity and the diminishment of α and β -phase transitions make these nanoporous Pd-

Ag alloys promising for enabling enhanced hydrogen selective membranes and as hydrogen dissociation catalysts.

The facile synthesis of titanium dioxide nanotube (TiO_2 NT) materials via the anodization of titanium is attractive due to its low cost, high surface area and high stability. Palladium deposited on TiO_2 NT (TiO_2 NT/Pd) electrode was synthesized via a photo-reduction method. The deposition of Pd on Ti plates was accomplished by using a hydrothermal method. Comparative studies were conducted in order to quantify the electro-hydrogen sorption behaviors and stabilities of these two electrodes. The results indicated that the TiO_2 NT/Pd possessed prominent activity and had high stability for enabling hydrogen storage.

Highly ordered TiO_2 nanotubes (TiO_2 NTs) were synthesized by anodization and were employed as substrates because of their high surface area. Pure Pt and a series of ultrafine Pt-Au nanoparticle catalysts of different compositions were loaded onto the TiO_2 NTs using a photo-assisted dispersal/deposition method. The fabricated Pt and Pt-Au catalysts were characterized by SEM, EDS, XPS and XRD. The activity of these electrocatalysts toward the oxidation of formic acid was investigated utilizing CV, LSV, CA and EIS. These investigations demonstrated that Pt-Au33% and Pt-Au50% exhibited very high electrocatalytic activity in the oxidation of formic acid, where dehydrogenation is the dominant reaction pathway in the oxidation process.

Acknowledgements

I would like to first thank my supervisor, Dr. Aicheng Chen, for all of his knowledge and advice throughout the course of my M. Sc. degree. He has supported me in all of my research and has given me the tools and confidence required for a future in this field. I would also like to thank my committee members, Dr. Floriano and Dr. MacKinnon, for their feedback on my thesis.

An extended thank you is necessary for the entire Lakehead University Chemistry Department and to Graduate Studies. Thank you also to Al MacKenzie for his assistance in the Lakehead University Instrumentation Lab. The Surface Interface Ontario / Chemical Engineering & Applied Chemistry at the University of Toronto must also be acknowledged for carrying out the XPS analysis.

All my fellow lab members of Dr. Chen's research group, former and current, deserve a special acknowledgement. This includes Dr. Min Tian, Dr. Guosheng Wu, Jiali Wen, Dr. Rasha Tolba, Brian Adams, Asieh Ahmadalinezhad, Robert Matt Asmussen, Paul Benvenuto, Rachelle Laurin, Monika Malig, Nelson Matyasovszky, Samantha Nigro, Cassandra Ostrom, Ke Pan, Xiao Qu, Matthew Simko, and Sapanbir Thind.

Lastly, I would like to extend my appreciation to my family, especially my husband, Xiao Qu, and friends for always being supportive in my decisions, and helping me through any hard times that I have encountered.

List of Abbreviations and Symbols

Abbreviation Name

A	Ampere
AFC	Alkaline Fuel Cell
CA	Chronoamperometry
CPE	Constant Phase Element
CV	Cyclic Voltammetry
DEFC	Direct Ethanol Fuel Cell
DFAFC	Direct Formic Acid Fuel Cell
DMFC	Direct Methanol Fuel Cell
E	Potential
EDS	Energy Dispersive Spectroscopy
EIS	Electrochemical Impedance Spectroscopy
FWHM	Full Width at Half Maximum
ICE	Internal Combustion Engine
ICP	Inductively Coupled Plasma
j	Current Density
LSV	Linear Sweep Voltametry
NT	Nanotube

MCFC	Molten Carbonate Fuel Cell
PAFC	Phosphoric Acid Fuel Cell
PEMFC	Proton Exchange Membrane Fuel Cell
SCE	Saturated Calomel Electrode
SEM	Scanning Electron Microscopy
SOFC	Solid Oxide Fuel Cell
XPS	X-ray Photoelectron Spectroscopy
XRD	X-ray Diffraction

Table of Contents

Abstract.....	I
Acknowledgements	III
List of Abbreviations and symbols.....	IV
Table of Contents.....	VI
Chapter 1 Introduction	1
1.1 Proton exchange membrane fuel cell.....	1
1.2 Hydrogen storage and purification.....	5
1.3 Pd-based materials for hydrogen sorption and purification	12
1.4 Pt-based and Pd-based electrocatalysis for DFAFC	16
1.5 Scope of this thesis.....	20
Reference.....	21
Chapter 2 Experimental methods	27
2.1 Introduction.....	27
2.2 Chemicals and materials	27
2.3 Fabrication of nanomaterials.....	28
2.4 Surface analysis.....	29
2.5 Electrochemical experiments	30
2.6 Summary	30
References	30
Chapter 3 Synthesis and electrochemical study of nanoporous Pd-Ag alloys for hydrogen sorption	31
3.1 Introduction.....	31

3.2	Experimental Section	33
3.3	Surface morphology, composition, and structure of the prepared Pd-Ag electrodes	34
3.4	General cyclic voltammetric (CV) behaviour of the Pd-Ag nanostructures	40
3.5	Sweep rate dependence of hydrogen electrosorption in the Pd-Ag nanostructures	42
3.6	Influence of the electrode potential and the composition of the Pd-Ag alloys on the capacity of hydrogen electrosorption	42
3.7	Dependence of hydrogen sorption time on the electrode potential and composition of Pd-Ag	47
3.8	Conclusions	49
	References	50
Chapter 4	Hydrogen Electrosorption into Palladium Nanoparticles Deposited on TiO ₂ Nanotubes	54
4.1	Introduction	54
4.2	Experimental Section	55
4.3	Characterization of synthesized Ti/Pd and TiO ₂ NT/Pd materials	56
4.4	General cyclic voltammetric (CV) behaviour of the Pd nanostructures	59
4.5	Stability test of Ti/Pd and TiO ₂ NT/Pd	67
4.6	Conclusion	72
	Reference	72
Chapter 5	Electrocatalytic activity of Pt–Au nanoparticles supported on TiO ₂ nanotube arrays	75

5.1	Introduction	75
5.2	Experimental section	77
5.3	Surface morphology and compositions of Pt-Au catalysts	79
5.4	Electrochemistry of the Pt and Pt-Au nanocatalysts	84
5.5	Electro-oxidation of formic acid on Pt and Pt-Au	86
5.6	Conclusion	93
Chapter 6	Summary and future work	97
6.1	Hydrogen Electrosorption into Pd-Ag nanostructures	97
6.2	Hydrogen sorption in TiO ₂ NT/Pd	98
6.3	Electrochemical activity of TiO ₂ NT/Pt-Au	98
6.4	Closing remarks and future work	99

Chapter 1 Introduction

1.1 Proton exchange membrane fuel cell

A fuel cell is an electrochemical energy conversion device. It produces electricity from external supplies of fuel on the anode side and oxidant on the cathode side. Fuel cells can operate virtually continuously as long as the necessary fuel and flows are maintained.¹⁻⁴

Fuel cells offer several benefits for applications in transportation, stationary, and portable power. One of the major benefits is an increase in efficiency over conventional technologies. Fuel cells are more than twice as efficient as internal combustion engines (ICEs), with the potential for greater than 80% efficiency in combined heat and power systems.¹⁻³

Fuel cells may be grouped by the type of electrolytes that they utilize, namely: alkaline fuel cells (AFC), polymer electrolyte membrane or proton exchange membrane fuel cells (PEMFC), phosphoric acid fuel cells (PAFC), molten carbonate fuel cells (MCFC) and solid oxide fuel cells (SOFC).⁵ Table 1.1 depicts the general characteristics of five types of fuel cells. Proton exchange membrane fuel cells may also be classified by the type of fuels that they use, namely: hydrogen fuel cell, direct methanol fuel cell (DMFC), direct ethanol fuel cell (DEFC) and direct formic acid fuel cell (DFAFC), which use hydrogen, methanol, ethanol and formic acid as fuels, respectively.¹ Proton exchange membrane fuel cells are compact and lightweight, work at low temperatures with a high output power and low environmental impact, and offer superior system startup and shutdown performance. These advantages have sparked development efforts in various sectors of industry to open up new application areas encompassing stationary power,

portable supplies, and emergency and disaster backup power supplies.¹ Here, proton exchange membrane fuel cells (e.g., hydrogen fuel cell and DFAFC) are mainly introduced.

Table 1.1 General characteristics of five types of fuel cells⁶

	PEMFC	AFC	PAFC	MCFC	SOFC
Primary Applications	Automotive and stationary power	Space vehicles and drinking water	Stationary power	Stationary power	Vehicle auxiliary power
Electrolyte	Polymer (plastic) membrane	Concentrated (30-50%) KOH in H ₂ O	Concentrated 100% phosphoric acid	Molten Carbonate retained in a ceramic matrix of LiAlO ₂	Yttrium-stabilized Zirkondioxide
Operating Temperature Range	50-100 °C	50-200 °C	150-220 °C	600-700 °C	700-1000 °C
Charge Carrier	H ⁺	OH ⁻	H ⁺	CO ₃ ²⁻	O ₂ ⁻
Catalysts	Pt-based	Pt-based	Pt-based	Ni-based	Perovskites
Primary Fuel	H ₂	H ₂	H ₂	H ₂ , CO, CH ₄	H ₂ , CO
Start-up Time	Sec-min	Sec-min	Hours	Hours	Hours
Power Density (kW/m ³)	3.8-6.5	~1	0.8-1.9	1.5-2.6	0.1-1.5
Combined Cycle Efficiency	50-60%	50-60%	55%	55-65%	55-65%

1.1.1 Hydrogen fuel cell

Hydrogen fuel cells are regarded as one of the most promising classes of fuel cells for light-duty applications, such as the provision of power for vehicles.⁷ Figure 1.1 illustrates the principle of operation of a hydrogen fuel cell. Humidified air enters the cathode channel, and hydrogen gas enters the anode channel.¹ The hydrogen diffuses through the anode diffusion layer toward the catalyst layer, where each hydrogen molecule is split into two protons and two electrons at the catalyst surface according to



The protons then migrate through the membrane and the electrons travel through the conductive diffusion layer and to an external circuit where they produce electrical current. On the cathode side the oxygen diffuses through the diffusion layer, splits up at the catalyst layer surface and reacts with both the protons and electrons to form water:



Reaction 1.1 is slightly endothermic, whereas reaction 1.2 is heavily exothermic. Hence, there is a resultant generation of heat. From the above it can be seen that the overall reaction of the hydrogen fuel cell may be written as:



Hydrogen is not an energy source, but rather an energy carrier, which means that it stores and delivers energy in a usable form. The attraction of using hydrogen as an energy currency is that, if hydrogen is prepared without the use of fossil fuel inputs, vehicle propulsion does not

contribute to the emission of carbon dioxide. In addition, hydrogen generates the highest level of electrochemical performance. High-purity hydrogen continues to receive increasing attention as a promising energy carrier for fuel cells in portable power applications. However, hydrogen storage and purification remain as dual primary challenges for the portable application of hydrogen fuel cells.⁸ More details on this will be discussed in Section 1. 2.

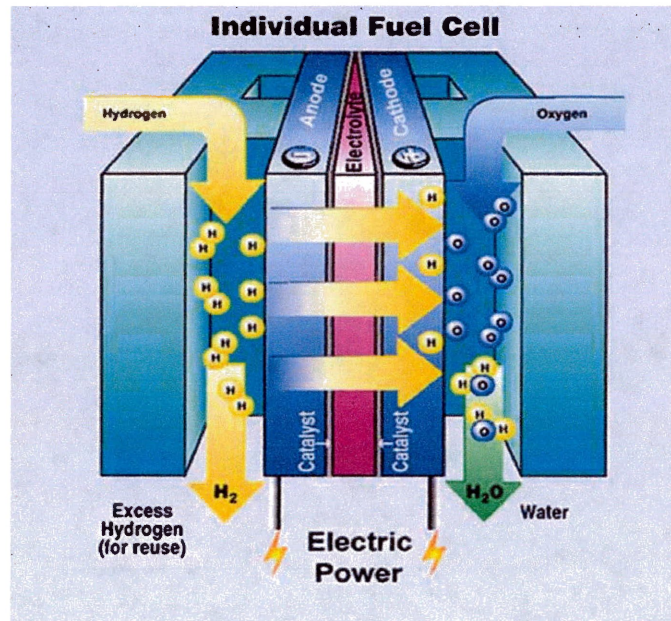


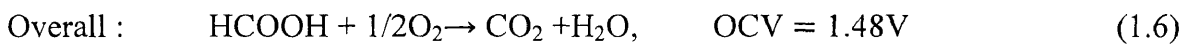
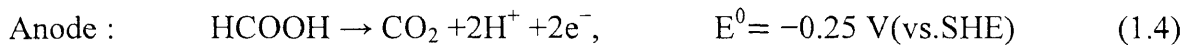
Fig.1.1 Scheme of the operational principles of hydrogen fuel cell.⁹

1.1.2 Direct formic acid fuel cell

Direct formic acid fuel cells are generally considered as preferred alternatives for the replacement of batteries in portable power devices.¹⁰⁻¹¹ Toward this end, most DFAFCs are designed as small modular and portable units. The demand for power sources with superior performance has increased as a result of the rapid growth of the portable electronics market. There is significant potential for micro-fuel cells to deliver more energy per volume and weight

than conventional batteries. DFAFCs appear to be attractive candidates for meeting increasing power density demands. With the advantages of high electromotive force, limited fuel crossover, and high practical power densities at low temperature, DFAFCs are very promising power devices for the near future.¹²⁻¹⁵

The cathode, anode and overall reactions of a direct formic acid fuel cell are described as:



The direct formic acid fuel cell exhibits an enhanced electromotive force (EMF) (open circuit voltage (OCV) = 1.48 V.¹⁶⁻¹⁷ The theoretical energy density of formic acid is determined as: $2F \times \text{OCV} \times (\text{MW})^{-1}$. From the molecular weight MW (kg mol^{-1}), open circuit potential OCV (V) and the Faraday constant ($F = 96,485 \text{ C mol}^{-1}$), formic acid has an intrinsic energy density of 1725 Wh kg^{-1} .¹⁸⁻¹⁹ Considering the density of this liquid (1.22 kg L^{-1}), the theoretical energy density of formic acid may also be expressed as 2104 Wh L^{-1} .^{16,19} In a DFAFC system, catalysts with high activity are required for both the anode and cathode in order to achieve superior performance.²⁰⁻²²

1.2 Hydrogen storage and purification

1.2.1 Hydrogen as a fuel

Owing to an increasing world population and the demand for higher standards of living and better air quality, future energy demands are expected to increase exponentially.⁷ Addressing this

demand will pose great challenges.⁷ Currently, most of the world energy requirement for transportation and heating (which comprises two-third of principal energy demands) is derived from petroleum or natural gas.^{7,23} These two fuels are generally favored due to their ease of transport in either liquid or gaseous forms. Unfortunately, the combustion of hydrocarbon fuels for transportation and heating contributes to over half of all greenhouse gas emissions and a large fraction of air pollutant emissions. Hence, today's world is facing a critical urgency for the development of alternative fuels. Among various alternatives, hydrogen fuel offers the most optimal potential benefits in terms of diversified supply and for the reduction of aerosolized pollutants and greenhouse gas emissions.²³

Hydrogen has the highest energy content per unit mass of any fuel.²³⁻²⁴ For example, on the basis of weight, hydrogen has nearly three times the energy content of gasoline (140.4 MJ/kg versus 48.6 MJ/kg).²⁵ Therefore, one of the important and attractive features of hydrogen is its electrochemical properties, which can be utilized in a fuel cell. At present, H₂/O₂ fuel cells are available that operate at efficiencies of 50–60% with a lifetime of up to 3000h. Current outputs range from 440 to 1720 A/m² at the electrode surface, which may generate a power output that spans from 50 to 2500 W. However, on the basis of volume the situation is reversed with 8,491 MJ/m³ for liquid hydrogen versus 31,150 MJ/m³ for gasoline.^{7,26} The low volumetric density of hydrogen results in storage problems, particularly for automotive applications.²⁶⁻²⁷

1.2.2 Hydrogen storage

The development of a hydrogen-based economy is contingent on the development of safe and cost-effective hydrogen storage systems. Several studies have been published that describe the storage of hydrogen using different techniques.^{26,28-36} Hydrogen storage is a key element in the

utilization of hydrogen fuel. However, as relates to the use of fuel in vehicles, hydrogen storage remains as the chief technical challenge. Present storage techniques for hydrogen include compressed gas, cryogenic liquid and absorption on solids.

Hydrogen exists as a molecular gas. At room temperature and atmospheric pressure, 4 kg of hydrogen occupies a volume of 45 m³. This corresponds to a balloon of 5 m in diameter, which is hardly a practical solution for powering a vehicle.²³ However, in consideration of both current storage and refueling technologies, the most promising short-term alternative is likely to be compressed gas storage.²³

The storage of hydrogen in liquid form under cryogenic conditions is attractive in that it offers low weight and volume per unit energy in comparison to compressed hydrogen.⁷ The major issues with liquid hydrogen storage tanks are hydrogen boil-off, the amount of energy that is required for hydrogen liquefaction, and tank cost. Liquid hydrogen must be stored at 20 K (-253°C). Storage tanks have to be insulated to preserve temperature, and are required to be reinforced to store the liquid hydrogen under some pressure. The total fuel cycle energy efficiency is significantly lower for liquid hydrogen than for gaseous hydrogen due to the large amount of energy that is required for liquefaction. The total theoretical amount of energy required for liquefaction is approximately 3.4 MJ/kg, whereas the actual amount of energy required for liquefaction is much higher, approximately 50.4 MJ/kg, with a refrigeration efficiency of 7.2%. Overall, liquefaction results in a loss of about 30% of the energy that is stored within liquid hydrogen.⁷

Metal hydrides are specific combinations of metallic alloys that possess the ability to absorb and retain hydrogen, which may be later released, either at room temperature or upon heating.^{31,37}

The total amount of hydrogen absorbed is generally 1–2 wt% of the total weight of the tank. However, some metal hydrides are capable of storing 5–7 wt%. The percentage of gas absorbed to the volume of the metal is still relatively low. Nevertheless, hydrides offer a valuable solution to hydrogen storage. Although the volume of this storage device is only two-fold greater than an equivalent gasoline tank, it is unfortunately 20-fold heavier. The alloys act as a sponge, which absorbs large amounts of hydrogen, but in the process it may also absorb any impurities that are introduced into the tank via the hydrogen.

By utilizing hydrogenation and dehydrogenation cycles of organic compounds, organic chemical hydrides can achieve the storage of hydrogen.³⁸⁻⁴² Examples include organic chemical hydrides that consist of reversible catalysis pairs such as decalin dehydrogenation/naphthalene hydrogenation and tetralin dehydrogenation / naphthalene hydrogenation.⁴³⁻⁴⁶ Decalin has the capacity to store hydrogen at high capacities (7.3 wt%, 64.8 kg H₂/m³). Decalin and naphthalene are accepted by the public as safe commodity chemicals since they have long been domestically utilized in solvents and insect killers, respectively. However, the energy and equipment requirements for the dehydrogenation reaction are too expensive for onboard use. Organic chemical hydrides are considered as more suitable for hydrogen storage and dispensing at the fueling station.

1.2.3 Hydrogen purification

A large percentage of H₂ is used for large-scale processes in the metallurgical, chemical, petrochemical, pharmaceutical and textile industries to manufacture a diverse range of products, from semiconductors and steel alloys, to vitamins and raw chemical materials such as ammonia, methanol, and hydrogen peroxide. However, the large-scale production of H₂ for these industries

often requires an almost prohibitively large capital investment for the separation and purification processes, which significantly drive up the cost of H₂.⁴⁷ Regardless of which method is employed in the production of H₂, the need will always exist for a cost effective and efficient means for separating it from other, less desirable species. Currently, H₂ may be purified through one (or a combination) of three major processes: (1) pressure swing adsorption (PSA), (2) fractional/cryogenic distillation, or (3) membrane separation.⁴⁷ While PSA and fractional/cryogenic distillation systems are in commercial operation, they are generally not cost effective and are quite energetically demanding for the separation and purification of H₂. In addition, neither of these methods provides a level of purity that is sufficient for the targeted applications in the hydrogen economy. The third method, membrane separation, is currently considered to be the most promising due to low energy consumption, the potential for continuous operation, dramatically lower investment costs, ease of operation, and ultimately, cost effectiveness.⁴⁷

Within the domain of gaseous H₂ separations, membrane compositions span the entire periodic table and range from metallic alloys and organic polymers to inorganic oxides and composites. Classified by composition, membranes are delineated as follows: metallic (pure metals or alloys), inorganics (including oxides, zeolites, glasses, and ceramics), porous carbons, pure organic polymers, and hybrids or composites.⁴⁷⁻⁴⁸

Metallic membranes are typically dense sheets or films through which H₂ permeates in the form of its constituent protons and electrons.⁴⁸⁻⁴⁹ The fundamental kinetic mechanism within these dense metallic membranes requires the conduction of free electrons and the presence of specific catalytic surfaces to dissociate the H₂ on the raw feed stream side, and the re-association of the protons and electrons on the product side. Hydrogen selectivity is typically very high in these

systems, since the dense structure prevents the passage of large atoms and molecules such as CO, CO₂, O₂, and N₂. This enhanced selectivity translates to very high purity H₂ and the increased thermal stabilities allow for higher operating temperatures. These are the primary advantages that metallic membranes offer over other materials. The metals that are most suitable for H₂ separation membranes typically have high H₂ permeability, high diffusivities or solubility, and good stability at elevated temperatures. These include, but are not exclusively limited to tantalum, niobium, vanadium, platinum and palladium. Historically, H₂ separations were performed with Pd-based membranes, since they naturally catalyze the surface dissociation/re-association processes and are highly permeable to H₂. There is extensive information in the literature regarding the many years of research into Pd membranes.⁴⁷

Inorganic membranes, which have good thermal stability and chemical inertness, have advantages over polymeric membranes for many industrial applications.^{47,50-51} Improved membrane integrity and manufacturing costs are constant factors which are the focus of numerous research efforts. Zeolite membranes, in particular, combine pore size and shape selectivity with the inherent mechanical, thermal, and chemical stability that is necessary for continuous long-term separation processes. The effective pore size distribution of the zeolite membrane, and hence its separation performance, is intrinsically governed by the selection of the zeolitic phase(s). Gas and liquid separation using zeolite membranes is primarily governed by competitive adsorption and diffusion mechanisms. When the zeolite pore size distribution falls between the molecular sizes of the feed components, a size exclusion mechanism can dominate the separation process. However, one of the main challenges in zeolite membrane development is the minimization of intercrystal pores that are inherently formed within polycrystalline zeolite films. The existence of intercrystal pores with dimensions larger than the zeolitic pores is the

major cause of decline in molecular separation efficiency. The elimination of intercrystalline pores is essential for the attainment of high separation selectivity, which is viable for industrial applications.

Hydrogen rejection and contaminant permeation is being intensely explored as a new approach for H₂ purification through the use of carbon-based membranes.⁴⁷ Because of hydrogen's low critical temperature and small kinetic diameter, a rejective membrane process allows for H₂ purification via contaminant permeation with respect to H₂. Carbon membranes have a very distinct economic advantage in that maintaining/collecting H₂ in the retentate reduces the necessity for costly H₂ recompression steps. Therefore, they may only find utility in certain limited applications, such as the use of H₂ in refineries, where only low or medium pressure hydrogen is required. In addition, non-polymeric carbon-based membranes are rejective H₂ membranes that may be categorized into three classes: carbon membranes, carbon molecular sieve membranes (CMSMs), and carbon nanotubes (CNTs). The separation ability of each class of material is dependent both on the chemistry of the material and on the particulars of fabrication and implementation (ie., module design).

Though carbon-based membranes show much promise in the area of light gas separations, there remain a number of issues that hinder their introduction to the marketplace. First, they are very brittle and fragile, and therefore require more careful handling. This may be avoided to a certain degree by optimizing precursors and preparation methods. Second, processing complexities translate to high fabrication costs. Carbon membranes require a pre-purifier for the removal of strongly adsorbing residual vapors that can clog up pores. This is a critical factor as the membrane transport proceeds through pores rather than through the bulk system. This is typical of many industrial adsorption separators.

Polymeric membranes which are selective for hydrogen operate at temperatures of ~ 100 °C and are designed such that the concentration of hydrogen is increased in the product stream. The remaining components of the gas mixture remain in the feed stream or are diverted to a secondary waste stream. Dense polymeric membranes may be divided into glassy and rubbery classes.⁵² The former have higher selectivity and lower flux, whereas the latter have higher flux but lower selectivity. Their key advantages include low cost, and that they possess the ability to cope with high-pressure drops. However, limited mechanical strength, relatively high sensitivity to swelling and compaction, and susceptibility to certain chemicals such as hydrochloric acid (HCl), sulfur oxides (SO_x), and CO₂ make polymeric membranes less attractive.

1.3 Pd-based materials for hydrogen sorption and purification

Hydrogen absorbing materials are important in hydrogen storage, metal-hydride batteries, and for hydrogen purification. These materials are usually metals and complex alloys that are optimized for practical use. Palladium is a metal which can absorb a large quantity of hydrogen. The palladium-hydrogen system has been studied extensively in the gas phase; however, the electrochemical conditions are more complex. In practical applications, diffusion, solubility, physical stability, and the kinetics of hydrogen adsorption/absorption processes determine the utility of hydrogen absorbing materials. Palladium can be used as a simple model to study the fundamental properties of hydrogen absorbing materials and to better understand the mechanisms and kinetics of hydrogen adsorption and its entry into metals. It is possible to investigate these processes by electrochemical techniques and to determine the thermodynamic and kinetic parameters of hydrogen adsorption-absorption and evolution reactions in the Pd/H system.

1.3.1 Pd-based materials for hydrogen sorption

Shown in table 1.2 are intermetallic compounds and their hydrogen-storage properties.²³ Only Pd can absorb hydrogen at ambient temperature and pressure even though its hydrogen capacity is not high. Pd, a classical hydrogen-storage metal, exhibits exceptional features for practical use. Specifically, it can be used as a catalyst for hydrogen sorption and desorption.

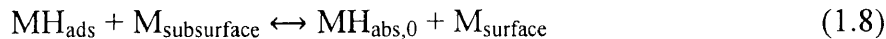
Table 1.2 intermetallic compounds and their hydrogen-sorption properties.²³

Type	Metal	Hydride	Structure	wt.% H	P _{eq} , T
Elemental	Pd	PdH _{0.6}	Fm3m	0.56	0.02 bar, 298
AB ₅	LaNi ₅	LaNi ₅ H ₆	P6/mmm	1.37	2 bar, 298 K
AB ₂	ZrV ₂	ZrV ₂ H _{5.5}	Fd3m	3.01	10-8 bar, 323
AB	FeTi	FeTiH ₂	Pm3m	1.89	5 bar, 303 K
A ₂ B	Mg ₂ Ni	Mg ₂ NiH ₄	P6222	3.59	1 bar, 555 K
Body-centered cubic	TiV ₂	TiV ₂ H ₄	b.c.c.	2.60	10 bar, 313 K

The Pd–H system has been studied for years but there remains no agreement as to the detailed mechanism of the absorption reaction. Typically, hydrogen atoms are considered to enter the metal either by a two-step or a direct absorption mechanism.⁵³⁻⁵⁵ The equations below are written under the assumption of a two-step absorption mechanism from an acidic solution. Hydrogen is initially adsorbed on the Pd metal surface (M) of an electrode in the Volmer step:



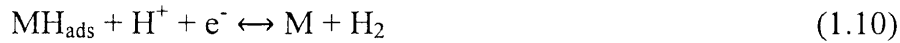
followed by absorption in the subsurface layer at a distance $x = 0$ from the interface:



Where $M_{\text{subsurface}}$ and M_{surface} are the empty subsurface and surface sites, and the subsequent diffusion into the bulk of the metal:



Of course, there may be parasitic reactions such as hydrogen evolution, HER, according to the Heyrovsky:



or Tafel reactions:



Hydrogen occupies the octahedral interstices of the lattice of Pd. The consequence of the entry of hydrogen into a metal is the expansion of the lattice. At low concentrations, hydrogen forms solid Pd-H solutions at the α -phase ($nH/nPd < 0.025$), whereas at high concentrations it forms a β phase ($nH/nPd > 0.300$), which is palladium hydride. Phase transitions occur due to the new arrangement of the absorbed/desorbed hydrogen in the Pd lattice and changes in the electronic properties of the Pd atoms. Fig.1.2 illustrates a schematic model of a metal structure with H atoms in the interstices between the metal atoms, and H_2 molecules at the surface.²³ Hydrogen atoms are shown as being supplied by physisorbed hydrogen molecules on the left-hand side and from the dissociation of water molecules on the right-hand side.²³

However, the use of Pd as the sole metal hydride for hydrogen storage is not practical because of its high cost and hydrogen embrittlement that is caused by the phase transition from α to β that takes place within pure palladium. Pd-based alloys, on the other hand, serve as an attractive class of materials for the study of metal hydrides due to the high solubility and permeability of

hydrogen in comparison to pure Pd, as well as the reduced cost via the addition of cheaper metals.

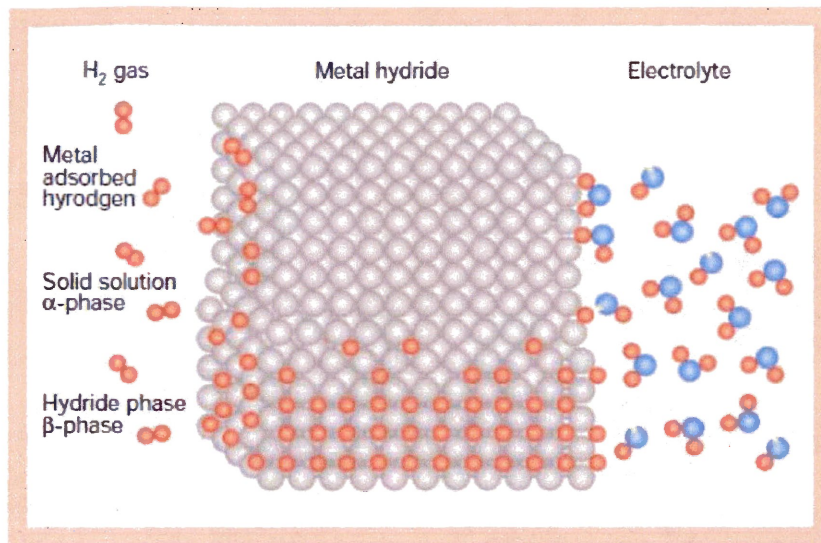


Fig.1.2 Schematic model of a metal structure with H atoms in the interstices between the metal atoms, and H₂ molecules at the surface.²³

Pd-alloys may be reversibly loaded with hydrogen for study in both the gas phase and under electrochemical conditions. Extremely large currents generated by the electrochemical absorption and desorption of hydrogen in bulk Pd (wires or foils) can be avoided by utilizing so-called “limited volume electrodes” (LVEs). These LVEs consist of a thin layer of Pd or Pd-alloy that is deposited onto a matrix, such as gold, which does not absorb hydrogen. LVEs allow for the control of the amount of absorbed hydrogen in the thin layer. Pd and various Pd alloys, including PdPt⁵⁶, PdRh⁵⁷, PdNi⁵⁸, and PdCd³⁴ have been studied using this approach.

1.3.2 Pd-based materials for hydrogen purification

In a dense metallic membrane, H₂ permeates the solid material via the solution diffusion mechanism involving a total of seven steps, which are illustrated in Fig.1.3.⁴⁷ Pure palladium

becomes brittle in the presence of hydrogen during thermal cycling due to dimensional changes caused by a transformation between the two phases (α and β) of palladium hydride at $\sim 300^\circ\text{C}$.⁵⁹⁻

⁶² To avoid metal embrittlement and resultant membrane cracking or distortion, pure palladium membranes should not be exposed to hydrogen at temperatures below 300°C . To increase the resistance to embrittlement, Pd is alloyed with other metals such as Ag and Cu. The most commonly employed alloy in the commercially available membrane modules contains 23% Ag and 77% Pd by weight; this composition is also claimed to maximize the hydrogen permeability of the Pd–Ag alloy.⁴⁸

1.4 Pt-based and Pd-based electrocatalysis for DFAFC

The high energy density and rapid kinetics inherent to liquid fuels, in conjunction with, the convenient usage and simplicity of power system integration, make direct liquid fuel cells (DLFCs) a promising power source for portable device applications.⁶³ Among the various types of liquid fuels, formic acid has emerged as a promising candidate due to its superior oxidation kinetics, high theoretical thermodynamic cell potential and reduced propensity for fuel crossover problems, which are associated with fuel cell systems. The development of electrocatalysts for the oxidation of formic acid and the investigation of the reaction mechanism and kinetics on single crystal catalyst surfaces are necessary prerequisites to the wide implementation of DFAFC in portable devices. In addition, research efforts are required in order to devise strategies for the reduction of poisoning materials such as CO. The modification of noble metal catalyst surfaces and the development of non-Pt based electrocatalysts comprise two fundamental approaches toward increasing the durability and reducing the overall cost of DFAFC devices.

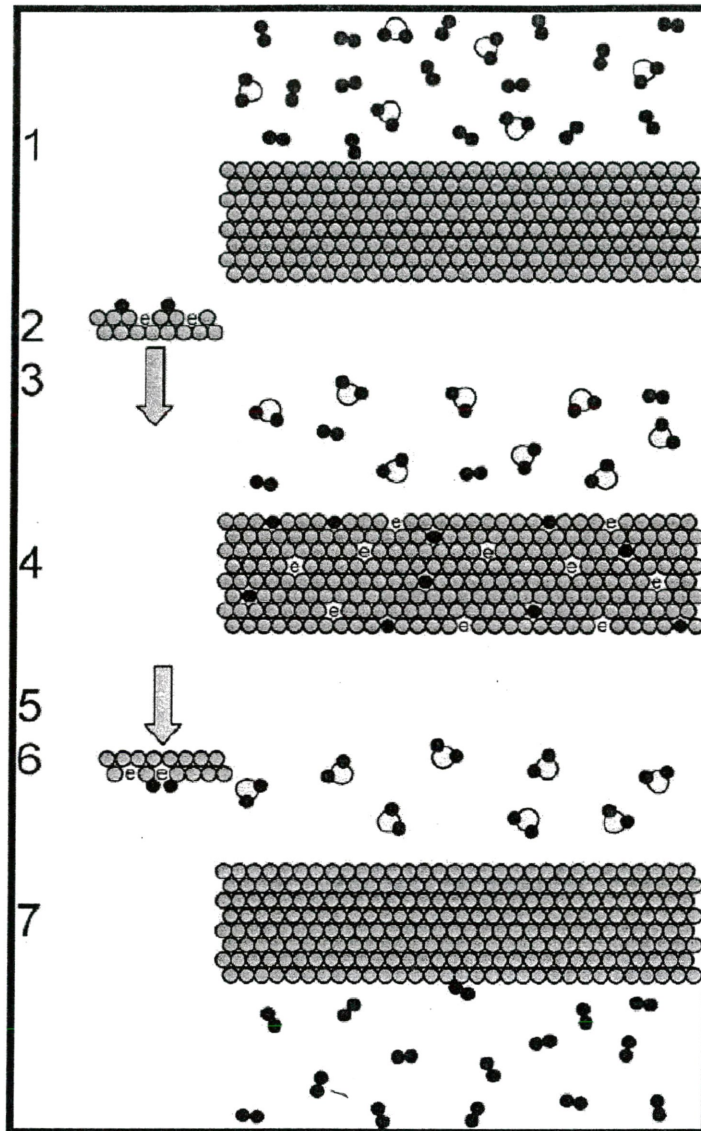
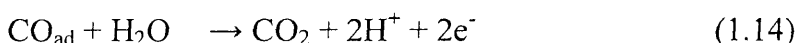
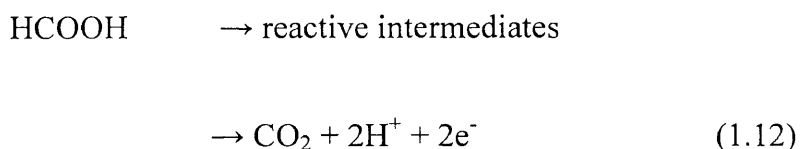


Fig.1.3 Seven-step diffusion mechanism in dense metal phases: (1) movement of the raw gas (mixture of H_2 and undesired elements) to the feed stream surface of the membrane; (2) dissociation of chemisorbed H_2 into hydrogen ions (H^+) and electrons (e^-); (3) adsorption of H^+ ions into the bulk of the membrane; (4) diffusion of the H^+ ions and electrons through the membrane; (5) desorption of H^+ ions from the bulk of the membrane to the product stream surface of the membrane; (6) reassociation of the H^+ ions and the electrons into discrete molecules of H_2 ; and, finally, (7) diffusion of the H_2 from the product surface of the membrane.⁴⁷

1.4.1 Pt-based electrocatalyst

In the early stages of DFAFC development, Pt-based catalysts were employed in the anode layer. The first report of a DFAFC, by Weber et al., found that formic acid was electrochemically more active than methanol on both Pt-black and Pt/Ru catalysts.¹⁰

The mechanism of formic acid electro-oxidation on Pt is well-established in the literature.⁶⁴⁻⁶⁸ It is generally accepted that the electrocatalytic oxidation of HCOOH to carbon dioxide (CO₂) on a metal surface proceeds via a dual path mechanism; the direct oxidation reaction (1.12) of reactive weakly-adsorbed intermediates to form CO₂ in parallel with an indirect oxidation reaction (1.13 and 1.14) pathway involving formic acid dehydration and the subsequent electrooxidation of the resultant strongly adsorbed carbon monoxide (CO) to CO₂.^{22,63}



Pt is easily poisoned by reactive intermediates and CO, which significantly reduce the Pt electrocatalytic performance at low potentials.

Pt-based bimetallic electrocatalysts demonstrate enhanced activities in comparison to pure Pt in formic acid electro-oxidation reactions.^{12,15,67-71} Pt-Ru exhibits enhanced activity relative to Pt at potentials above 0.35 V vs RHE.⁶⁴ The effect of Ru was rationalized as arising from the bifunctional action of Pt and Ru sites.²² Au and Ir have been suggested as promising alloys for

the enhancement of formic acid oxidation by reducing poison formation due to the so-called “third body effect”. This effect is based on the role of second metals (or adatoms) in the blockage of surface sites where side reactions generate poisonous species, or in blocking the adsorption of inhibiting species, which require more than one surface site for adsorption. Au is one of the most promising elements in that it has a higher tolerance against CO poisoning and a corresponding superior electrocatalytic activity for the oxidation of formic acid.⁷²

1.4.2 Pd-based electrocatalysts

The electro-oxidation of formic acid on Pd catalysts has been extensively studied.⁷³⁻⁷⁴ In comparison to Pt-based catalysts, Pd-black generated unusually high power densities at ambient (22 °C) and higher (30–50°C) temperatures.¹⁰ The activity of the Pd black catalyst decreased with cell operation time, with a consequent loss in DFAFC performance. However, the lost activity could largely be recovered by applying a high anodic potential. The DFAFC that utilized the Pd anode catalyst not only generated a much higher power density than either the DFAFC or DMFC using the Pt–Ru catalyst, but also approached the performance of a hydrogen-PEM fuel cell. Deactivation of the Pd catalyst was a problem for the DFAFCs, particularly when operated with high formic acid concentrations, but again it was found that the initial cell performance could be recovered by applying a potential of 1.2V to the anode for several seconds.

The Pd catalyst may overcome the CO poisoning effect because the electro-oxidation of formic acid proceeds primarily through the direct pathway (reaction 1.12).⁷⁵⁻⁷⁶ The formic acid is directly oxidized to CO₂ and there is no CO intermediate formed.⁷⁷ In order to further improve the electrocatalytic performance of Pd catalysts, Pd-based binary metallic catalysts have been investigated. To date, the mechanism by which the electrocatalytic performance is increased in

Pd-based binary metallic catalysts is still not clear. Two hypotheses have been suggested. It was considered that the second atom may increase the adsorption capacity of the active oxygen and subsequently the oxidation rate of formic acid or it may act to prevent the formation of strongly adsorbed CO. The Pd-based binary metallic catalysts studied include Pd–Ni, Pd–Au, Pd–Pt, etc.⁷⁸⁻⁸⁰

1.5 Scope of this thesis

The main intent of this M.Sc. thesis is to synthesize Pd-based and Pt-based nanomaterials and to study their electrochemical properties for fuel cell applications. The first and most hopeful ongoing research goal is to decrease the cost of materials that are required for a given application by employing an alternate metal with lower cost. One target of this research involves the development of new synthesis methods which will lead to the creation of high catalytic surface areas. An increase in the surface area/volume ratio for catalysts will translate to decreased material costs.

It appears that for all hydrogen absorbing applications (purification and storage) there are two common issues which need to be addressed; namely hydrogen embrittlement and poisoning species. In addition, hydrogen solubility plays an important role in some applications. For hydrogen dissociation applications (e.g., hydrogen storage and catalysis), where surface interactions are of greater concern than bulk phase absorption, the adsorption strength of atomic hydrogen is the most crucial factor. All of these properties may be modified by alloying Pd with other metals. Another goal of this research is to investigate the alloying effect of Pd and Pt in order to develop efficient Pd-based and Pt-based nanostructured catalysts.

This thesis is comprised of six chapters. In the following chapter, experimental methods for the synthesis of Pd-based nanomaterials will be discussed, as well as the methods that are used to analyze their structures and physical properties. Chapter 3 will present the results of a study on the electrosorption of hydrogen into Pd-Ag nanostructures. Chapter 4 will discuss the hydrogen absorption properties of Pd deposited on TiO₂ nanotubes with high surface area. Chapter 5 will present the results of a study of Pt-Au catalysts and Pd-Ag catalysts for the oxidation of formic acid. The final chapter, Chapter 6, will provide a summary of the results and outlook of the future work.

Reference

- (1) Vasquez, L. O. *Fuel Cell Research Trends*; Nova Science Publishers: New York, 2007.
- (2) Epping Martin, K.; Kopasz John, P.; McMurphy Kevin, W. In *Fuel Cell Chemistry and Operation*; American Chemical Society: 2010; Vol. 1040, p 1.
- (3) Winter, M.; Brodd, R. J. *Chem. Rev.* **2004**, *104*, 4245.
- (4) Herring, A. M. *Fuel Cell Chemistry and Operation*; American Chemical Society, 2010; Vol. 1040.
- (5) Barbir, F. *PEM Fuel Cells Theory and Practice*; Elsevier Academic Press: Amsterdam; Boston, 2005.
- (6) Basu, S. *Recent Trends in Fuel Cell Science and Technology*; Springer; Anamaya: New York : New Delhi, 2007.
- (7) Gupta, R.; Pant, K. In *Hydrogen Fuel*; CRC Press: 2008, p 2.

- (8) Deshpande, K.; Meldon, J. H.; Schmidt, M. A.; Jensen, K. F. *J. Microelectromech. Syst.* **2010**, *19*, 402.
- (9) http://climatelab.org/fuel_cells.
- (10) Yu, X.; Pickup, P. G. *J. Power Sources* **2008**, *182*, 124.
- (11) Ha, S.; Dunbar, Z.; Masel, R. I. *J. Power Sources* **2006**, *158*, 129.
- (12) Park, I. S.; Lee, K. S.; Choi, J. H.; Park, H. Y.; Sung, Y. E. *J. Phys. Chem. C* **2007**, *111*, 19126.
- (13) Huang, Y. J.; Zhou, X. C.; Liao, J. H.; Liu, C. P.; Lu, T. H.; Xing, W. *Electrochem. Commun.* **2008**, *10*, 1155.
- (14) Uhm, S.; Lee, H. J.; Kwon, Y.; Lee, J. *Angew. Chem.-Int. Edit.* **2008**, *47*, 10163.
- (15) Yi, Q. F.; Chen, A. C.; Huang, W.; Zhang, J. J.; Liu, X. P.; Xu, G. R.; Zhou, Z. H. *Electrochem. Commun.* **2007**, *9*, 1513.
- (16) Wang, R. F.; Liao, S. J.; Ji, S. *J. Power Sources* **2008**, *180*, 205.
- (17) Wang, X. M.; Xia, Y. Y. *Electrochim. Acta* **2009**, *54*, 7525.
- (18) Wang, Y. J.; Wu, B.; Gao, Y.; Tang, Y. W.; Lu, T. H.; Xing, W.; Liu, C. P. *J. Power Sources* **2009**, *192*, 372.
- (19) Yu, X. W.; Pickup, P. G. *J. Power Sources* **2008**, *182*, 124.
- (20) Zhu, Y.; Kang, Y.; Zou, Z.; Zhou, Q.; Zheng, J.; Xia, B.; Yang, H. *Electrochem. Commun.* **2008**, *10*, 802.
- (21) Markovic, N. M.; Ross, P. N. *Surf. Sci. Rep.* **2002**, *45*, 121.
- (22) Park, I.-S.; Lee, K.-S.; Choi, J.-H.; Park, H.-Y.; Sung, Y.-E. *J. Phys. Chem. C* **2007**, *111*, 19126.
- (23) Schlappbach, L.; Zuttel, A. *Nature* **2001**, *414*, 353.

- (24) Gupta, R. B. In *Hydrogen fuel: production, transport and storage*; CRC; Taylor & Francis: Boca Raton, Fla.: London, 2009.
- (25) Banerjee, S.; Puri, I. K. *Nanotechnology* **2008**, *19*.
- (26) Orimo, S.-i.; Nakamori, Y.; Eliseo, J. R.; Züttel, A.; Jensen, C. M. *Chem. Rev.* **2007**, *107*, 4111.
- (27) Pillai, P.; Raja, K. S.; Misra, M. *J. Power Sources* **2006**, *161*, 524.
- (28) Sun, Z.; Liufu, S.; Chen, X.; Chen, L. *Chem Commun (Camb)* **2010**, *46*, 3101.
- (29) Yang, J.; Sudik, A.; Wolverton, C.; Siegel, D. J. *Chem. Soc. Rev.* **2010**, *39*, 656.
- (30) Gupta, R.; Pant, K. In *Hydrogen Fuel*; CRC Press: 2008, p 409.
- (31) Gupta, R.; Pant, K. In *Hydrogen Fuel*; CRC Press: 2008, p 381.
- (32) Kishore, S.; Nelson, J. A.; Adair, J. H.; Eklund, P. C. *J. Alloy. Compd.* **2005**, *389*, 234.
- (33) Peng, Q.; Chen, G.; Mizuseki, H.; Kawazoe, Y. *J. Chem. Phys.* **2009**, *131*.
- (34) Adams, B. D.; Wu, G. S.; Nigrio, S.; Chen, A. C. *J. Am. Chem. Soc.* **2009**, *131*, 6930.
- (35) Lin, J. Y. *Science* **2000**, *287*, 1929.
- (36) Liu, C.; Fan, Y. Y.; Liu, M.; Cong, H. T.; Cheng, H. M.; Dresselhaus, M. S. *Science* **1999**, *286*, 1127.
- (37) Schuth, F. *Nature* **2005**, *434*, 712.
- (38) Thornton, A. W.; Nairn, K. M.; Hill, J. M.; Hill, A. J.; Hill, M. R. *J. Am. Chem. Soc.* **2009**, *131*, 10662.
- (39) Shin, K.; Kim, Y.; Strobel, T. A.; Prasad, P. S. R.; Sugahara, T.; Lee, H.; Sloan, E. D.; Sum, A. K.; Koh, C. A. *J. Phys. Chem. A* **2009**, *113*, 6415.
- (40) Mavrandonakis, A.; Klontzas, E.; Tylianakis, E.; Froudakis, G. E. *J. Am. Chem. Soc.* **2009**, *131*, 13410.

- (41) Li, Y.; Yang, R. T. *J. Am. Chem. Soc.* **2006**, *128*, 8136.
- (42) Belof, J. L.; Stern, A. C.; Eddaoudi, M.; Space, B. *J. Am. Chem. Soc.* **2007**, *129*, 15202.
- (43) Zhang, X.; Zhang, Q.; Zhao, A.; Guan, J.; He, D.; Hu, H.; Liang, C. *Energ. Fuels* **2010**, *24*, 3796.
- (44) Santana, R. C.; Jongpatiwut, S.; Alvarez, W. E.; Resasco, D. E. *Ind. Eng. Chem. Res.* **2005**, *44*, 7928.
- (45) Rautanen, P. A.; Lylykangas, M. S.; Aittamaa, J. R.; Krause, A. O. I. *Ind. Eng. Chem. Res.*, **2002**, *41*, 5966.
- (46) Castano, P.; Pawelec, B.; Aguayo, A. T.; Gayubo, A. G.; Arandes, J. M. *Industrial Ind. Eng. Chem. Res.*, **2008**, *47*, 665.
- (47) Ockwig, N. W.; Nenoff, T. M. *Chem. Rev.* **2007**, *107*, 4078.
- (48) Damle, A. In *Hydrogen Fuel*; CRC Press: 2008, p 283.
- (49) Foletto, E. L.; Da Silveira, J. V. W.; Jahn, S. L. *Latin Am. Appl. Res.* **2008**, *38*, 79.
- (50) Othman, M. R.; Tan, S. C.; Bhatia, S.; Fernando, W. J. N. *Fuel Process. Technol.* **2011**, *92*, 428.
- (51) Das, N.; Kundu, D.; Chatterjee, M. *J. Coat. Technol. Res.* **2010**, *7*, 383.
- (52) Kumbharkar, S. C.; Liu, Y.; Li, K. *J. Membr. Sci.* **2011**, *375*, 231.
- (53) Gabrielli, C.; Grand, P. P.; Lasia, A.; Perrot, H. *J. Electrochem. Soc.* **2004**, *151*, A1925.
- (54) Lasia, A. *J. Electroanal. Chem.* **2006**, *593*, 159.
- (55) Gabrielli, C.; Grand, P. P.; Lasia, A.; Perrot, H. *J. Electrochem. Soc.* **2004**, *151*, A1937.
- (56) Grden, M.; Piascik, A.; Koczorowski, Z.; Czerwinski, A. *J. Electroanal. Chem.* **2002**, *532*, 35.
- (57) Kibria, A.; Sakamoto, Y. *Int. J. Hydrog. Energy* **2000**, *25*, 853.

- (58) Grden, M.; Czerwinski, A.; Golimowski, J.; Bulska, E.; Krasnodebska-Ostrega, B.; Marassi, R.; Zamponi, S. *J. Electroanal. Chem.* **1999**, *460*, 30.
- (59) Yamauchi, M.; Ikeda, R.; Kitagawa, H.; Takata, M. *J. Phys. Chem. C* **2008**, *112*, 3294.
- (60) Lukaszewski, M.; Czerwinski, A. *J. Solid State Electrochem.* **2008**, *12*, 1589.
- (61) Lukaszewski, M.; Kedra, T.; Czerwinski, A. *Electrochem. Commun.* **2009**, *11*, 978.
- (62) Li, Y.; Cheng, Y. T. *Int. J. Hydrog. Energy* **1996**, *21*, 281.
- (63) Uhm, S.; Lee, H. J.; Lee, J. *Phys. Chem. Chem. Phys.* **2009**, *11*, 9326.
- (64) Chen, Y.; Zhou, Y. M.; Tang, Y. W.; Lu, T. H. *J. Power Sources* **2010**, *195*, 4129.
- (65) Zhang, S.; Shao, Y. Y.; Yin, G. P.; Lin, Y. H. *J. Power Sources* **2010**, *195*, 1103.
- (66) Zhang, S.; Shao, Y.; Liao, H.-g.; Liu, J.; Aksay, I. A.; Yin, G.; Lin, Y. *Chem. Mat.* **2011**, *23*, 1079.
- (67) Bai, Y.-C.; Zhang, W.-D.; Chen, C.-H.; Zhang, J.-Q. *J. Alloy. Compd.* **2011**, *509*, 1029.
- (68) Wang, J. P.; Holt-Hindle, P.; MacDonald, D.; Thomas, D. F.; Chen, A. C. *Electrochim. Acta* **2008**, *53*, 6944.
- (69) Yi, Q. F.; Zhang, J. J.; Chen, A. C.; Liu, X. P.; Xu, G. R.; Zhou, Z. H. *J. Appl. Electrochem.* **2008**, *38*, 695.
- (70) Wang, J. P.; Thomas, D. F.; Chen, A. C. *Chem. Commun.* **2008**, 5010.
- (71) Chen, D. J.; Zhou, Z. Y.; Wang, Q.; Xiang, D. M.; Tian, N.; Sun, S. G. *Chem. Commun.* **2010**, *46*, 4252.
- (72) Choi, J.-H.; Jeong, K.-J.; Dong, Y.; Han, J.; Lim, T.-H.; Lee, J.-S.; Sung, Y.-E. *J. Power Sources* **2006**, *163*, 71.
- (73) Morales-Acosta, D.; Ledesma-Garcia, J.; Godinez, L. A.; Rodriguez, H. G.; Alvarez-Contreras, L.; Arriaga, L. G. *J. Power Sources* **2010**, *195*, 461.

- (74) Chen, C. H.; Liou, W. J.; Lin, H. M.; Wu, S. H.; Borodzinski, A.; Stobinski, L.; Kedzierzawski, P. *Fuel Cells* **2010**, *10*, 227.
- (75) Ha, S.; Larsen, R.; Masel, R. I. *J. Power Sources* **2005**, *144*, 28.
- (76) Yu, X.; Pickup, P. G. *Electrochem. Commun.* **2009**, *11*, 2012.
- (77) Wang, X.; Tang, Y.; Gao, Y.; Lu, T. H. *J. Power Sources* **2008**, *175*, 784.
- (78) Yi, Q. F.; Huang, W.; Liu, X. P.; Xu, G. R.; Zhou, Z. H.; Chen, A. C. *J. Electroanal. Chem.* **2008**, *619*, 197.
- (79) Du, C.; Chen, M.; Wang, W.; Yin, G. *ACS Appl. Mater. Interfaces* **2011**, *3*, 105.
- (80) Bulushev, D. A.; Beloshapkin, S.; Ross, J. R. H. *Catal. Today* **2010**, *154*, 7.

Chapter 2 Experimental methods

2.1 Introduction

In the previous chapter, several types of fuel cells were discussed, inclusive of the challenges that must be addressed prior to their commercial implementation. Also, the objectives of the research that will comprise this thesis were outlined. In this chapter, the main experimental methodology and techniques used in this M.Sc. project will be briefly introduced. For clarity, some of the details of the experimental procedures and equipment that, pertain to each specific study, will be presented in Chapters 3 – 5.

2.2 Chemicals and materials

The following chemicals were used as received from Sigma-Aldrich: sulfuric acid (99.999%); perchloric acid (70%); hydrochloric acid (37.5%); nitric acid ($\geq 69\%$); ammonium formate (99.995%); Formic acid ($>96\%$); dimethyl sulfoxide (DMSO)(99.99%); hydrofluoric acid (50%), AgNO_3 ($\geq 99.0\%$); $\text{Pd}(\text{NO}_3)_2 \cdot \text{H}_2\text{O}$.

The following chemical materials and materials were used as received from Alfa-Aesar: titanium wire (99.7%, 2mm diameter); titanium strip (99.2%, 1.25cm \times 0.5mm); Pt wire (99.9%, 0.5 mm diameter); Pd wire (99.9%, 0,5mm diameter); $\text{HAuCl}_4 \cdot \text{H}_2\text{O}$ (99.9%); $\text{H}_2\text{PtCl}_6 \cdot 6\text{H}_2\text{O}$ (99.9%); PdCl_2 (99.9%).

The following gases were used throughout this thesis research: argon (PPAXAIR, UHP, 99.999%) and carbon monoxide (PRAXAIR, Grade 2.5, 99.5%).

Pure water (18M Ω cm) obtained from aNANOpure® Diamond™ UV ultrapure water purification system was used for cleaning purposes and in the preparation of all solutions and electrolytes.

2.3 Fabrication of nanomaterials

2.3.1 Ti-supported nanoparticles

The nanostructures used as electrodes in the hydrogen electrosorption studies (Chapter 3) were directly grown onto Ti plates using a facile hydrothermal reduction method. Ti plates (99.2%, 1.25 cm \times 0.80 cm \times 0.5 mm) were washed by sonication in acetone followed by pure water (18.2 M Ω cm), then etched in an 18 wt % HCl solution at 85 °C for 30 minutes, and finally rinsed with pure water. To fabricate the Pd-Ag nanostructures, the pre-etched Ti plates were placed in Teflon vessels containing 10 ml of an aqueous mixture of inorganic metal precursors and the reducing agent. The containers were subsequently heated at 180 °C for 2 hours.¹

Inductively coupled plasma atomic emission spectroscopy (ICP-AES) was used to verify completion of the reduction of the metal catalysts and the final composition of the Ti supported nanoparticles.

2.3.2 TiO₂ nanotube supported nanoparticles

TiO₂NTs were fabricated in a two-electrode electrochemical cell.² The etched Ti plate, which was thoroughly rinsed with pure water, served as the working electrode. The counter electrode consisted of a Pt plate (2 cm²), which was cleaned prior to each experiment via flame-annealing. The anodization took place in a solution that contained dimethyl sulfoxide (DMSO) with 2% (wt) HF and 2% (wt) H₂O at 40V for 8 hours. Following the electrochemical treatment, the sample

was rinsed thoroughly with pure water. Finally, the sample was baked at 450 °C for 3 h to form the anatase structured TiO₂NTs.

All TiO₂NTs supported nanostructures were used for hydrogen sorption (Chapter 4) and for formic acid oxidation (Chapter 5) All of the TiO₂NTs supported samples were prepared using a photo assisted reduction method. The inorganic precursors and reducing agent was initially deaerated for 20 minutes with ultrapure argon gas prior to measurements in order to remove any dissolved oxygen, followed by ultraviolet light irradiation. This procedure was repeated certain necessary times. The electrode was finally removed from the light, rinsed with ultra pure water and dried in a vacuum oven at 40°C. The precursors were reduced to their metal states and then deposited onto the TiO₂NTs.

2.4 Surface analysis

The surface morphology and composition of the coatings were characterized using a JEOL 5900LV scanning electron microscope (SEM) and X-ray energy dispersive spectrometry (EDS). The concentrations of silver and palladium in the solution following the hydrothermal reduction process were also analyzed using an inductively coupled plasma (ICP). The X-ray diffraction (XRD) (Philips PW 1050-3710 or PAN analytical X'Pert Pro MPD) patterns were recorded on a PW 1050-3710 diffractometer using a Cu K α ($\lambda = 1.5405 \text{ \AA}$) radiation source. X-ray photoelectron spectra were collected using a Thermo Scientific K-Alpha XPS spectrometer. All of the samples were run at a take-off angle (relative to the surface) of 90°. A monochromatic Al K α X-ray source was used, with a spot area of 400 μm . Charge compensation was provided and the position of the energy scale was adjusted to place the main C 1s feature (C-C) at 284.6 eV. All data processing was performed using XPSpeak software.

2.5 Electrochemical experiments

VoltaLab PGZ402 potentiostat was used in this work. All experiments were deoxygenated via the continuous passage of ultra-pure Ar gas either into the electrolyte before electrochemical measurements or over the top of the electrolyte during electrochemical measurements. A three-electrode cell was used, which included a saturated calomel electrode (SCE) connected to the cell through a salt bridge as the reference electrode, with a Pt wire coil as the counter electrode. The Pt wire coil was cleaned prior to each experiment by flame annealing and quenching with pure distilled water. Data acquisition and analysis were performed using VoltMaster 4 software. All of the experiments were carried out at room temperature (22 ± 2 °C).

2.6 Summary

This chapter has presented the materials that were used throughout the course of the research that was conducted for the compilation of this thesis. The experimental methods and equipment used for synthesizing and characterizing Pd-based and Pt-based nanomaterials were discussed in detail. The following chapter will present a study of Pd-Ag nanostructures for the electrosorption of hydrogen.

References

- (1) Chen, S.; Adams, B. D.; Chen, A. *Electrochim. Acta* **2010**, *56*, 61.
- (2) Tian, M.; Malig, M.; Chen, S.; Chen, A. *Electrochem. Commun.* **2011**, *13*, 370.

Chapter 3 Synthesis and electrochemical study of nanoporous Pd-Ag alloys for hydrogen sorption

3.1 Introduction

Hydrogen, because of its large combustion heat (287 kJ/mole) and its environmentally compatible by-product, water, is being extensively researched as an alternative to fossil fuels.¹⁻⁴ Storing hydrogen in a gas form or handling hydrogen in a liquid state at a critical low temperature (32.97K) presents difficult challenges for its practical usage. Hydrogen storage alloys provide one of the best ways to store hydrogen compactly and safely as a consequence of the high stability of their hydride.⁵⁻¹¹ Driven by the need to develop hydrogen absorption materials, studies on the interaction between metals and hydrogen have become increasingly important. Electrochemical study provides a feasible approach to determine the thermodynamic and kinetic parameters of hydrogen sorption, which is important for the development of new materials for hydrogen storage. Most studies have been focused on finding the optimal properties of the metallic materials in terms of fast hydriding/dehydriding kinetics, large hydrogen-uptake capacity, high cycle stability, and reasonable production costs.¹²⁻¹⁴ Poor reversibility and slow kinetics are the main problems of many metal hydride systems such as MgH_2 and $NaAlH_4$.³

Palladium and its alloys are classical materials for storing hydrogen above room temperature and show fast adsorption/absorption rates.^{13,15-17} The palladium/hydrogen system has been intensively investigated both in gas phase and under electrochemical conditions, due to its potential applications in hydrogen storage, metal-hydride batteries and hydrogen purification.¹⁸⁻²¹ However, the use of Pd as the sole metal hydride for hydrogen storage is not practical because of

its high cost and the hydrogen embrittlement caused by the phase transition from α to β in pure palladium.²² Pd-based alloys, on the other hand, offer a class of attractive materials for studying metal hydrides because of the high solubility and permeability of hydrogen compared to pure Pd as well as the reduced cost if cheaper metals are added.²³⁻²⁹ Great attention has been paid to nanostructured materials because of their high surface areas and significantly different properties compared to conventional materials with coarse grains.³⁰⁻³³ For instance, recent study has revealed that the electrochemical response of hydrogen at Pd is critically dependent on the size and structure of the Pd surface.³⁴ The analytical response can be easily tailored in favour of either H_{ad} oxidation by nanoscale tuning the coverage of Pd on Au nanoparticles. Nanostructured materials show distinct advantages in their hydrogen uptake characteristics compared with their bulk counterparts. Rapid hydrogen diffusion has been reported to occur in nanostructured materials, greatly improving the kinetics for hydrogen absorption and desorption.³⁵⁻³⁸ It has been reported that nanoparticles exhibit dilated lattices that would result in larger interstitial volumes for hydrogen storage and better storage characteristics.^{6,17} The characteristic hydrogen diffusion is automatically reduced due to the dilation of the lattice, leading to faster kinetics for hydrogen absorption and desorption.^{39,40}

Although palladium and silver have been widely used in electrochemical studies as electrodes, little attention has been directed to the synthesis and study of nanostructured palladium and silver alloys.⁴¹⁻⁴⁴ The relative low cost and strong structural properties of silver make it an attractive material to combine with palladium for hydrogen purification and storage. In the present study, for the first time, nanoporous Pd-Ag alloys with different amount of Ag varied from 0 to 40 at.% were synthesized using a facile hydrothermal method. The behaviour and characteristics of hydrogen absorption of the nanoporous Pd-Ag alloys were studied and compared with the pure

nanoporous Pd. The effects of sweep rate, electrode potential, and composition of Pd-Ag on hydrogen sorption have been systemically evaluated. Pd-Ag alloy is the most commonly used material for hydrogen extraction in industry.¹² The nanoporous Pd-Ag alloys fabricated in this study can be treated as a model system for other hydrogen sorbing materials; thus the knowledge gained from the present study provides some insights in the design of efficient Pd-based catalysts for hydrogen purification and storage.

3.2 Experimental Section

A series of Pd-Ag nanostructures with different compositions of Ag ranging from 0 to 40 at.% were directly grown onto Ti substrates using a hydrothermal method described in Chapter 2.^{45,46} In all cases, the amounts of the reducing agent of ammonium formate and ethylene glycol added were kept constant at 10 mM and 2.5M, respectively. Varying amounts of the $\text{Pd}(\text{NO}_3)_2 \cdot x\text{H}_2\text{O}$ and AgNO_3 precursors were added to obtain the desired ratio of Pd to Ag. After cooling to room temperature, the Pd-Ag coated Ti plates were finally dried in a vacuum oven at 40 °C.

The surface morphology of the fabricated samples was characterized using a JEOL JSM 590LV SEM. Surface composition was investigated by and Oxford Links ISIS energy dispersive X-ray spectrometer as well as XPS for the Pd-Ag(20%) sample. The XRD patterns of the as-prepared samples were recorded using a Philips PW 1050-3710 Diffractometer with $\text{Cu K}\alpha$ radiation.

For the hydrogen electrosorption measurements, the cell setup was described in Chapter 2. The reference electrode was a SCE connected to the cell through a salt bridge. All potentials mentioned herein are with respect to the SCE reference electrode. The working electrodes used were the prepared Ti/PdAg plates (1cm^2) The coating loads of the electrodes, for calculating the H/PdAg ratios, were determined by weighing the Ti plates before and after being coated with the

Pd-Ag nanostructures with a mass balance accurate to 0.01 mg. The electrolyte for these studies was 0.1 M HClO₄, and the solution was deaerated with ultrapure argon gas prior to measurements to remove any dissolved oxygen, and argon gas was continuously bubbled into the solution during the experiments to increase mass transport. At the beginning of the absorption experiments, each of the Pd-Ag electrodes was cycled continuously through the potential region of hydrogen adsorption and absorption until an invariant voltammogram was obtained on further scanning.

3.3 Surface morphology, composition, and structure of the prepared Pd-Ag electrodes

The surface morphology of the synthesized Pd-Ag alloys was examined by SEM at a magnification of 15,000. Fig 3.1a presents a typical SEM image of the Pd-Ag15% sample. All the Pd and Pd-Ag samples fabricated in this study possess nanoporous structures, similar to the Pd-Ag15% sample (Fig 3.1a), consisting of irregular pores ranging from several to hundreds of nanometers in diameter. It is expected that the porous structure possesses a high surface area, which is desirable for hydrogen sorption and storage. The EDS spectra of the seven nanoporous samples (pure Pd, Pd-Ag10%, Pd-Ag15%, Pd-Ag20%, Pd-Ag25%, Pd-Ag30% and Pd-Ag40%) are presented in Fig 3.1b. The peaks marked by a star are derived from the Ti substrate. Two Pd peaks and two Ag peaks are observed for all the nanoporous Pd-Ag samples. As expected, the intensity of the Ag peaks progressively increases from Pd-Ag10% to Pd-Ag40%. Quantitative analysis of these EDS spectra shows that the compositions of all the Pd-Ag samples are consistent with the composition of the Pd and Ag precursors initially added to the hydrothermal vessels. This is further confirmed by ICP analysis. Table 3.1 displays the ICP results for the amount of precursors remaining in solution (i.e. not reduced) after the hydrothermal reduction. These experimental results have demonstrated that the reduction agents chosen in this study can

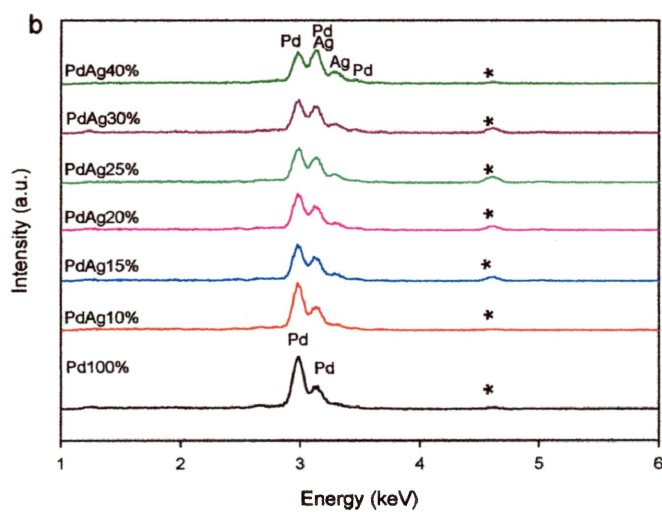
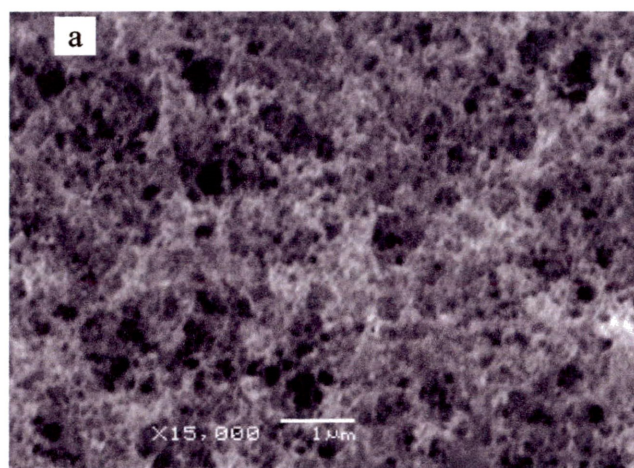


Fig 3.1. (a) Typical SEM image at 15,000 × magnification of the Pd-Ag surfaces with normalized atomic ratios of Pd/Ag of 85:15; (b) the EDS spectra of the nanoporous Pd and Pd-Ag alloys. The peaks labelled with (*) are derived from the Ti substrate.

Table 3.1. ICP results of the concentrations of Pd²⁺ and Ag⁺ remaining in solution after the hydrothermal reductions. Initial concentrations were calculated based on the amount of Pd(NO₃)₂ and AgNO₃ added to the hydrothermal vessels.

Sample	Pd(initial) /ppm	Pd(final) /ppm	Ag(initial) /ppm	Ag(final) /ppm	Molar ratio
					Pd : Ag
Pd	532.10	0.02	0.00	0.00	100:0
PdAg10%	478.89	0.06	53.93	0.00	90:10
PdAg15%	452.29	0.03	80.90	0.00	85:15
PdAg20%	425.68	0.18	107.87	0.03	80:20
PdAg25%	399.08	0.03	134.84	0.02	75:25
PdAg30%	372.47	0.13	161.80	0.00	70:30
PdAg40%	319.26	0.04	215.74	0.11	60:40

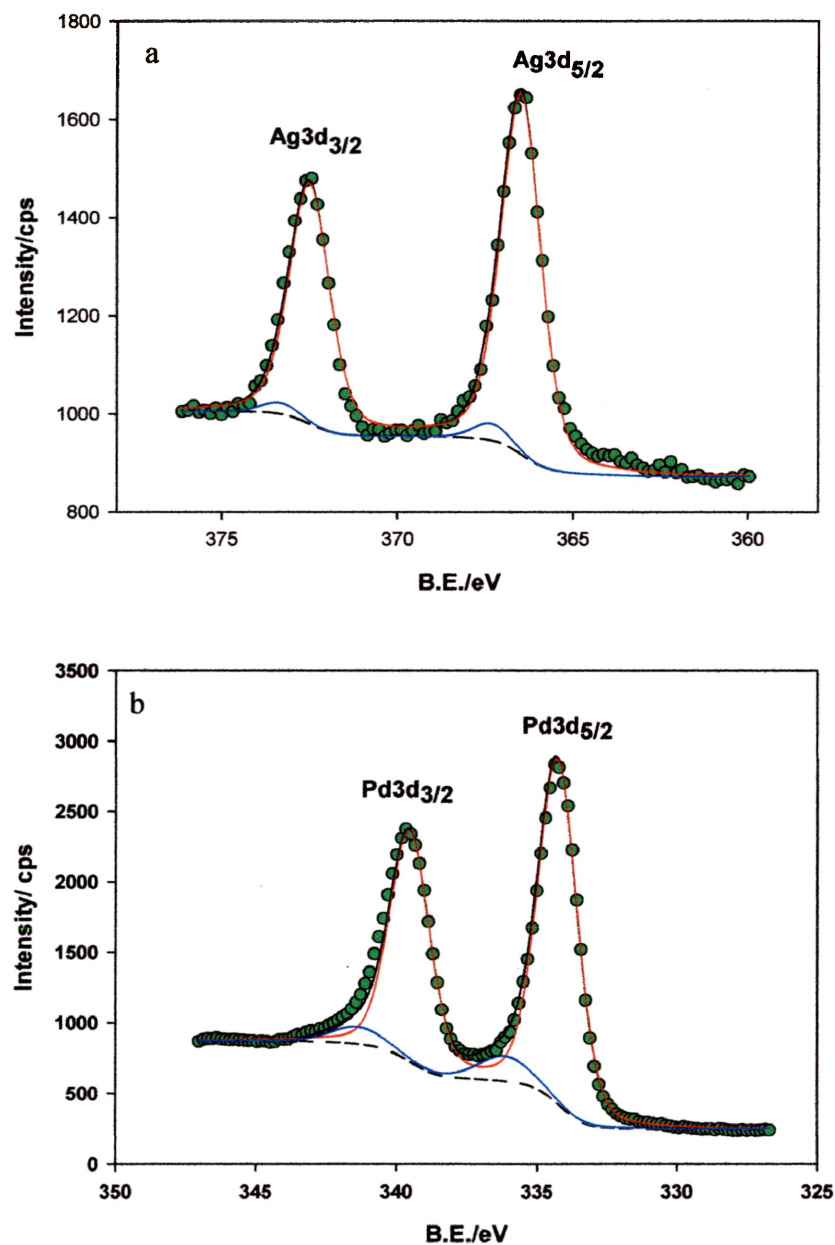


Fig.3 2. XPS spectra of the Pd3d (a) and Ag3d (b) regions for the Pd-Ag(20%) sample. The green dots, dashed lines, and red, blue, and black solid lines represent the raw data, baseline, individual components (zero and high oxidation states) and total fit, respectively.

effectively reduce the Pd²⁺ and Ag⁺ precursors under the hydrothermal condition and that the composition of the formed nanoporous Pd-Ag alloy can be easily controlled using this proposed new method.

X-ray photoelectron spectroscopy (XPS) was performed to analyze the surface composition and the electronic interaction of the Pd-Ag alloys. Fig 3.2 shows the high resolution XPS spectra for Pd(3d) and Ag(3d) of the sample Pd-Ag20%. The spectrum of Pd(3d) shows a doublet peaks located at a low binding energy (3d_{3/2}) at 334.4eV and at a high binding energy (3d_{5/2}) at 339.7eV (Fig 3.2a), indicating the presence of Pd in the metallic state Pd⁰ and higher oxidation states. The binding energies of the Ag(3d_{3/2}) and Ag(3d_{5/2}) peaks (Fig 3.2b) were measured at 366.5eV and 372.4eV, respectively. Using the area of the fitted curves for the Pd and Ag in both the metallic and the higher oxidation states, the ratio of metal/metal oxide was calculated. It was found that 92% of the Pd and 97% of the Ag were in their metallic states, further showing that the hydrothermal method employed in this study was efficient for the preparation of nanoporous Pd-Ag alloys. The actual atomic composition of Ag was also estimated based on the area under the peaks to be 17.74%, which is close to the nominal Pd:Ag ratio of 80:20.

X-ray diffraction was used to characterize the phase structure of the samples. Fig 3.3a presents the XRD patterns of the nanoporous Pd and Pd-Ag samples, consistent with a face centered-cubic (fcc) unit cell. The 2θ values of 40.02°, 46.56°, 68.04°, and 82.05° for the nanoporous Pd can be indexed to the diffractions of the (111), (200), (220) and (311) planes of Pd, respectively (JCPDS file no. 46-1043). The absence of Ag peaks in the XRD patterns of the nanoporous Pd-Ag samples suggests that there were no Pd and Ag crystalline metal phase separation and that Pd-Ag bimetallic alloyed structures were formed. In addition, all the peaks slightly shifted to a lower angle position due to the incorporation of increasing amounts of the larger Ag atoms into

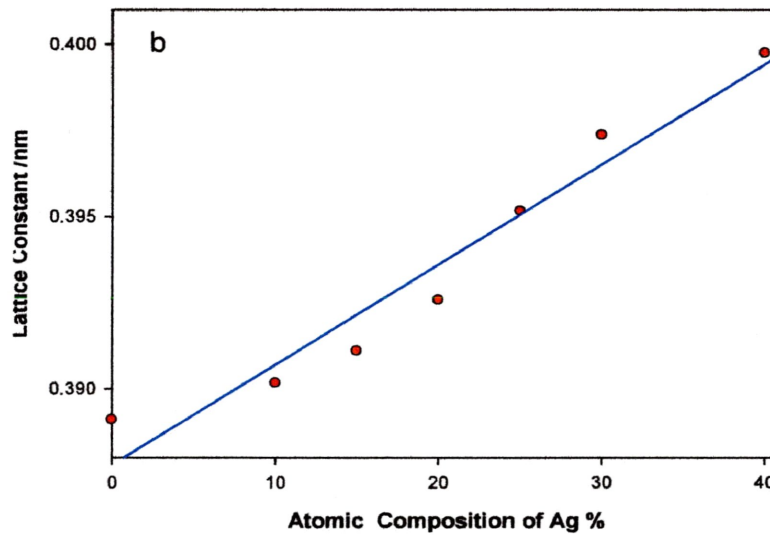
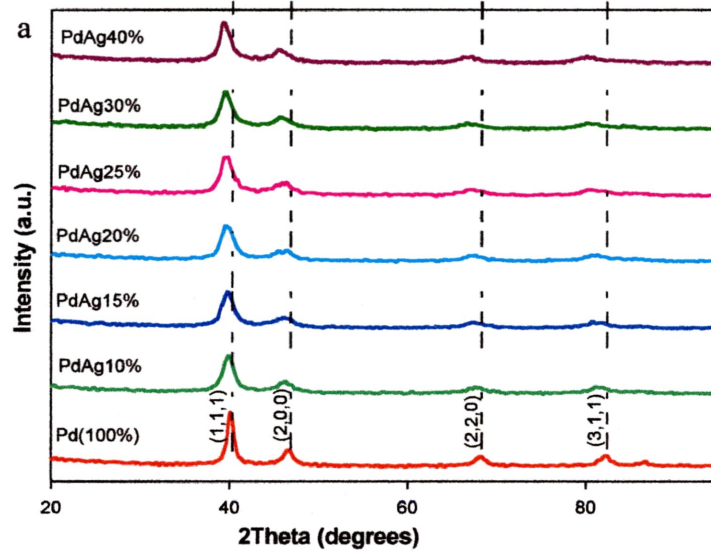


Fig. 3.3. (a) XRD patterns of the prepared Pd and PdAg films; (b) Vegard's plot showing the dependence of the fcc lattice constant calculated from the (220) peaks of each XRD pattern in (a) using Eq. (1) on the normalized atomic composition of Ag.

the Pd fcc lattice, indicating that the lattices in the nanoporous Pd-Ag were expanded. The fcc lattice parameter can be calculated from the diffraction peak positions. In the XRD patterns the (220) peak was used to calculate the lattice parameter a using the Bragg's equation⁴⁷:

$$a = \frac{\sqrt{2}\lambda_{K\alpha}}{\sin \theta_{max}} \quad (1)$$

where a is the lattice constant, λ is the wavelength of X-ray radiation (Cu $K\alpha = 0.15405$ nm), and θ is the location of the (220) peak in radians. A plot of the lattice constant vs. the normalized atomic composition of Ag of the nanoporous Pd-Ag alloys (Vegard's plot) is shown in Fig 3.3b. The lattice constant of the Pd-Ag alloys linearly increases with the increase of the Ag component. The lattice constant of the nanoporous Pd is 0.389 nm, which increases to 0.400 nm for the Pd-Ag40% sample, showing a significant dilation of the lattice constant with increasing amounts of Ag.

3.4 General cyclic voltammetric (CV) behaviour of the Pd-Ag nanostructures

For a general hydrogen electrosorption characterization of the nanoporous Pd and Pd-Ag alloys, two cycles of CVs in the range of -300 to 400 mV were recorded in 0.1 M perchloric acid at a scan rate of 20 mV/s; the second cycle was presented in Fig 3.4. For comparison, Fig 3.4 displays the CV curves of the nanoporous Pd and Pd-Ag alloys with 10, 20 and 30 at.% Ag. As the high current caused by hydrogen absorption dominates and covers the adsorption processes, it is difficult to decouple the adsorption process from the absorption process.¹⁸ A large broad peak due to the desorption of hydrogen appears between -300 and 0.0 mV when scanning the electrode potential from -300 mV to +400 mV, The integrated peak intensity for the hydrogen desorption/oxidation (i.e. the discharge) significantly increased when the Ag content was

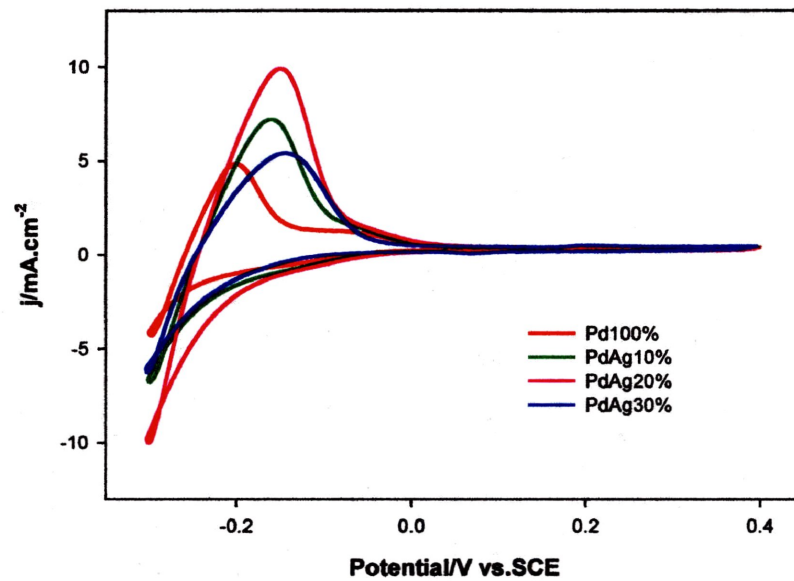


Fig. 3.4. Cyclic voltammograms of the PdAg electrodes recorded in 0.1 M HClO_4 at a scan rate of 20 mV/s.

increased from 0% to 20%. Further increasing the Ag amount to 30%, the hydrogen discharge decreased, showing that the amount of Ag incorporated into Pd has a strong impact on the capacity of hydrogen sorption of the Pd-Ag nanomaterials.

3.5 Sweep rate dependence of hydrogen electrosorption in the Pd-Ag nanostructures

To illustrate the effect of the sweep rate on the hydrogen electrosorption, Fig 3.5a presents the CV curves of the nanoporous Pd-Ag20% alloy recorded at the sweep rates varied from 5 to 50 mV/s. A well defined hydrogen sorption peak centered at -285 mV is observed at the low sweep rate (5 mV/s). The total charge, Q_H , due to hydrogen adsorption and absorption into the Pd-Ag nanostructures versus the potential scan rate is shown in Fig. 3.5b. The amount of hydrogen sorbed into the nanoporous Pd-Ag alloy, calculated from the charge of the hydrogen desorption/oxidation peaks, was found to be dependent on the sweep rate used in the cyclic voltammetric experiments. Increasing the potential scan rate results in a decrease in the hydrogen discharge, showing that a low sweep rate is preferential for determining the hydrogen adsorbing/absorbing capacity of the Pd-Ag nanostructures.

3.6 Influence of the electrode potential and the composition of the Pd-Ag alloys on the capacity of hydrogen electrosorption

The electrosorption of hydrogen into the nanoporous Pd-Ag alloys was further examined at different electrode potentials varied from -275 to -175 mV vs. SCE. The potential was first held at a constant potential for a period of time; linear voltammetry was then run starting from the held potential to +200 mV. The effect of the time held at different potentials on the hydrogen discharge was investigated, revealing that a period of 5 minutes is long enough to obtain complete saturation of hydrogen into the nanoporous Pd and Pd-Ag alloys. For comparison, Fig

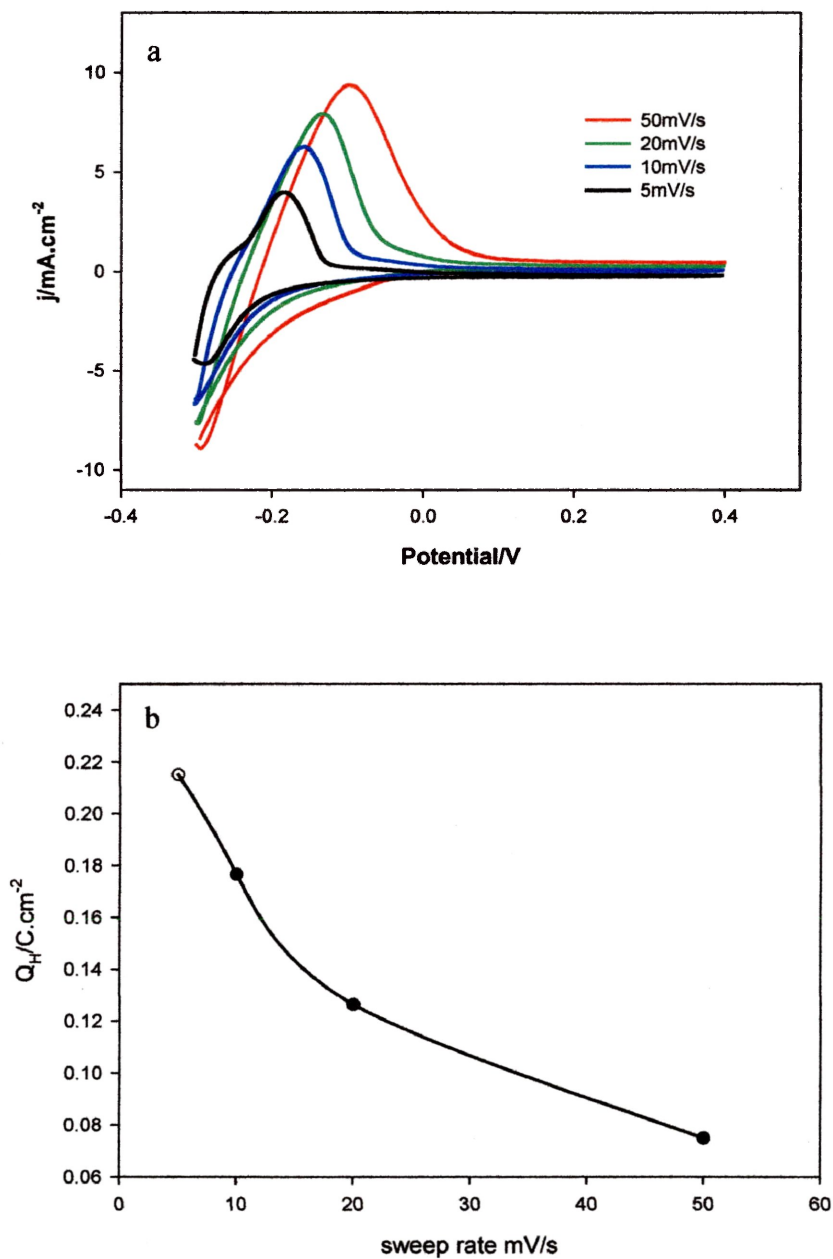


Fig. 3.5. a Cyclic voltammograms of the Pd-Ag(20%) electrode recorded in 0.1 M HClO₄ at various scan rates. b Charge due to hydrogen desorption versus sweep rate calculated by integrating the area under the anodic peaks in a.

3.6a and 3.6b present the linear voltammograms of the nanoporous Pd and Pd-Ag20%, respectively, recorded at the scan rate of 20 mV/s after being held at each of the pre-selected potentials for 5 min. The intensity of the hydrogen desorption/oxidation peak strongly depends on the held electrode potential; the lower the potential, the larger the peak. Similar behaviour is also observed for other nanoporous Pd-Ag alloys, reflecting the fact that, under the electrochemical conditions, the amount of hydrogen sorbed into the Pd and Pd-Ag alloys is potential dependent. A lower electrode potential corresponds to a higher hydrogen pressure in gas-phase experiments.^{8,26} For pure Pd, the absorption of hydrogen produces two different phases (α phase and β phase).⁴⁸ At low concentrations of hydrogen, the α -phase appears, which possesses a lattice constant very similar to pure Pd. At high concentrations of hydrogen (metal hydride), the β phase forms, resulting in an increase in the lattice constant. The large expansion of the lattice constant can cause cracking of the membrane (hydrogen embrittlement). As seen in Fig 3.6a, for the nanoporous Pd, a significant increase of the peak intensity is observed when the held potential was changed from -225 to -250mV, which corresponds to the transition from the α phase to β phase hydrogen sorption. However, no sharp transition was observed for the nanoporous Pd-Ag20% (Fig 3.6b). Note that the peak intensity of the nanoporous Pd-Ag20% is much higher than that of the pure nanoporous Pd when the potential was held at -225 mV.

To quantitatively examine the effect of the held potential on the capacity of the hydrogen sorption into the nanoporous Pd and Pd-Ag alloys, the total hydrogen discharge was calculated by integrating the hydrogen desorption/oxidation peak shown in Fig 3.6. Fig 3.7a depicts the dependence of the electrochemically measured hydrogen absorption capacity, expressed as the integrated hydrogen discharge, on the different absorption potentials for the nanoporous Pd-Ag alloys with different Ag composition varied from 0 to 40%. The plots can be divided into two

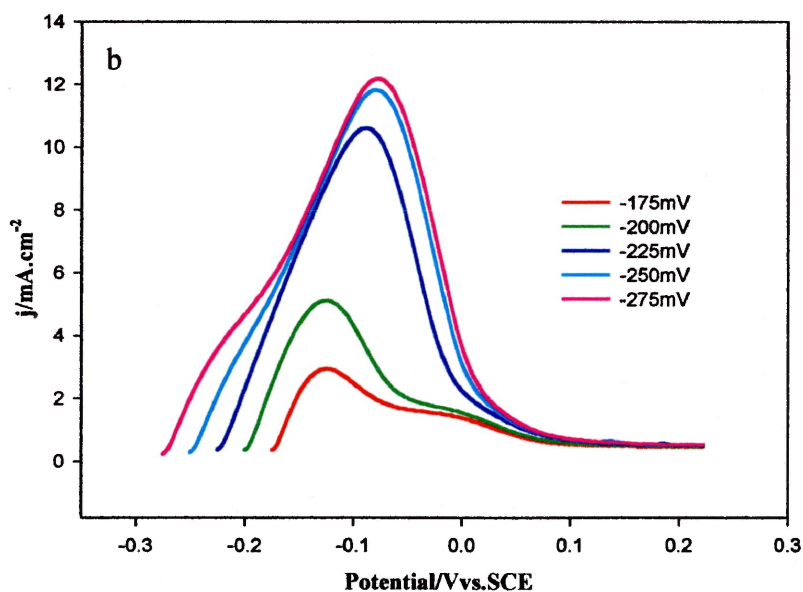
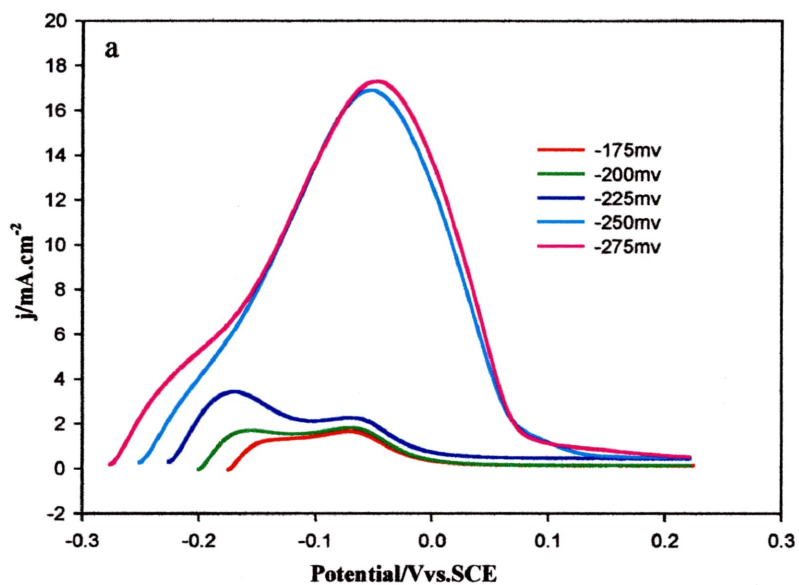


Fig. 3.6. Anodic sweeps of the desorption of hydrogen from (a) Pd and (b) Pd-Ag(20%) after holding the potential at various cathodic limits for 5 minutes in 0.1 M HClO₄. The scan rate was 20 mV/s.

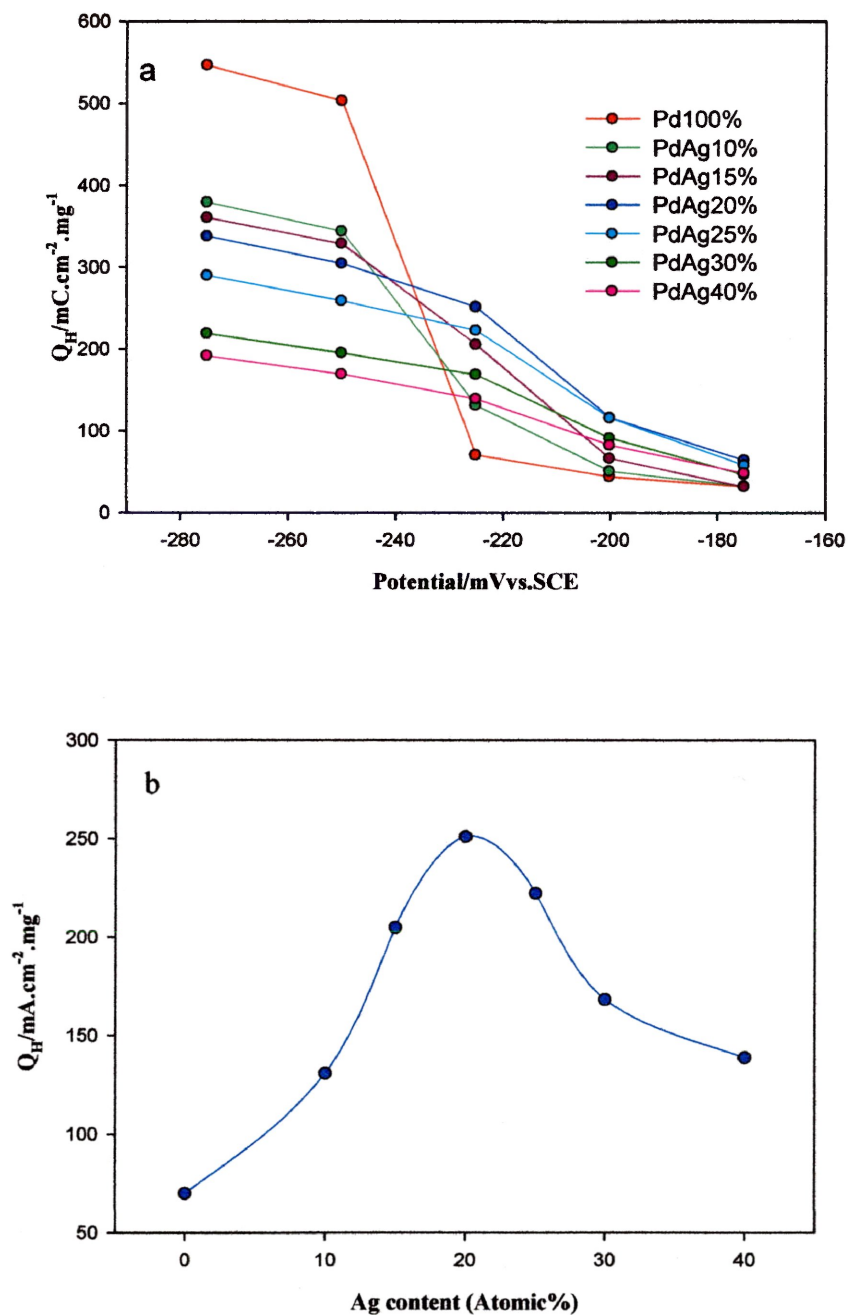


Fig 3.7. (a) The overall hydrogen desorption charge, Q_H , normalized by the mass of the Pd and Pd-Ag alloys versus different potentials. (b) The overall hydrogen desorption charge, Q_H , after hydrogen electroadsorption at -225mV versus the normalized atomic composition of Ag.

sections. The potential range above -225 mV corresponds to α phase hydrogen sorption; while the potential below -225 mV leads to the β phase hydrogen sorption. Increasing the composition of Ag from 0 to 40% decreases the β phase hydrogen sorption capacity and diminishes the α to β phase transition. In contrast, increasing the composition of Ag increases the α phase hydrogen sorption capacity. After reaching the maximum capacity, further increase of the amount of Ag results in a decrease of the hydrogen sorption capacity. For comparison, Fig 3.7b presents the hydrogen sorption capacity at -225 mV versus the composition of Ag of the nanoporous Pd-Ag alloys. When the Ag content is increased from 0 to 20%, the hydrogen sorption significantly increases. Further increasing the Ag content from 20% to 40%, the hydrogen sorption capacity decreases. The nanoporous Pd-Ag20% possesses the highest capacity for the α phase hydrogen sorption, which is over 4 times larger than the nanoporous Pd. This can be attributed to the dilation of lattice constant resulting from the incorporation of larger Ag atoms into the Pd fcc lattice as seen in Fig.3.3.

3.7 Dependence of hydrogen sorption time on the electrode potential and composition of Pd-Ag

The kinetics of hydrogen sorption into the nanoporous Pd-Ag alloys was further investigated using chronoamperometry. First, the potential on the Pd-Ag electrodes was held at +200 mV for 30s, where neither hydrogen absorption nor adsorption occurs. The electrode potential was then stepped down to the hydrogen sorption region between -175 and -275mV; and the corresponding chronoamperometric ($i - t$) curves were recorded (not shown here) in order to determine the time needed for a steady-state saturation of the nanoporous Pd-Ag electrodes with hydrogen. As shown in Fig 3.8, the saturation time strongly depends on the composition of the nanoporous Pd-

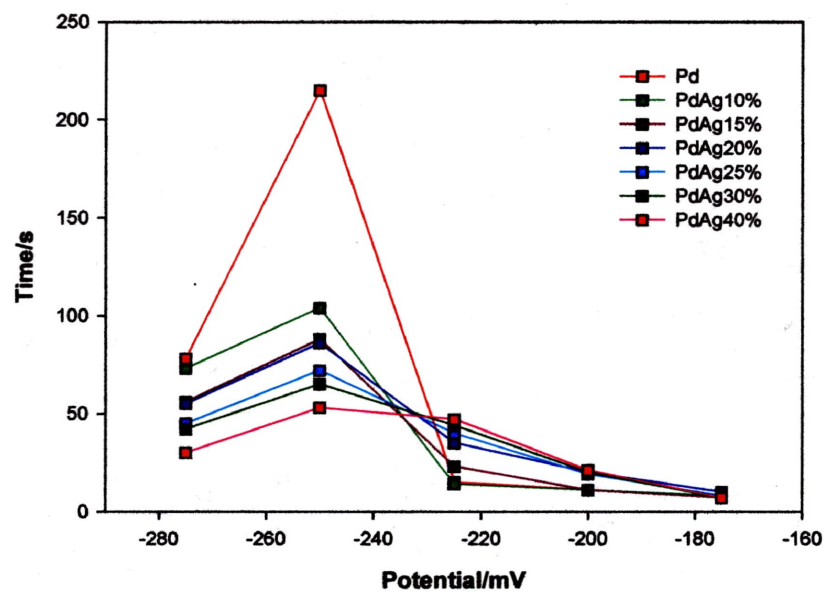


Fig. 3.8. The time required for obtaining steady state saturation of the electrodes with absorbed hydrogen with respect to potential.

Ag alloys and the applied potential. For all the nanoporous Pd and Pd-Ag electrodes, the maximum time (t_m) required to achieve the hydrogen saturation occurs at the same potential (-250 mV), where the β phase hydrogen sorption takes place. The t_m for the nanoporous Pd is much higher than that for the nanoporous Pd-Ag electrodes. The addition of Ag dramatically lowers the maximum time. The increase of the amount of Ag results in a decrease of t_m . For the nanoporous Pd, when the potential was changed from -225 to -250 mV, the time required for hydrogen saturation was increased from 15 to 215s. This is consistent with the study of the hydrogen sorption capacity shown in Fig 3.7a, where a sharp α to β phase transition was observed at -250 mV. The above results indicate that the α to β phase transition is the rate determining step and that the addition of Ag not only increases the α phase hydrogen sorption capacity, but also improves the kinetics of hydrogen sorption.

3.8 Conclusions

In this study, nanoporous Pd-Ag alloys with the Ag content varied from 0 to 40% were successfully synthesized using a facile hydrothermal method. The method is very effective and can easily control the composition of the formed Pd-Ag nanostructures. The XRD analysis shows that the lattice constant of the nanoporous Pd-Ag alloys increases with the increase of the amount of Ag. Electrochemical methods have been employed to systemically study the fabricated nanoporous Pd-Ag electrodes, showing that the hydrogen sorption into the nanoporous Pd-Ag alloys strongly depends on the composition of Pd-Ag and the applied sorption potential. Hydrogen sorption into the nanoporous Pd occurs in two distinct phases (α phase and β phase). The addition of Ag greatly increases the α phase hydrogen sorption capacity and diminishes the α and β phase transition due to the dilation of the lattice constant. The nanoporous Pd-Ag alloy with 20% silver content possesses the highest capacity for the α phase hydrogen sorption at -225

mV, which is over 4 times higher than the pure nanoporous Pd. The study has also shown that the phase transition is the rate limiting step in the hydrogen absorption process and, therefore, with the addition of Ag, the kinetics is much faster. The combination of the enhanced α phase hydrogen sorption capacity and diminishing of the α and β -phase transition makes the nanoporous Pd-Ag alloys attractive for hydrogen selective membranes and hydrogen dissociation catalysts.

References

- (1) Turner, J. A. *Science* **2004**, *305*, 972.
- (2) Reguera, E. *Int. J. Hydrog. Energy* **2009**, *34*, 9163.
- (3) Hamaed, A.; Hoang, T. K. A.; Trudeau, M.; Antonelli, D. M. *J. Organomet. Chem.* **2009**, *694*, 2793.
- (4) Peng, Q.; Chen, G.; Mizuseki, H.; Kawazoe, Y. *J. Chem. Phys.* **2009**, *131*.
- (5) Lukaszewski, M.; Kusmierczyk, K.; Kotowski, J.; Siwek, H.; Czerwinski, A. *J. Solid State Electrochem.* **2003**, *7*, 69.
- (6) Kobayashi, H.; Yarnauchi, M.; Kitagawa, H.; Kubota, Y.; Kato, K.; Takata, M. *J. Am. Chem. Soc.* **2008**, *130*, 1828.
- (7) Amorim, C.; Keane, M. A. *J. Colloid Interface Sci.* **2008**, *322*, 196.
- (8) Comisso, N.; De Ninno, A.; Del Giudice, E.; Mengoli, G.; Soldan, P. *Electrochim. Acta* **2004**, *49*, 1379.
- (9) Li, Y.; Cheng, Y. T. *Int. J. Hydrog. Energy* **1996**, *21*, 281.
- (10) Chen, Y.; Sequeira, C.; Allen, T.; Chen, C. P. *J. Alloy. Compd.* **2005**, *404*, 661.

- (11) Friedrichs, O.; Kolodziejczyk, L.; Sanchez-Lopez, J. C.; Fernandez, A.; Lyubenova, L.; Zander, D.; Koster, U.; Aguey-Zinsou, K. F.; Klassen, T.; Bormann, R. *J. Alloy. Compd.* **2008**, *463*, 539.
- (12) Sun, Y. G.; Tao, Z. L.; Chen, J.; Herricks, T.; Xia, Y. N. *J. Am. Chem. Soc.* **2004**, *126*, 5940.
- (13) Yamauchi, M.; Ikeda, R.; Kitagawa, H.; Takata, M. *J. Phys. Chem. C* **2008**, *112*, 3294.
- (14) Czerwinski, A.; Kiersztyn, I.; Grden, M.; Czapla, J. *J. Electroanal. Chem.* **1999**, *471*, 190.
- (15) Kadirgan, F.; Kannan, A. M.; Atilan, T.; Beyhan, S.; Ozenler, S. S.; Suzer, S.; Yorur, A. *Int. J. Hydrog. Energy* **2009**, *34*, 9450.
- (16) Grden, M.; Piascik, A.; Koczorowski, Z.; Czerwinski, A. *J. Electroanal. Chem.* **2002**, *532*, 35.
- (17) Avila-Garcia, I.; Plata-Torres, M.; Dominguez-Crespo, M. A.; Ramirez-Rodriguez, C.; Arce-Estrada, E. M. *J. Alloy. Compd.* **2007**, *434*, 764.
- (18) Gabrielli, C.; Grand, P. P.; Lasia, A.; Perrot, H. *J. Electrochem. Soc.* **2004**, *151*, A1937.
- (19) Gabrielli, C.; Grand, P. P.; Lasia, A.; Perrot, H. *J. Electrochem. Soc.* **2004**, *151*, A1925.
- (20) Martin, M. H.; Lasia, A. *Electrochim. Acta* **2008**, *53*, 6317.
- (21) Lasia, A. *J. Electroanal. Chem.* **2006**, *593*, 159.
- (22) Li, H.; Xu, H. Y.; Li, W. Z. *J. Membr. Sci.* **2008**, *324*, 44.
- (23) Zurowski, A.; Lukaszewski, M.; Czerwinski, A. *Electrochim. Acta* **2008**, *53*, 7812.
- (24) Słojewski, M.; Kowalska, J.; Jurczakowski, R. *J. Phys. Chem. C* **2009**, *113*, 3707.
- (25) Grden, M.; Czerwinski, A.; Golimowski, J.; Bulska, E.; Krasnodebska-Ostrega, B.; Marassi, R.; Zamponi, S. *J. Electroanal. Chem.* **1999**, *460*, 30.
- (26) Zurowski, A.; Lukaszewski, M.; Czerwinski, A. *Electrochim. Acta* **2006**, *51*, 3112.

- (27) Foletto, E. L.; Da Silveira, J. V. W.; Jahn, S. L. *Latin Am. Appl. Res.* **2008**, *38*, 79.
- (28) Adams, B. D.; Wu, G. S.; Nigrio, S.; Chen, A. C. *J. Am. Chem. Soc.* **2009**, *131*, 6930.
- (29) Adams, B.; Tian, M.; Chen, A. *Electrochim. Acta* **2009**, *54*, 1491.
- (30) Lukaszewski, M.; Klimek, K.; Czerwinski, A. *J. Electroanal. Chem.* **2009**, *637*, 13.
- (31) Kuji, T.; Matsumura, Y.; Uchida, H.; Aizawa, T. *J. Alloy. Compd.* **2002**, *330*, 718.
- (32) Chen, X. C.; Hou, Y. Q.; Wang, H.; Cao, Y.; He, J. H. *J. Phys. Chem. C* **2008**, *112*, 8172.
- (33) Polanski, M.; Bystrzycki, J. *J. Alloy. Compd.* **2009**, *486*, 697.
- (34) Liang, H. P.; Lawrence, N. S.; Jones, T. G. J.; Banks, C. E.; Ducati, C. *J. Am. Chem. Soc.* **2007**, *129*, 6068.
- (35) Tan, X. H.; Harrower, C. T.; Amirkhiz, B. S.; Mitlin, D. *Int. J. Hydrog. Energy* **2009**, *34*, 7741.
- (36) Barlag, H.; Opara, L.; Zuchner, H. *J. Alloy. Compd.* **2002**, *330*, 434.
- (37) Heinze, S.; Vuillemin, B.; Colson, J. C.; Giroux, P.; Leterq, D. *Solid State Ion.* **1999**, *122*, 51.
- (38) Nielsen, T. K.; Manickam, K.; Hirscher, M.; Besenbacher, F.; Jensen, T. R. *ACS Nano* **2009**, *3*, 3521.
- (39) Kishore, S.; Nelson, J. A.; Adair, J. H.; Eklund, P. C. *J. Alloy. Compd.* **2005**, *389*, 234.
- (40) Yamauchi, M.; Kobayashi, H.; Kitagawa, H. *ChemPhysChem* **2009**, *10*, 2566.
- (41) Medicherla, V. R. R.; Drube, W. *Appl. Surf. Sci.* **2009**, *256*, 376.
- (42) Lin, W. H.; Chang, H. F. *Surf. Coat. Technol.* **2005**, *194*, 157.
- (43) Kibria, A.; Sakamoto, Y. *Int. J. Hydrog. Energy* **2000**, *25*, 853.
- (44) McLeod, L. S.; Degertekin, F. L.; Fedorov, A. G. *J. Membr. Sci.* **2009**, *341*, 225.
- (45) Wang, J. P.; Thomas, D. F.; Chen, A. C. *Chem. Commun.* **2008**, 5010.

- (46) Wang, J. P.; Holt-Hindle, P.; MacDonald, D.; Thomas, D. F.; Chen, A. C. *Electrochim. Acta* **2008**, *53*, 6944.
- (47) Huang, Y. J.; Zhou, X. C.; Liao, J. H.; Liu, C. P.; Lu, T. H.; Xing, W. *Electrochem. Commun.* **2008**, *10*, 1155.
- (48) Narehood, D. G.; Kishore, S.; Goto, H.; Adair, J. H.; Nelson, J. A.; Gutierrez, H. R.; Eklund, P. C. *Int. J. Hydrog. Energy* **2009**, *34*, 952.

Chapter 4 Hydrogen Electrosorption into Palladium Nanoparticles Deposited on TiO₂ Nanotubes

4.1 Introduction

Palladium exhibits exceptional practical features for use in a hydrogen economy: hydrogen generation as a catalyst, hydrogen storage, hydrogen purification, energy generation from hydrogen to electricity, and hydrogen sensors.¹⁻⁴ In particular, palladium provides one of the best ways to store hydrogen safely and compactly as a consequence of the high capacity and great stability of its hydride.^{1,5-8} However, the primary bottleneck with bulk palladium for hydrogen storage involves its sluggish hydrogenation and dehydrogenation processes due to diffusion limitations.^{5,9-10} To address this issue, a number of nanoscale palladium materials supported on different substrates (gold, titanium, glassy carbon, carbon nanotubes, etc.) for hydrogen storage have been synthesized and studied.¹¹⁻¹⁴ During the past a few years, TiO₂ nanotubes (TiO₂ NTs) have attracted great research interest owing to their peculiar architecture, remarkable properties, and potential for wide-ranging applications.¹⁵⁻¹⁸ TiO₂ NTs employed as substrates for hydrogen storage exhibit many advantages.^{11,19-23} First, the relatively low cost of TiO₂ NTs that are produced by the anodization of titanium method renders these materials attractive for technological applications.^{16,24-25} Second, the semiconducting properties of TiO₂ NTs result in strong electronic interactions between the support and deposits, thereby improving the stability of the electrodes.²² Thirdly, in comparison with bulk Ti substrates, TiO₂ NT substrates make available extraordinarily large surface areas, which may serve to distribute the palladium more uniformly.¹⁵ Finally, the TiO₂ NTs themselves are effective materials for hydrogen storage.^{15,26-27}

However, to the best of our knowledge, Pd nanoparticles deposited onto TiO₂ nanotubes (TiO₂ NT/Pd) for hydrogen storage has not been investigated thus far.

In this work, both a hydrothermal method and a photo-assisted reduction method are utilized in the synthesis of Pd nanoparticles, which are then deposited on titanium and TiO₂ nanotube substrates, respectively. Hydrothermal reduction serves as an effective method for the formation of alloys in that the compositions of the alloys can be controlled in a facile manner, and through which a wide range of nanostructured materials may be easily synthesized.^{3,28-30} Photo-assisted reduction is a promising method for the deposition of Pd nanoparticles with a narrow particle size distribution onto TiO₂ NTs. The electrochemical behaviors of the Pd nanoparticles deposited on Ti and TiO₂ NTs were investigated, which showed that TiO₂ NT/Pd electrodes exhibit a high hydrogen capacity, prominent activity, fast kinetics and excellent stability for hydrogen sorption/desorption.

4.2 Experimental Section

To fabricate Ti supported Pd nanostructures, hydrothermal method was used described in Chapter 2. Ammonium formate was used as the reducing agent and PdCl₂ served as the metal precursor. The concentrations of the reducing agent and the PdCl₂ precursor were 500mM and 2.5mM, respectively.

The TiO₂NTs supported Pd nanostructures were prepared using photo assisted reduction method as described in Chapter 2. A solution comprised of 100uL of 50mM Pd(NO₃)₂ and 5mL of 50% methanol was first deaerated for 20 minutes with ultrapure argon gas prior to measurements in order to remove any dissolved oxygen, and then irradiated by ultraviolet light for 20 minutes. This procedure was repeated four times. The Pd was spontaneously deposited onto the surfaces

of the TiO₂ nanotubes. The coating loads of the electrodes, which are used for calculating H/Pd ratios, were determined by weighing the Ti plate or TiO₂ nanotube plate before and after being coated with the Pd nanostructures with a mass balance, accurate to 0.01 mg.

The surface morphology of the fabricated samples was characterized using a JEOL JSM 590LV SEM. Surface composition was investigated by and Oxford Links ISIS energy dispersive X-ray spectrometer as well as XPS for the Pd-Ag(20%) sample. The XRD patterns of the as-prepared samples were recorded using a Philips PW 1050-3710 Diffractometer with Cu K α radiation.

The electrochemical performance of the electrodes for hydrogen adsorption/absorption was characterized using cyclic voltammetry (CV). The reference electrode was a saturated calomel electrode (SCE) connected to the cell by means of a salt bridge. The working electrodes used were the prepared Ti/Pd and TiO₂ NT/Pd electrodes. The electrolyte for these CV studies was 0.1 M HClO₄, and the solution was deaerated with ultrapure argon gas prior to measurements. Argon was continually passed over the solution throughout the investigation.

4.3 Characterization of synthesized Ti/Pd and TiO₂ NT/Pd materials

Fig. 4.1 shows SEM images of the TiO₂ substrate (a), TiO₂ NT/Pd (b), and Ti/Pd (c) of the samples. It is observed that well-ordered and uniform TiO₂ NTs were formed on the pure titanium plate via the electrochemical anodic oxidation technique. The tops of the tubes were open and the diameters of these nanotubes ranged from 60 to 90 nm, with wall thicknesses of ~10 nm. Fig. 4.1 (b) shows the image of Pd deposited onto the TiO₂ NTs by photo-assisted reduction. Most of the palladium nanoparticles were attached at the tops and on the walls of the TiO₂ NTs, which served to increase the active surface area of the electrode considerably. This demonstrated that the photo-assisted reduction method is an effective strategy for reducing the

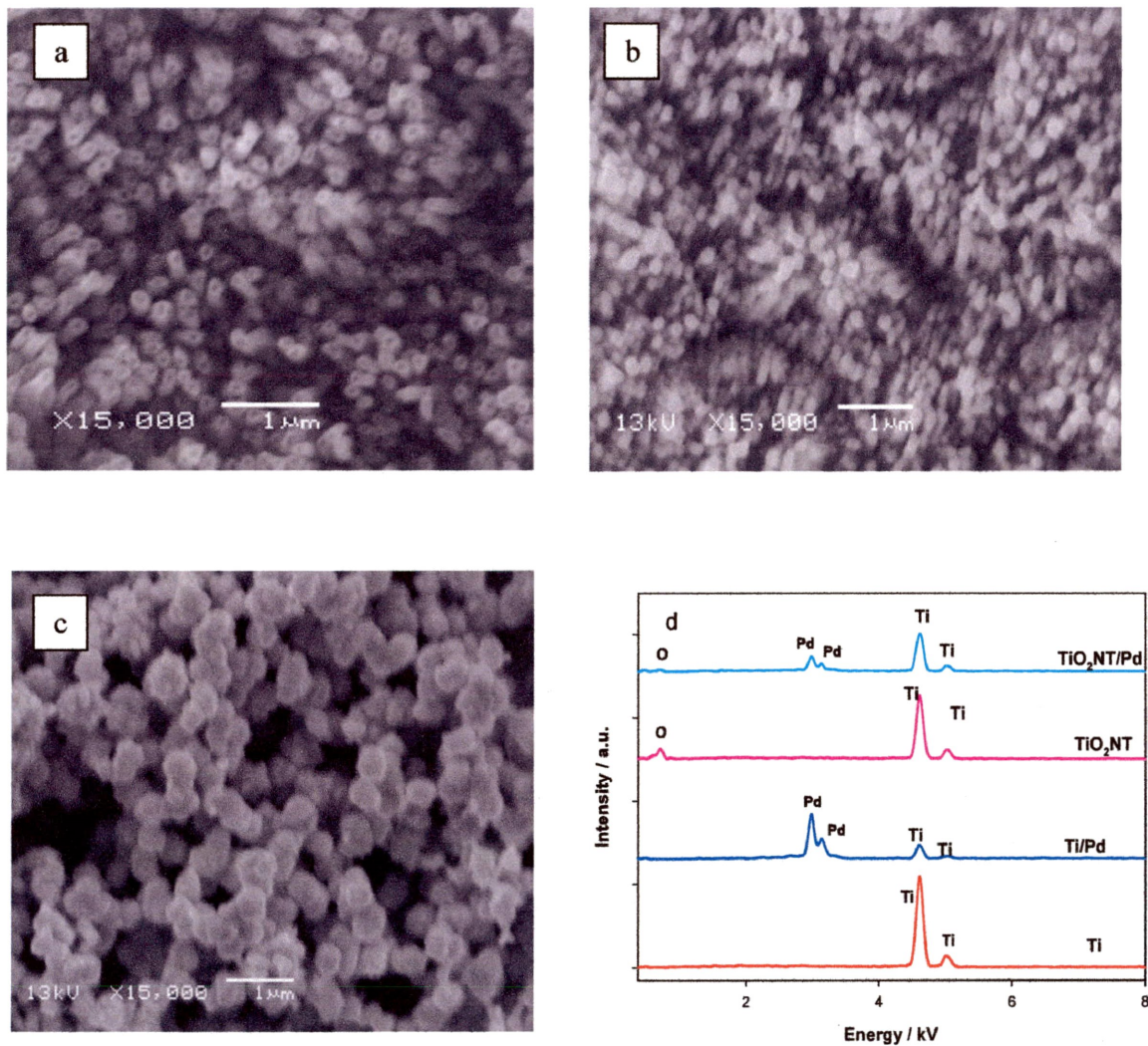


Fig.4.1. SEM images (15,000× magnification) of the samples: (a) the substrate of TiO₂ NTs prior to photo-assisted deposition; (b) Pd deposited onto TiO₂ NTs after photo-assisted deposition; (c) Pd deposited on a Ti substrate by the hydrothermal method. And (d) EDS spectra of the Ti/Pd and TiO₂ NT/Pd before and after Pd deposition.

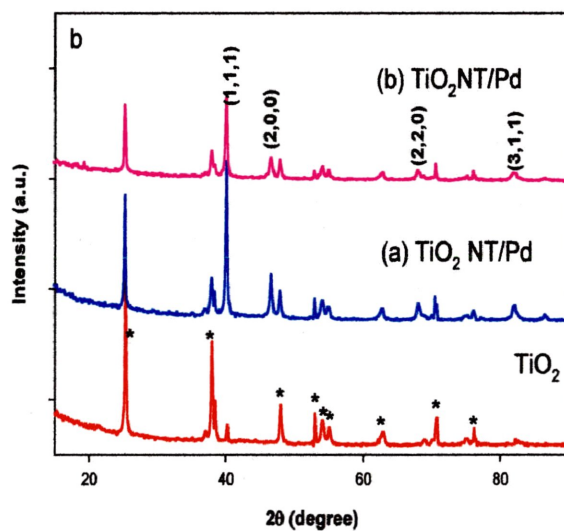
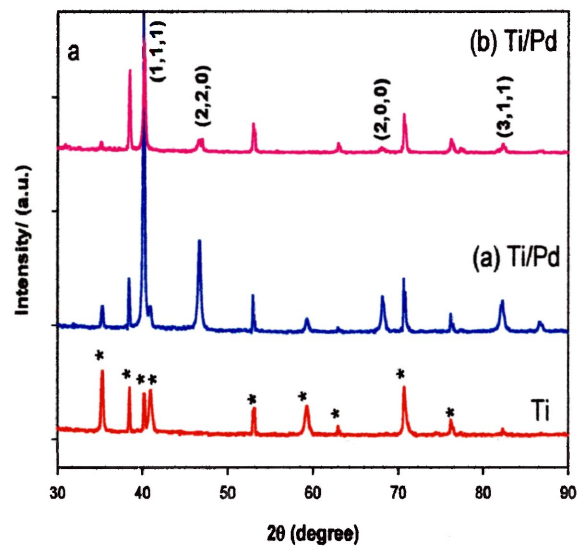


Fig. 4.2 (a) XRD patterns of the Ti/Pd before and after 3000 cyclic voltammograms; (b) XRD patterns of the $\text{TiO}_2\text{ NT}/\text{Pd}$ before and after 4000 cyclic voltammograms, peaks from TiO_2 and Ti substrates marked with asterisks (*).

metal ions into metals. The size of palladium particles that were deposited on the titanium substrate by the hydrothermal method (Fig. 4.1 (c)) were much larger than those deposited onto the TiO₂ NTs. EDS spectra of the two samples before and after deposition (Fig. 4.1d) shows that the palladium was successfully incorporated into the substrates. XRD patterns were utilized to identify the lattice constant and to quantify the average particle size. Comparative XRD patterns for the Ti/Pd and TiO₂ NT/Pd are presented in Fig. 4.2a and Fig. 4.2b, respectively. The XRD patterns indicate that all of the peaks, except those arising from the Ti and TiO₂ NT substrates (marked with asterisks (*)), may be referenced to a face-centered cubic (fcc) unit cell. For pure Pd, the 2θ values of 40.02°, 46.56°, 68.04°, and 82.05° can be indexed to the diffraction of (111), (200), (220), and (311) planes of Pd, respectively (JCPDS file no. 46-1043). The lattice constant *a* was calculated using the Bragg's equation 3.1 in Section 3.3. The lattice constant calculated for pure palladium is 0.396, which is consistent with the literature³. The median Pd particle sizes were calculated from the (200) peak using the Scherrer equation:

$$L = \frac{0.94\lambda}{\beta \cos \theta} \quad (4.1)$$

where *L* is the average crystallite size, 0.94 is a constant for small spherical particles of similar size and distribution, *λ* is the wavelength of X-ray radiation (Cu Kα = 0.15405 nm), *β* is the full width at half maximum (FWHM) in radians, and *θ* is the location of the (200) peak. The diameter of the Pd crystallite nanoparticles on the bulk Ti was 24.6 nm, while the diameter of the Pd crystallite nanoparticles on the TiO₂ NTs was 24.1 nm.

4.4 General cyclic voltammetric (CV) behaviour of the Pd nanostructures

A general characterization of the two electrodes (Ti/Pd and TiO₂ NT/Pd) in the hydrogen region was recorded in a 0.1 M perchloric acid solution. Fig. 4.3 shows cyclic voltammograms of the Pd wire, Ti/Pd and TiO₂ NT/Pd electrodes. A substantial difference between these three electrodes is evident in the hydrogen region. When the potential in cyclic voltammetric experiments is kept to an upper limit of 0.40 V, no oxidation of the palladium metal is observed. For the three electrodes, hydrogen sorption commences at different potentials. Hydrogen sorption recorded from the Ti/Pd electrode and the Pd wire occurs below 20mV vs. SCE, whereas the hydrogen region of the TiO₂ NT/Pd electrode begins at 190mV vs. SCE and a distinct hydrogen sorption peak can be observed. In addition, the peak of hydrogen desorption of palladium wire electrodes appears at -68mV vs. SCE and spans a significant range. The desorption peak of Ti/Pd is second at -145mV vs. SCE, and the peak of hydrogen desorption of the TiO₂ NT/Pd electrode starts at the more negative peak potential of -170mV vs. SCE. These results indicate that the hydrogen is more weakly bonded to the Pd nanoparticles of the TiO₂ NT/Pd electrode, and consequently the TiO₂ NT/Pd electrode exhibits faster kinetics for hydrogen desorption.

The dependence of the sweep rate on the amount of hydrogen which was absorbed into the Pd nanostructures was examined. Shown in Fig. 4.4 (a) are the cyclic voltammograms of the hydrogen region at various sweep rates for the TiO₂ NT/Pd electrode. The charge due to hydrogen desorption was calculated from the anodic portion of the curves and is displayed in Fig. 4.4 (b). Fig. 4.4 (c) depicts the H/Pd ratio, which takes the mass of the Pd coating into consideration. The amount of electrosorbed hydrogen increases considerably with a slower sweep rate from the H/Pd ratio of less than 0.32 with 30 mV/s to ~ 0.59 for 1 mV/s. In order to better study the hydrogen-sorbing capabilities of the TiO₂/Pd nanostructures and to attain the

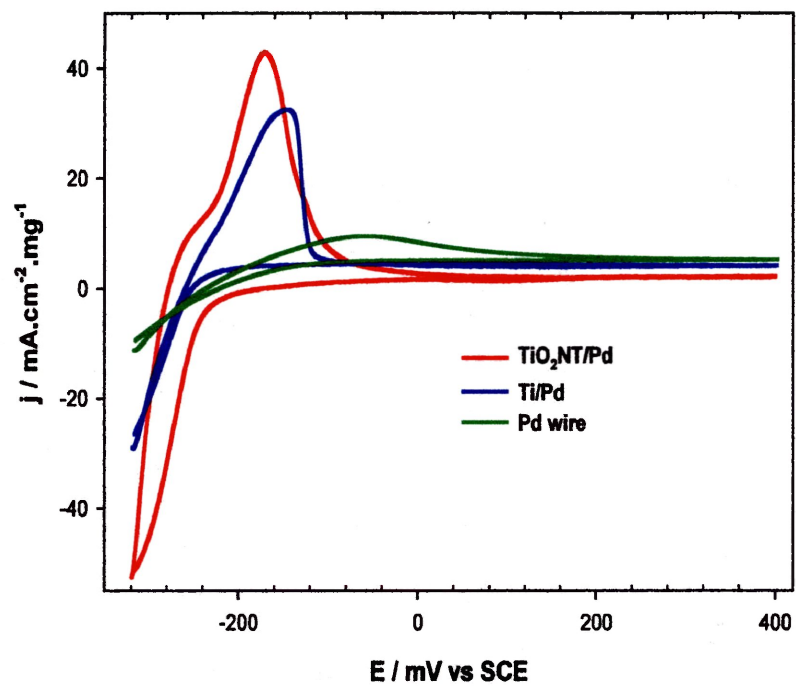


Fig. 4.3: Cyclic voltammograms of the three electrodes of (Pd wire, Ti/Pd and TiO_2 NT/Pd) in 0.1 M HClO_4 performed at a scan rate of 10 mV/s)

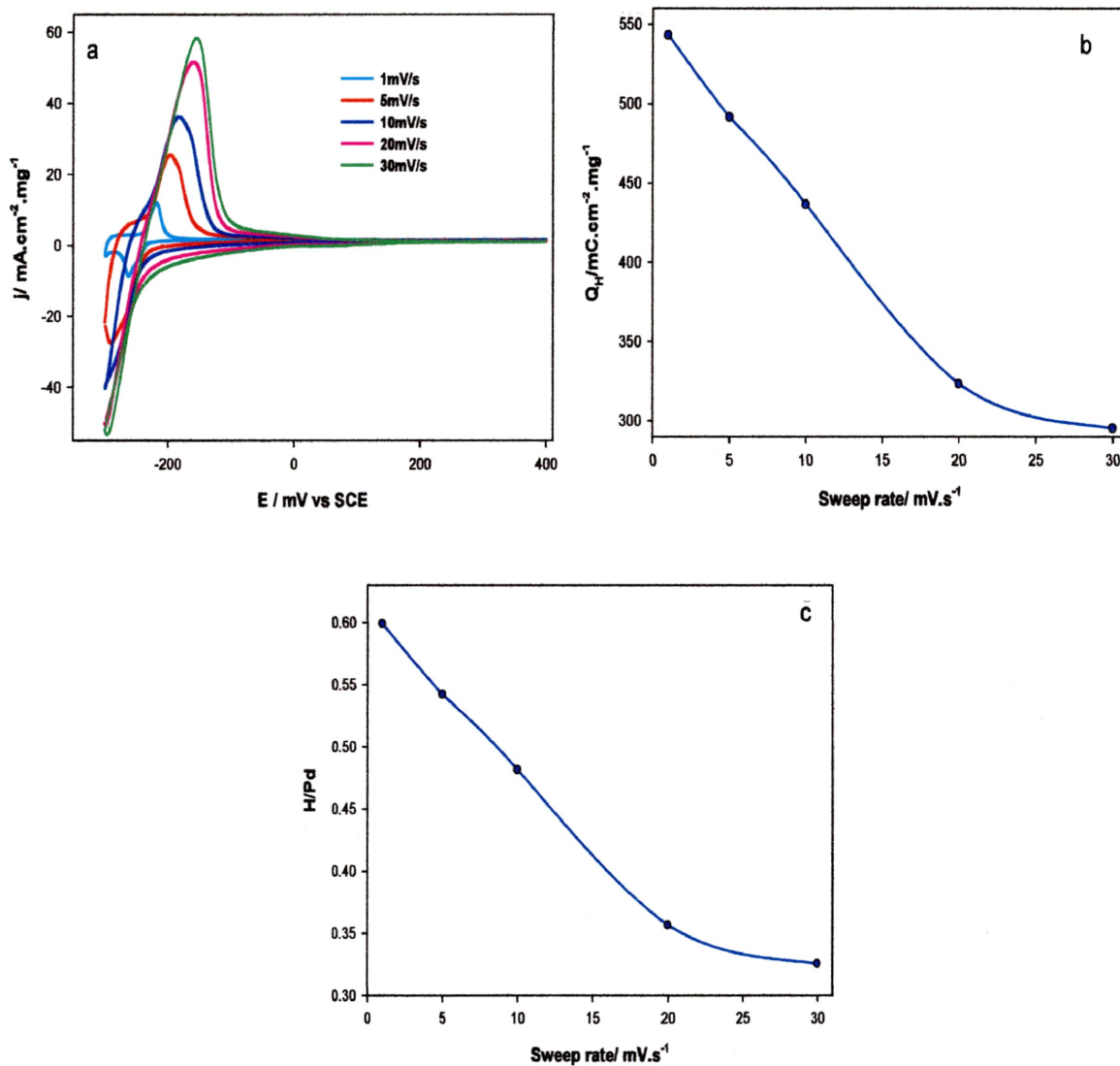


Fig. 4.4 (a) Cyclic voltammograms of TiO₂ NT/Pd in 0.1 M HClO₄ at various scan rates. (b) Charge due to hydrogen desorption versus sweep rate calculated by integrating the area under the anodic peaks in (a). (c) The H/Pd ratio versus sweep rate calculated based on the coating load of the TiO₂ NT/Pd electrode used.

maximum amount of hydrogen which may be adsorbed/absorbed, an extremely slow sweep rate is necessary. To further estimate the hydrogen capacity of the electrodes, they were saturated with hydrogen by holding a constant potential for a period of time prior to running the CVs.

The electrosorption of hydrogen into the Ti/Pd and TiO₂ NT/Pd electrodes was examined at various potentials, from -160mV to -320 mV (vs SCE). The potential was first held at a constant potential; cyclic voltammetry was run immediately afterward. The potential was held for 10 min, which was much longer than necessary to ensure the complete saturation of hydrogen. Fig. 4.5 (a) and Fig. 4.5 (b) illustrate the anodic sweeps (desorption of hydrogen) of the cyclic voltammograms of the Ti/Pd and TiO₂ NT/Pd electrodes, respectively, subsequent to their complete saturation with hydrogen at various potentials. Sharp transitions take place in the TiO₂ NT/Pd electrode at between -240 mV (vs. SCE) and -260 mV (vs SCE)), while in the Ti/Pd electrode, they are observed at between -260 mV (vs SCE) and -280 mV (vs. SCE). The volume of desorbed hydrogen at potentials more positive than -240 mV is negligible in comparison to that at -280 mV and below in both electrodes.

Anodic voltammetric scans for the oxidation of hydrogen absorbed at a constant potential (corresponding to the maximum saturation of the electrode with hydrogen) on both Ti/Pd and TiO₂ NT/Pd electrodes is depicted in Fig. 4.6. It should be noted that the potential hydrogen oxidation peak of the TiO₂ NT/Pd electrode is shifted negatively by 108mV in comparison to the Ti/Pd electrode. This means that the hydrogen removal from the TiO₂ NT supported palladium electrode is more rapid than that from the Ti supported palladium electrode. This is consistent with the results that were obtained from the cyclic voltammograms in Fig. 4.3. The possible reasons may be explained in terms of the morphology of the palladium, the substrate properties and the synthesis methods. The hydrogen desorption process can be affected by atomic scale

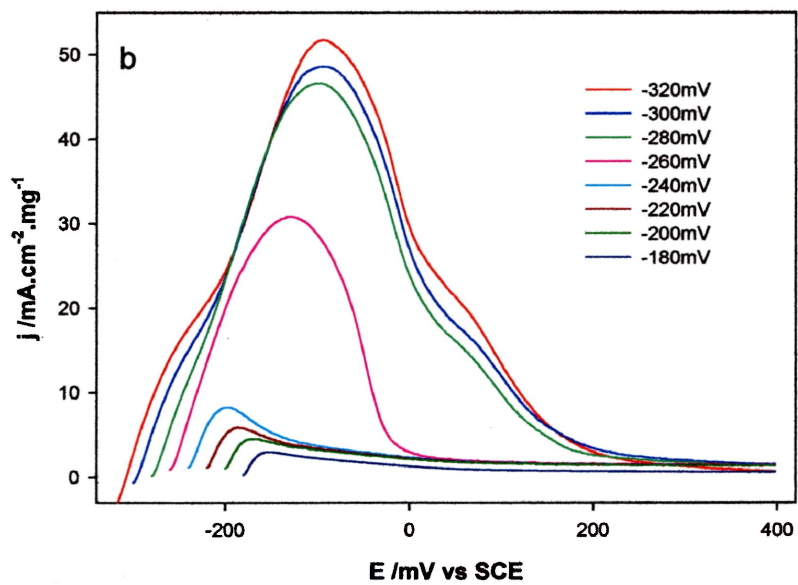
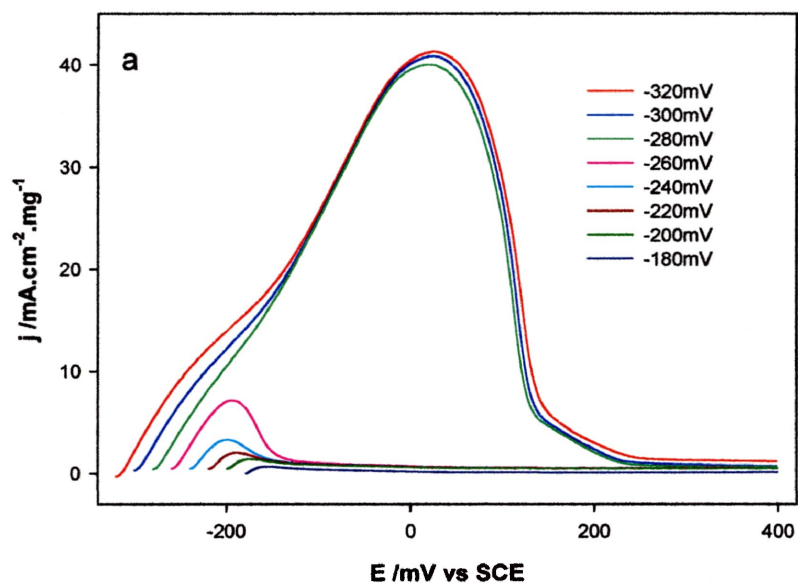


Fig. 4.5 Anodic sweeps of the desorption of hydrogen from (a) Ti/Pd and (b) TiO₂NT/Pd after holding the potential at various cathodic limits for 10 min in 0.1 M HClO₄. The scan rate was 20 mV/s.

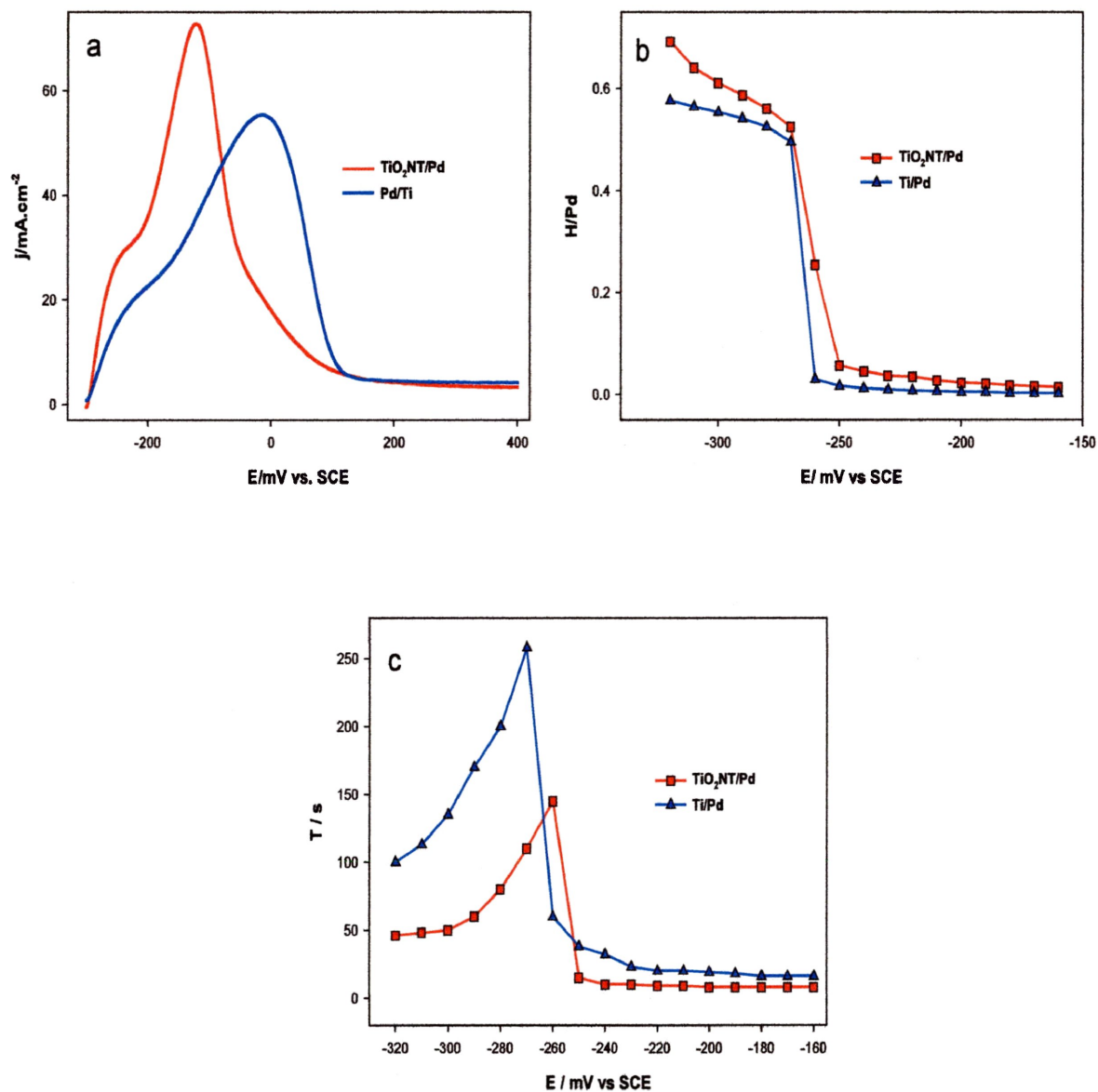


Fig. 4.6 (a): Anodic sweeps of the desorption of hydrogen from two electrodes after holding the potential at -300mV for 10 min in 0.1 M HClO_4 . The scan rate was 20 mV/s; (b): H/Pd ratio versus potential for the two samples of Ti/Pd and TiO_2 NT/Pd as indicated in the Figure. (c): Time required for obtaining steady state saturation of the two electrodes with absorbed hydrogen with respect to potential.

surface arrangements; the concentration of palladium atoms at the surface; adsorbed hydrogen-metal bond energies; as well as the palladium nanoparticle dimensions.^{2,12,32}

The volumes of hydrogen adsorbed/absorbed were determined utilizing electrochemical methods, and the results are shown in Fig. 4.6 (b). The H/Pd versus potential relationship has a characteristic shape that is determined by the forms of hydrogen present in the system. It depicts the relative amount of hydrogen absorbed (steady state value) and the H/Pd ratio, versus the absorption potential (E) for the two materials (Ti/Pd and TiO₂ NT/Pd). One can distinguish the existence of the potential regions of α and β phases, as well as the region of α - β phase transition.

The three parts of the H/Pd versus E curves recorded in Fig. 4.5 (b) correspond to various states of absorbed hydrogen. The first horizontal part for the lowest hydrogen saturation at the least negative potentials corresponds to hydrogen absorbed in the α -phase. The second horizontal section, at more negative potentials reflects full hydrogen saturation in β -phase. Both phases (α and β) of absorbed hydrogen exist in the potential range between the two horizontal parts of the H/Pd versus E curves (tilted parts of the curves). For each phase, the ratio of H/Pd of the TiO₂ NT/Pd is higher than that of the Ti/Pd electrode. Especially in the α -phase, where the volume of hydrogen stored in TiO₂ NT/Pd is four fold larger than that in the Ti/Pd electrode. The main reason for this is that hydrogen may be accumulated in the TiO₂ NTs.²²

The full saturation of the electrode was recognized when a steady-state current was attained. When the equivalent amount of palladium is deposited on the two electrodes, the time required for complete saturation (Fig. 4.6 (c)) is contingent on the applied potential and the microstructure of the electrodes. With a reduction in potential, the absorption time initially increases sharply to a maximum and then decreases. The maximum hydrogen saturation time for the Ti/Pd and TiO₂

NT/Pd occurs at potentials of -260 mV and -250mV, respectively, and corresponds to the α to β phase transition (the lowest step in hydrogen sorption process) potential in Fig. 4.6 (b).²¹ The potential that corresponds to the phase transition of the TiO₂ NT/Pd electrode is shifted to the positive direction in comparison with the Ti/Pd electrode. The hydrogen saturation time of the TiO₂ NT/Pd electrode is much shorter than that of the Ti/Pd electrode at the potentials studied in this work, which indicates that the TiO₂ NT/Pd show faster kinetics in the hydrogen sorption process.

4.5 Stability test of Ti/Pd and TiO₂ NT/Pd

Studies into the long-term stability of the TiO₂ NT/Pd and Ti/Pd electrodes were carried out by cyclic voltammetry with the corresponding results given in Fig. 4.7 (a) and Fig. 4.7 (b). The cyclic voltammetric curves for the prepared TiO₂ NT/Pd catalyst are shown in Fig. 4.7 (a). It is noted that with the increase of the cycle number (from 1 to 3000), the peak current density of the TiO₂ NT/Pd increased from 34.87 to 54.87 mA•cm⁻²•mg⁻¹ due to the fact that both the morphology and nanoparticle sizes changed simultaneously. The average size of the Pd nanoparticles on the Ti/Pd decreased from 24.6 nm to 15.5 nm, while the average size of the Pd nanoparticles on the TiO₂ NT/Pd decreased from an initial 24.1 nm to 18.3 nm. These values were calculated from the (200) peak shown in Figs. 4.2 (b) and 4.2 (c). From the 3000th to the 4000th cycle, the peak current density decreased gradually from the highest current peak density 54.87 to 53.88 mA•cm⁻²•mg⁻¹, which is still 98.20% of the maximum value. Compared to the TiO₂ NT/Pd catalyst, the peak current density of the Ti/Pd increased from 11.94 to 17.16 mA•cm⁻²•mg⁻¹ within the first 2000 cycles to gradually diminish to 15.93 mA•cm⁻²•mg⁻¹, representing 92.83% of its maximum value during the final 1000 cycles. These results demonstrate that the stability of the TiO₂ NT/Pd electrode is notably higher than that of the Ti/Pd

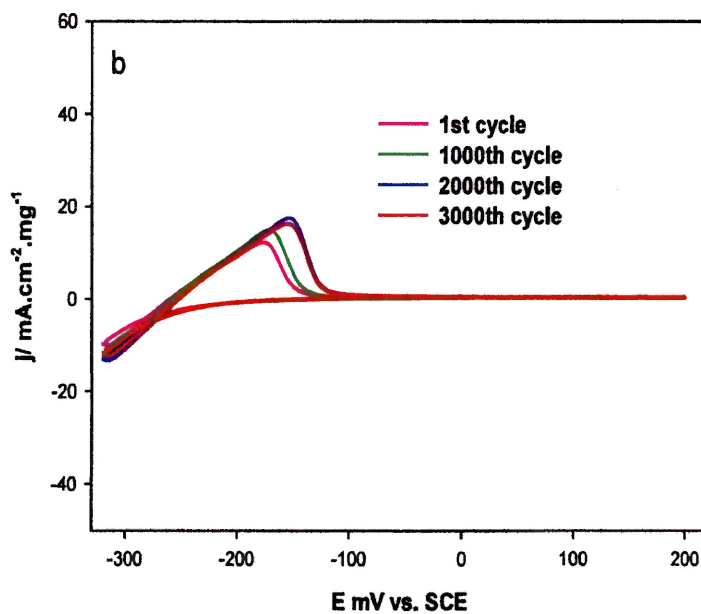
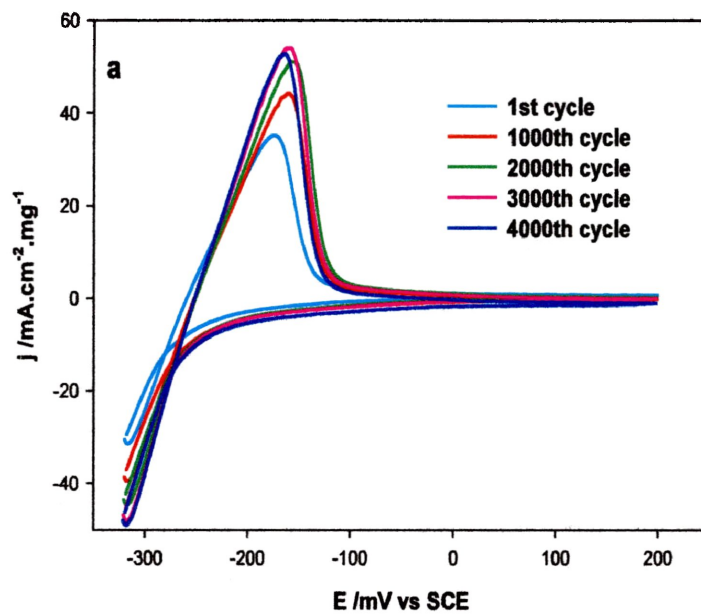


Fig. 4.7 Cyclic voltammetric curves (a) TiO_2 NT/Pd and (b) Ti/Pd in 0.1 HClO_4 at a sweep rate of 20mV/s at 1000 cycle intervals.

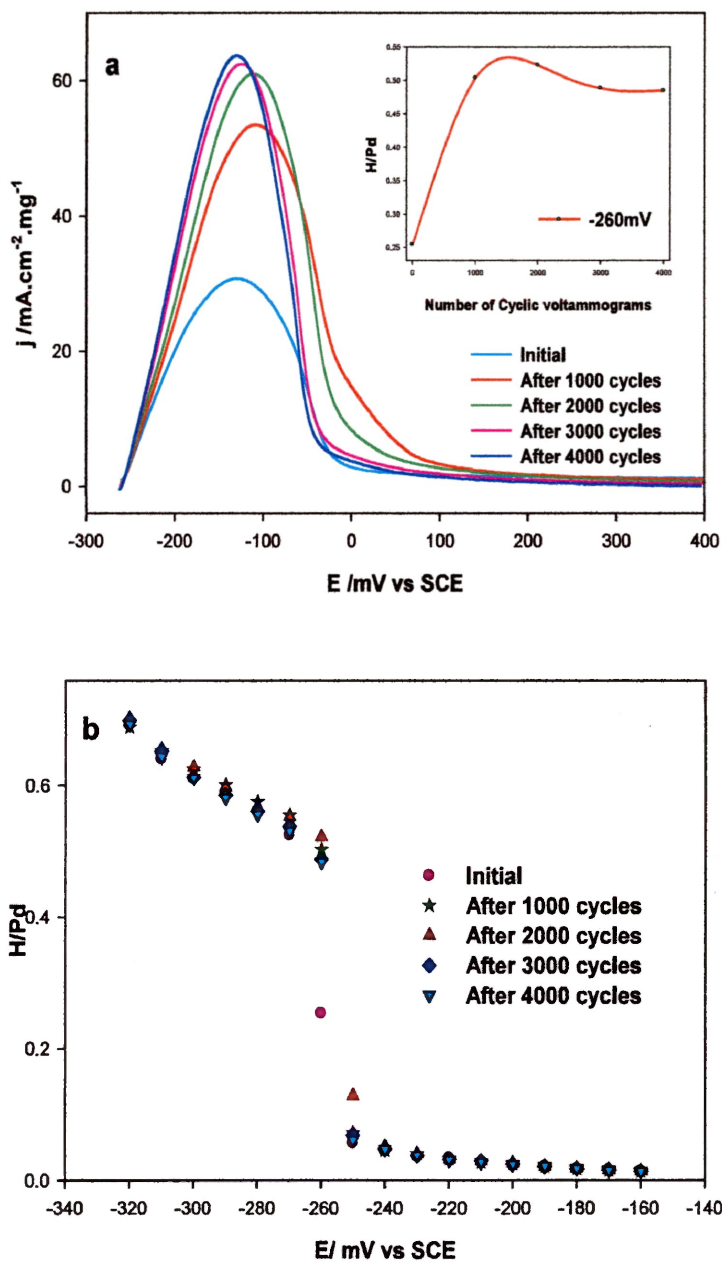


Fig. 4.8 (a) Anodic curves of the TiO_2 NT/Pd electrode for the desorption of hydrogen from -260mV vs SCE at 1000 cycle intervals after holding the potential at -260mV vs SCE for 10 min. in 0.1 M HClO_4 . The hydrogen capacity vs numbers of cyclic voltammetry is shown in the inset. (b) H/Pd ratio versus potential for TiO_2 NT/Pd at 1000 cycle intervals.

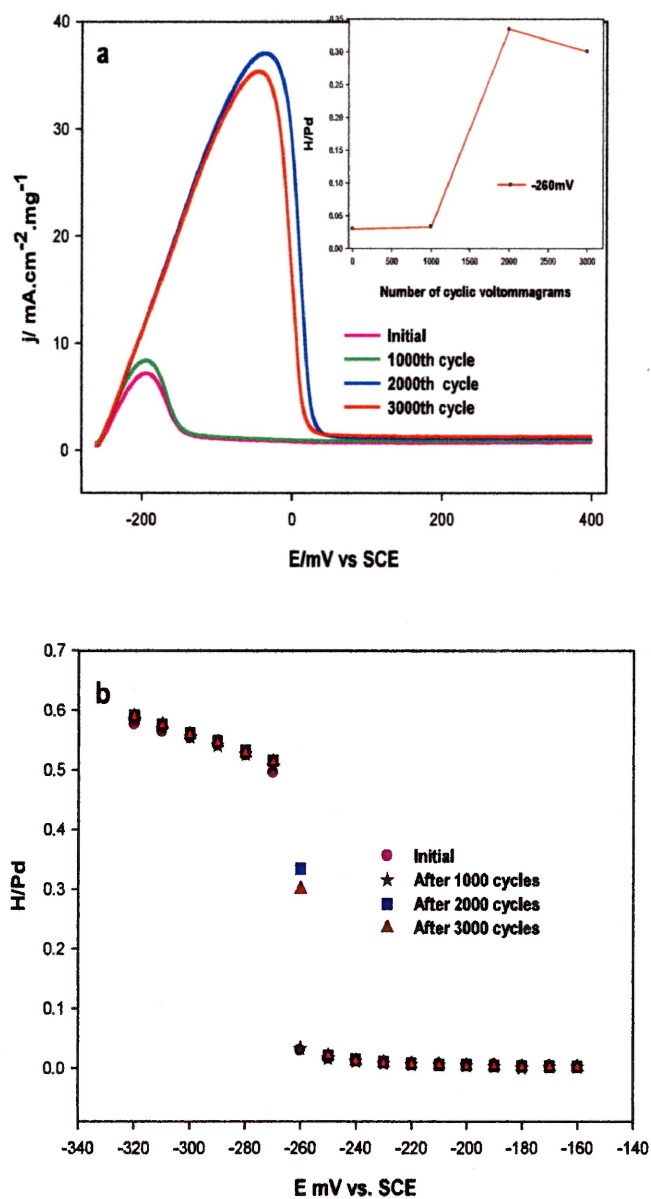


Fig. 4.9 (a) Anodic curves of Ti/Pd electrode for the desorption of hydrogen, from -260mV vs SCE at 1000 cycle intervals after holding the potential at -260mV vs SCE for 10 min. in 0.1 M HClO_4 . The hydrogen capacity of TiO_2 NT/Pd vs numbers of cyclic voltammetry is shown in the inset. (b) H/Pd ratio versus potential for Ti/Pd at 1000 cycle intervals.

electrode. The use of TiO₂ NTs as a support material exhibits appreciable electrochemical activity with improved durability, which is consistent with the results in the literature³²⁻³⁵. It should be emphasized that the maximum peak current density of TiO₂ NT/Pd electrode is 54.87 mA•cm⁻²•mg⁻¹, which is more than three times higher than that of Ti/Pd. This can be attributed to the fact that the TiO₂ NT support material has a much higher available surface area in comparison to the Ti plate substrate. The Pd nanoparticles are attached both at the top, as well as around the walls of the TiO₂ NTs. Thus, the activated surface area of the Pd on the TiO₂ NTs is significantly larger than that of the Pd on the Ti/Pd electrode.

The electrosorption of hydrogen into the TiO₂ NT/Pd and Ti/Pd during the stability test was further examined at different potentials, varying from -320 to -160mV versus SCE. The procedures were identical to those utilized in Fig. 4.5 (a). Fig. 4.8 (a) shows the anodic curve of hydrogen desorption from -260 mV to 400 mV versus SCE after hydrogen saturation at 1000 cycle intervals on TiO₂ NT/Pd. To quantitatively examine the effect of the held potential on the capacity of the hydrogen sorption into the TiO₂ NT/Pd, the total hydrogen capacity was calculated by integrating the hydrogen desorption/oxidation peak shown in Fig. 4.8 (a). As depicted in the inset, the hydrogen discharge ratio increases greatly from the initial value of 0.254 to the maximum of 0.522 after the initial 2000 cycles of scanning, which decreases slightly during the course of the following 2000 cycles.

Similarly, for the Ti/Pd catalyst, the hydrogen capacity ratio rose from 0.029 to 0.335, and then slowly decreased as shown in Fig. 4.9 (a). The electrosorption of hydrogen into the TiO₂ NT/Pd and the Ti/Pd during the stability test was further examined at different potentials varying from -320 to -160mV versus SCE. The total hydrogen discharge was calculated by integrating the hydrogen desorption/oxidation peak shown in Fig. 4.9 (a), depicted in the inset. Figs 4.8 (b) and

4.9 (b) presents the dependence of the electrochemically measured hydrogen absorption capacity, expressed as the integrated hydrogen/palladium ratio (H/Pd), on the different absorption potentials for the TiO₂ NT/Pd and Ti/Pd electrodes at 1000 cycle intervals, cyclic voltammetric scanning, respectively. It was found that initially, the hydrogen capacity increased slightly and then decreased, except at the potential of -260mV, which is similar to the results of Ti/Pd. Smaller Pd nanoparticles result in a narrower α/β phase transition³².

4.6 Conclusion

In conclusion, for the first time, the successful synthesis of an advanced material (TiO₂ NT supported palladium nanoparticles) for hydrogen storage has been achieved by means of photoreduction. The performance of the as-prepared TiO₂ NT/Pd material was compared with Ti/Pd. This study demonstrated that TiO₂ NT substrates significantly improved the properties and stability of the formed Pd nanoparticles. Electrochemical measurements show that the TiO₂/Pd nanostructures possess: (i) a higher capacity for hydrogen sorption under different potentials; (ii) faster kinetics for both hydrogen sorption and desorption; (iii) lower cost and excellent stability. The advantages listed above make TiO₂ NT/Pd attractive and useful for practical applications.

Reference

- (1) Yamauchi, M.; Ikeda, R.; Kitagawa, H.; Takata, M. *J. Phys. Chem. C* **2008**, *112*, 3294.
- (2) Kobayashi, H.; Yamauchi, M.; Kitagawa, H.; Kubota, Y.; Kato, K.; Takata, M. *J. Am. Chem. Soc.* **2008**, *130*, 1828.
- (3) Adams, B. D.; Wu, G. S.; Nigrio, S.; Chen, A. C. *J. Am. Chem. Soc.* **2009**, *131*, 6930.

- (4) Kobayashi, H.; Yamauchi, M.; Kitagawa, H.; Kubota, Y.; Kato, K.; Takata, M. *J. Am. Chem. Soc.* **2010**, *132*, 5576.
- (5) Schlapbach, L.; Züttel, A. *Nature* **2001**, *414*, 353.
- (6) Schuth, F. *Nature* **2005**, *434*, 712.
- (7) Czerwinski, A.; Kiersztyn, I.; Grden, M.; Czapla, J. *J. Electroanal. Chem.* **1999**, *471*, 190.
- (8) Sun, Y. G.; Tao, Z. L.; Chen, J.; Herricks, T.; Xia, Y. N. *J. Am. Chem. Soc.* **2004**, *126*, 5940.
- (9) Gabrielli, C.; Grand, P. P.; Lasia, A.; Perrot, H. *J. Electrochem. Soc.* **2004**, *151*, A1937.
- (10) Gabrielli, C.; Grand, P. P.; Lasia, A.; Perrot, H. *J. Electrochem. Soc.* **2004**, *151*, A1925.
- (11) Amorim, C.; Keane, M. A. *J. Colloid Interface Sci.* **2008**, *322*, 196.
- (12) Lukaszewski, M.; Czerwinski, A. *J. Solid State Electrochem.* **2008**, *12*, 1589.
- (13) Avila-Garcia, I.; Plata-Torres, M.; Dominguez-Crespo, M. A.; Ramirez-Rodriguez, C.; Arce-Estrada, E. M. *J. Alloy. Compd.* **2007**, *434*, 764.
- (14) Grden, M.; Piascik, A.; Koczorowski, Z.; Czerwinski, A. *J. Electroanal. Chem.* **2002**, *532*, 35.
- (15) Yoriya, S.; Grimes, C. A. *Langmuir* **2010**, *26*, 417.
- (16) Wang, X. M.; Xia, Y. Y. *Electrochim. Acta* **2010**, *55*, 851.
- (17) Peng, L.; Barczak, A. J.; Barbeau, R. A.; Xiao, Y. Y.; LaTempa, T. J.; Grimes, C. A.; Desai, T. A. *Nano Lett.* **2010**, *10*, 143.
- (18) Tian, M.; Wu, G. S.; Adams, B.; Wen, J. L.; Chen, A. C. *J. Phys. Chem. C* **2008**, *112*, 825.
- (19) Chen, X. C.; Hou, Y. Q.; Wang, H.; Cao, Y.; He, J. H. *J. Phys. Chem. C* **2008**, *112*, 8172.

- (20) Zurowski, A.; Lukaszewski, M.; Czerwinski, A. *Electrochim. Acta* **2006**, *51*, 3112.
- (21) Adams, B. D.; Ostrom, C. K.; Chen, A. *Langmuir* **2010**.
- (22) Bavykin, D. V.; Lapkin, A. A.; Plucinski, P. K.; Torrente-Murciano, L.; Friedrich, J. M.; Walsh, F. C. *Top. Catal.* **2006**, *39*, 151.
- (23) Huang, Y. J.; Zhou, X. C.; Liao, J. H.; Liu, C. P.; Lu, T. H.; Xing, W. *Electrochem. Commun.* **2008**, *10*, 1155.
- (24) Mor, G. K.; Kim, S.; Paulose, M.; Varghese, O. K.; Shankar, K.; Basham, J.; Grimes, C. A. *Nano Lett.* **2009**, *9*, 4250.
- (25) Varghese, O. K.; Paulose, M.; Grimes, C. A. *Nat. Nanotechnol.* **2009**, *4*, 592.
- (26) Lim, S. H.; Luo, J. Z.; Zhong, Z. Y.; Ji, W.; Lin, J. Y. *Inorg. Chem.* **2005**, *44*, 4124.
- (27) Grimes, C. A. *J. Mater. Chem.* **2007**, *17*, 1451.
- (28) Wang, J. P.; Asmussen, R. M.; Adams, B.; Thomas, D. F.; Chen, A. C. *Chem. Mat.* **2009**, *21*, 1716.
- (29) Wang, J. P.; Thomas, D. F.; Chen, A. C. *Chem. Commun.* **2008**, 5010.
- (30) Harada, M.; Einaga, H. *Langmuir* **2006**, *22*, 2371.
- (31) Tian, M.; Adams, B.; Wen, J. L.; Asmussen, R. M.; Chen, A. C. *Electrochim. Acta* **2009**, *54*, 3799.
- (32) Yamauchi, M.; Ikeda, R.; Kitagawa, H.; Takata, M. *J. Phys. Chem. C* **2008**, *112*, 3294.
- (33) Zhang, J.; Sasaki, K.; Sutter, E.; Adzic, R. R. *Science* **2007**, *315*, 220.
- (34) Bayrakceken, A.; Cangul, B.; Zhang, L. C.; Aindow, M.; Erkey, C. *Int. J. Hydrog. Energy* **2010**, *35*, 11669.
- (35) Selvaganesh, S. V.; Selvarani, G.; Sridhar, P.; Pitchumani, S.; Shukla, A. K. *J. Electrochem. Soc.* **2010**, *157*, B1000.

Chapter 5 Electrocatalytic activity of Pt–Au nanoparticles supported on TiO₂ nanotube arrays

5.1 Introduction

Direct formic acid fuel cells have attracted considerable attention because of the advantages of formic acid over methanol as an electrolyte.¹⁻⁸ First of all, formic acid is a non-toxic liquid fuel and avoids the risk of producing hazardous by-products in the oxidation process; poisonous formaldehyde usually presents during the oxidation of methanol. In addition, formic acid possesses lower penetration efficiency through the Nafion membrane than methanol due to the repulsion between HCOO⁻ and SO³⁻ ions.⁸ Furthermore, although the volumetric energy density of formic acid (2086Wh/L) is lower than that of methanol (4690Wh/L), highly concentrated formic acid can be used as fuel (e.g. 20M) to compensate the setback.⁷ From the economic point of view, electro-oxidation of formic acid commences at a more negative potential compared with that of methanol, which would yield a huge reduction in cost in the case of large scale applications.⁸⁻⁹ Finally, formic acid itself is an electrolyte, it can thus facilitate proton transport within the anode compartment.⁷

Recent studies show that the electrocatalytic activity of Pd for formic acid oxidation is very high as Pd catalysts, can overcome the CO poisoning effect mainly through the direct pathway.^{3,10-12} However, the high performance cannot be sustained, as Pd dissolves in acidic solution and is vulnerable towards intermediate species during constant current discharge.¹³ On the other hand, although platinum is the most active metal catalyst for the fuel cells both used as anode and cathode, it is well-known that, at room or moderate temperatures Pt is readily poisoned by

carbon monoxide, a by-product of formic acid and methanol oxidation.^{4,14-18} To date, Pt-based alloys, e.g. Pt-Ru, Pt-Au, have been considered as effective catalysts to enhance the activity and durability towards HCOOH oxidation.^{5,14,16,19-23} Au, previously deemed catalytically less active than other noble metals, has attracted much attention recently with the development of nanocrystalline Au-contained catalysts, showing appealing catalytic properties and high stabilities.²⁴⁻²⁶ Therefore, the study of bimetallic Pt-Au nanomaterials as fuel cell electrocatalysts for formic acid oxidation is of great interest and importance.

Although unsupported noble metal and noble alloy catalysts, such as Pt and Pd, were investigated to study the reaction mechanisms of electrocatalysis, supported electrocatalyst is a practical means to achieve high utilization of expensive noble metals to prolong the life time of the catalyst.²⁷⁻²⁹ Great efforts have been placed on synthesizing nano-scale noble-metal materials on inexpensive and stable substrates. Recent studies have shown that TiO₂ employed as the substrate and support exhibits great advantages due to its low cost and high stability.³⁰⁻³² Especially, the TiO₂ nanostructured materials such as nanotubes, nanowires, quantum dots, and nanofibers, have become a focus of considerable interest as they possess unique properties relevant to applications in photocatalytic functions.³³⁻³⁵ Among them, the nanomaterials with tubular structure has been considered the most suitable way to achieve larger enhancement of surface area without an increase in the geometric area. Electrochemical anodization of titanium in fluorinated electrolytes is employed in this study, which is a relatively simple process for the fabrication of highly ordered TiO₂ nanotube arrays.³⁶

Several methods have been reported in preparing the binary alloy nanoparticles deposited on TiO₂ nanotubes (TiO₂NTs), such as under-potential deposition (UPD), thermal treatment, spontaneous formation, and successive reduction.³⁷ The Pt-Au system has a positive heat of

formation, and the equilibrium phase diagram displays a large immiscibility gap below 1260 °C (critical temperature).²⁶ As a result, the Pt-Au nanomaterials with the expected compositions are difficult to prepare as homogeneous alloyed catalysts. Thus, there is great interest in developing a simple and straightforward approach to synthesizing Pt-Au nanostructures onto TiO₂ nanotubes. Photo-assisted deposition (PAD) method is a promising process of controlling the mean sizes of the alloy particles and synthesizing homogeneous alloy catalysts.³⁸⁻³⁹

In this study, highly ordered TiO₂NTs were fabricated by anodization as a support for Pt and Pt-Au electrocatalysts. For the first time, the photo-assisted deposition method was employed to prepare a series of Pt-Au nanoparticles dispersed on TiO₂NTs at room temperature. The compositions of the as-synthesized face centered cubic (fcc) Pt-Au alloys were easily controlled by using this method. The physicochemical properties of the Pt-Au electrodes were evaluated by scanning electron microscopy (SEM), X-ray energy dispersive spectrometry (EDS) and X-ray diffraction (XRD). The electrocatalytic properties of the Pt-Au with different compositions were investigated and the electro-oxidation of formic acid was studied. Impedance measurements of formic acid oxidation on Pt-Au were also performed.

5.2 Experimental section

A series of Pt-Au nanoparticles with different compositions were synthesized and directly dispersed onto TiO₂NTs substrates by the photo-assisted reduction process as described in Chapter 2.²⁵ To fabricate the Pt-Au nanoparticles, 0.13M of each inorganic precursor was made by dissolving 0.6732g of H₂PtCl₆•6H₂O in 5mL of ultrapure water and 0.5137g of AuCl₃•xH₂O in 5mL of ultrapure water, respectively. Pure Pt and four normalized composition ratios of Pt-Au (Pt:Au=3:1, 2:1, 1:1 and 1:2) deposited on TiO₂NTs were made. The desired compositions were made by mixing the appropriate volume ratio of each precursor together and the total volume for

the Pt and Au precursors was 40 μ L. The mixture solution of H₂PtCl₆•6H₂O and AuCl₃•xH₂O and 5mL of 50% (w/w) methanol was first deaerated for 20min. with ultrapure argon gas prior to measurements to remove any dissolved oxygen, and then was irradiated by Ultraviolet for 30min. This procedure was repeated three times. The electrode was finally removed from the light, rinsed with ultra pure water and dried in a vacuum oven at 40°C.

The surface morphology of the fabricated samples was characterized using a JEOL JSM 590LV SEM. Surface composition was investigated by and Oxford Links ISIS energy dispersive X-ray spectrometer as well as XPS for the Pd-Ag(20%) sample. The XRD patterns of the as-prepared samples were recorded using a Philips PW 1050-3710 Diffractometer with Cu K α radiation.

The reference electrode was a saturated calomel electrode (SCE) connected to the cell through a salt bridge composed of potassium chloride. All fabricated TiO₂NT/Pt-Au electrodes were used as the working electrodes. An electrolyte of 0.5M H₂SO₄ was used to examine the hydrogen sorption and desorption behaviors of the electrodes and an electrolyte of 0.1M HCOOH and 0.5M H₂SO₄ was used to investigate the formic acid oxidation activity of the electrodes. The electrolyte solutions were deaerated with the continuous passage of ultra-pure Ar gas into the electrolyte before electrochemical measurements and over the top of the electrolyte during electrochemical measurements. Electrochemical methods used in this work included cyclic voltammetry (CV), linear sweep voltammetry (LSV), chronoamperometry (CA), and electrochemical impedance spectroscopy (EIS). The chronoamperometric measurements were carried out by initially holding the potential at 0mV for 30 seconds, then stepping to various potentials for 600 seconds. The amplitude of modulation potentials for EIS measurements was 10mV, and the frequency was changed from 40kHz to 40mHz.

5.3 Surface morphology and compositions of Pt-Au catalysts

The surface morphology and composition of the synthesized TiO₂NTs substrates and Pt-Au alloys deposited on the TiO₂NTs were examined by SEM at a magnification of 10,000 and energy dispersive X-ray spectroscopy. Fig.5.1a shows that high-density, well-ordered, and uniform TiO₂NTs were directly grown on the titanium substrate by the electrochemical anodic oxidation technique. The tops of the tubes were open and the diameters of these nanotubes ranged from 60 to 90 nm with wall thicknesses of about ~10 nm and lengths of 1-2 μm. SEM images of Pt and Pt-Au33% dispersed on TiO₂NTs are shown in Fig.5.1b and 5.1c, respectively. Very small Pt particles were uniformly dispersed on the TiO₂NTs (Fig.5.1b) while larger Pt-Au alloy particles formed (Fig.5.1c). This is because Pt prefers to form single crystal seeds due to its chemical nature,⁴⁰ while the Pt-Au33% nanoparticles tend to congregate. The EDS spectra of five different ratios of the Pt-Au electrodes are shown in Fig.5.1d. The atomic ratios of Pt to Au are 74:26, 66:34, 51:49 and 34:66 for the four electrodes, which are close to the setting ratio of Pt to Au in their precursor concentrations of 3:1, 2:1, 1:1 and 1:2, described as Pt-Au25%, Pt-Au33%, Pt-Au50% and Pt-Au67%, respectively. The results indicate that the Pt-Au alloy can be successfully synthesized and the composition of Pt and Au in the alloy can be effectively controlled by using the photo-assisted deposition method.

X-ray photoelectron spectroscopy (XPS) was performed to analyze the surface composition and the electronic interaction of the Pt-Au nanoparticles dispersed on the TiO₂NTs. Fig.5.2a displays the Pt (4f) regions of XPS spectra of the pure Pt and Pt-Au catalysts. The binding energies of Pt (4f_{7/2}) and Pt (4f_{5/2}) and the Pt (4f) peaks shifting for the Pt-Au catalysts were observed in Fig.5.2a. It was found that both peaks of Pt (4f_{7/2}) and Pt (4f_{5/2}) shift negatively by ca. 0.18eV for Pt-Au33% and ca. 0.40eV for Pt-Au50% compared with the pure Pt. The negative shift of Pt (4f)

peaks is indicative of the lowering of Pt binding energy due to the addition of Au and implies that electron transfer occurs from Au to Pt. Therefore, the addition of Au modifies the electronic structure of Pt and produces an electronic effect. Fig.5.2b and 5.2c show the high resolution XPS spectra for Pt (4f) and Au (4f) of the sample Pt-Au33%. The spectrum of Pt (4f) shows a doublet peak located at a low binding energy ($4f_{5/2}$) at 74.35eV and at a high binding energy ($4f_{7/2}$) at 71.02eV (Fig.5.2b), indicating the presence of Pt in the metallic state Pt^0 and higher oxidation states. The binding energies of the Au ($4f_{5/2}$) and Au ($4f_{7/2}$) peaks (Fig.5.2c) were measured at 87.76eV and 84.09eV, respectively. It was found that 91.2% of Pt is in its metallic state and almost 100.0% of Au is in its metallic state, showing that the photo-assistant deposition method can effectively reduce Pt and Au precursors. The actual atomic composition of Au was also estimated based on the area under the peaks to be 31.5%, which is very close to the nominal ratio 33.3% of Au in Pt-Au33% electrode.

X-ray Diffraction (XRD) was used to characterize the internal crystalline structure of the nanostructured samples. The XRD patterns of Pt and Pt-Au and Au deposited on TiO_2 NTs are shown in Fig.5.3 The peaks marked with stars are derived from Ti substrate and the anatase phase of the TiO_2 NTs. The Pt nanoparticles (NPs) exhibit diffraction peaks at 46.4° , 67.3° and 82.0° corresponding to the characteristic (200), (220), (311) reflections of a Pt faced-centred cubic (fcc) structure (JCPDS file no. 4-0802). No separated Pt and Au peaks were shown in the Pt-Au33% and Pt-Au67% confirming the formation of Pt-Au alloys without crystalline metal phase separation. The (2 0 0) peaks of the Pt-Au nanoparticles shifting to a lower 2θ angle than that of the pure Pt nanoparticles indicates the increase in lattice constant of Pt due to the incorporation of Au atoms. The average particle sizes for the Pt were calculated from the (200) peak using the Scherrer equation (4.1) in Section 4.3.

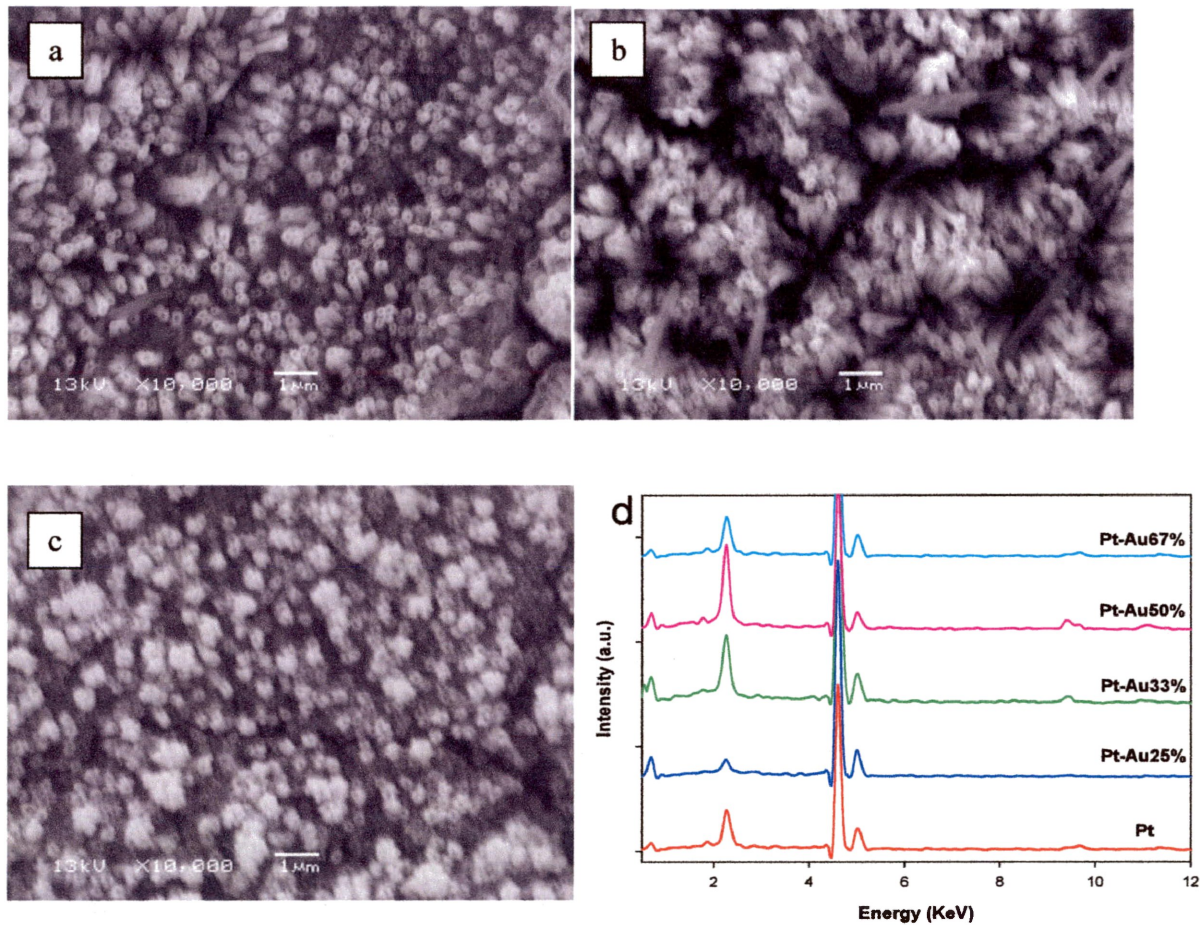


Fig.5.1 SEM images at 10,000 magnification of the TiO₂NTs, Pt and Pt-Au33% in (a), (b) and (c), respectively. (d) shows the EDS spectra of the pure Pt (red), Pt-Au25% (blue), Pt-Au33%(green), Pt-Au50%(purple) and Pt-Au67%(cyan) deposited on the TiO₂NTs substrates. The peaks labelled with * are derived from the TiO₂ NTs substrate.

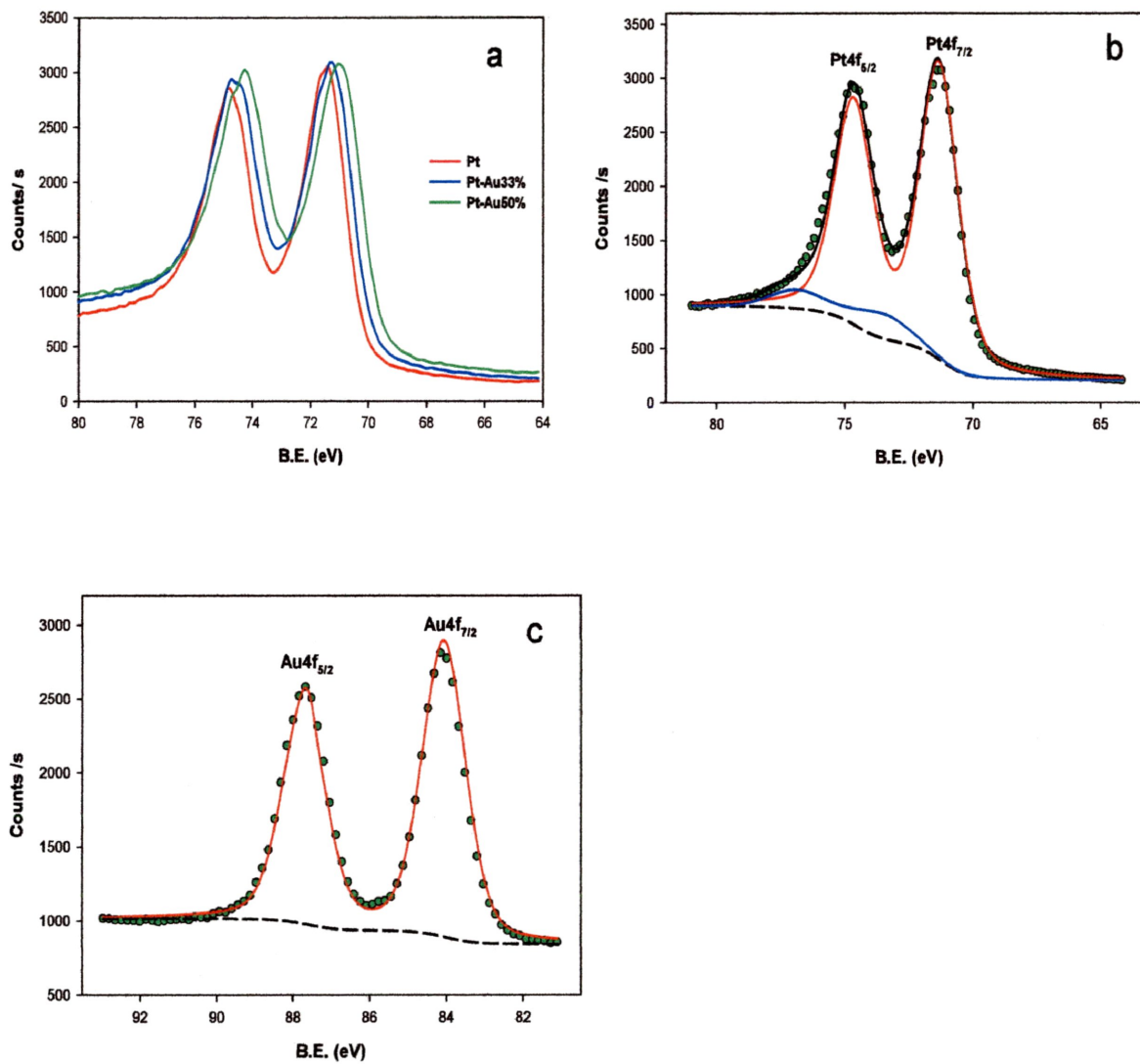


Figure 5.2. (a) XPS spectra of Pt(4f) of Pt, Pt-Au33% and Pt-Au50%. XPS spectra of the Pt (4f) (b) and Au(4f) (c) regions for the Pt-Au33% sample; the green dots, dashed lines, and red, blue, and black solid lines represent the raw data, baseline, individual components (zero and high oxidation states) and total fit, respectively.

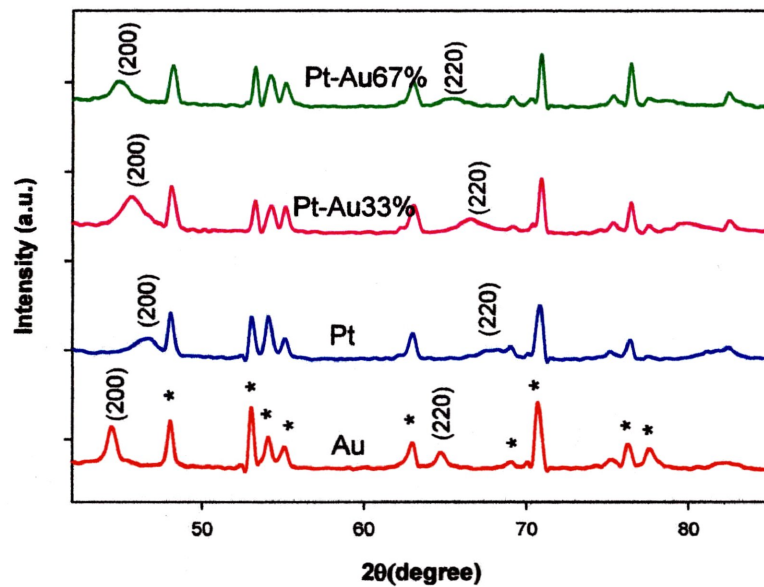


Fig.5.3 XRD patterns of pure Pt, pure Au, Pt-Au33% and Pt-Au67% deposited on the TiO₂NTs. The peaks marked as stars are derived from the Ti substrate and the anatase phase of the TiO₂ NTs.

Herein, the θ is chosen to be the location of the (200) peak. The reason for choosing the Pt (200) is that the Pt (220) is interfered by the substrate and the peak is weaker. The average crystallite sizes of Pt, Au, Pt-Au33%, and Pt-Au67% nanoparticles formed on the Ti/TiO₂NTs substrates are 22.3, 38.7, 15.7 and 19.4nm, respectively.

5.4 Electrochemistry of the Pt and Pt-Au nanocatalysts

The electrochemical characterization of as-synthesized nanocatalysts was carried out by running cyclic voltammetry of the Pt and Pt-Au electrodes in 0.5M H₂SO₄ at the scan rate of 20mV/s. Fig.5.4a shows the CVs of the Pt and Pt-Au nanocatalysts recorded in the range of -225mV to 600mV vs. SCE. Pt shows typical hydrogen adsorption and desorption behaviour. The similar behaviours of hydrogen adsorption and desorption can be observed with the Au composition of 25% and 33% on the Pt-Au alloys. With further increment of the compositions of Au from 50% to 67%, the two pairs of hydrogen adsorption and desorption peaks become obscure. Increasing the compositions of Au in the alloys results in the diminishing of the peak current of hydrogen adsorption, which indicates smaller electroactive surface area of hydrogen adsorption and desorption was obtained as Au does not absorb hydrogen in this situation.²³

Fig.5.4b shows CVs of the Pt, Pt-Au33% and Pt-Au67% in 0.5M H₂SO₄ solution with the long potential range recorded from -225mV to 1350mV vs. SCE. The reduction peaks at 900mV vs. SCE shown in Pt-Au33% and Pt-Au67% confirm the presence of Au. The peaks at 440mV for the three electrodes verify the existence of Pt. The reduction current of the Au oxide decreases while the reduction current of the Pt oxide increases as the amount of Pt increases. The decrease in the reduction current density at the potential of 440mV and the increase in the reduction current density at the potential of 900mV with the increasing amount of Au in the nanoparticle

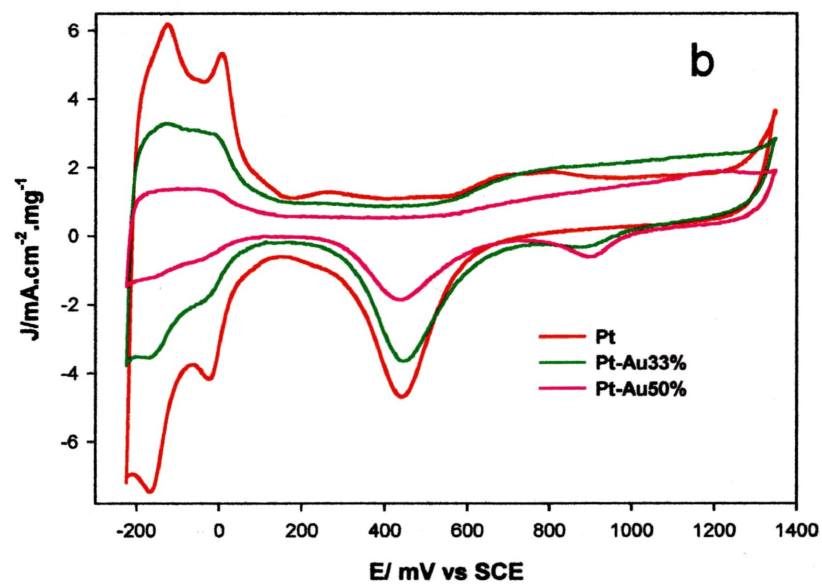
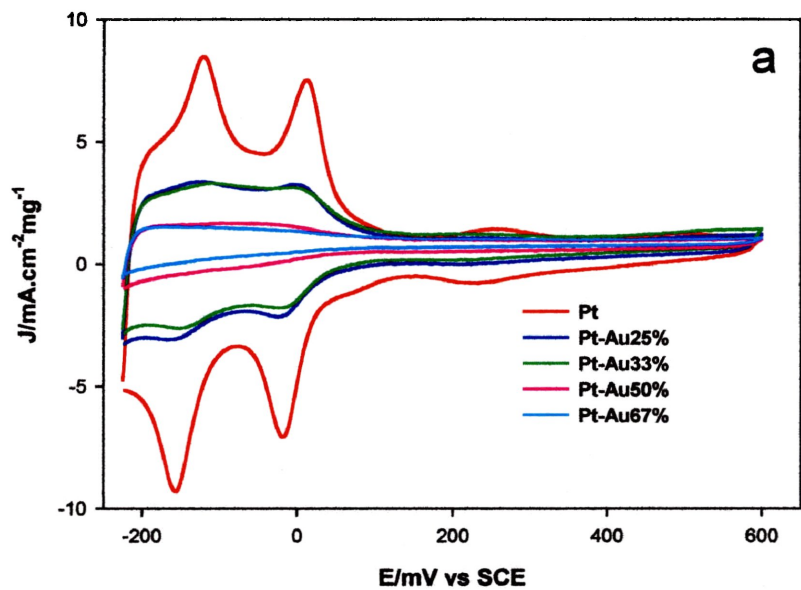


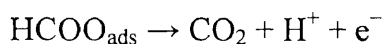
Fig.5.4. Short range (a) and long range (b) cyclic voltammograms of different ratios of the Pt-Au electrodes in 0.5M H_2SO_4 at a scan rate of 20 mV/s.

materials further prove the existence of Au in alloys.

5.5 Electro-oxidation of formic acid on Pt and Pt-Au

The catalytic activity of the Pt and Pt-Au electrocatalysts was investigated towards formic acid oxidation. There are dual pathways for formic acid oxidation: a dehydrogenation pathway (direct pathway) and a dehydration pathway (Indirect pathway).⁴

I: Direct dehydrogenation producing CO₂.



II: Dehydration generating CO (poisoning intermediate).

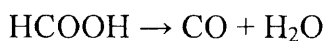


Fig.5.5 shows the linear sweep voltammograms of the Pt and Pt-Au electrodes in a 0.1M HCOOH and 0.5M H₂SO₄ solution at a potential scan rate of 20mV/s. The overall current density is normalized by the total mass of the Pt and Au load on the TiO₂NTs. It can be observed that there are two peaks for each electrode: peaks (P1) near 370 mV and peaks (P2) near 630mV. The first anodic peak at near 370mV corresponds to formic acid oxidation via the direct pathway, while the second peak near 620mV can be mainly attributed to formic acid oxidation via the indirect pathway.² For the Pt electrode, peak current density (P2) is higher than that of peak 1, which indicates that formic acid oxidation on this electrode is mainly through the indirect

pathway and thus produces undesirable intermediate CO. However, the peak current densities at 370mV for each of the Pt-Au are higher than that at 630mV, indicating that direct pathway dominates the overall oxidation process. In addition, the onset potential of HCOOH oxidation on the Pt catalyst is about 50 mV vs. SCE, while those on the Pt-Au33% and Pt-Au50% catalyst negatively shifted to about -50 mV vs. SCE. Au-based alloys have been suggested as promising materials for the enhancement of formic acid oxidation by reducing poison formation due to the “third body effect”, which is based on the role of a second metal in blocking the surface sites for a side reaction that generates poisonous species, or in blocking the adsorption of the inhibiting species, which requires more than one surface site for adsorption.^{9,41} Another possible reason could be the electronic modification of Pt which results in the strong interaction of HCOOH with Pt. After the incorporation of Au atoms, the surface electronic properties of Pt atoms could be changed, and influence the reaction kinetics and reduce the tendency to poison. Therefore, Pt-Au alloy nanoparticles could help both suppress adsorbed poisonous species and modify the strength of the surface adsorption.^{9,42}

Chronoamperometry was used to further investigate the activity and stability of the electrodes. The electrode potential was held at 0mV for 30s, and then stepped up to 100mV (Fig.5.6a) and 360mV (Fig.5.6b), respectively. In Fig.5.6a, in the curves of all catalysts, there was a sharp initial current drop, following by a slow decay. The reason for the slow decay could be attributed to the poisoning and structure change of the Pt-Au nanoparticles as a result of perturbation of the potentials during the reaction, especially in the presence of the intermediate produced during the oxidation of HCOOH.⁴³ The current density at 600s on the Pt-Au50% is found to be $5.19\text{mAcm}^{-2}\text{mg}^{-1}$, much higher than that on the Pt ($0.6\text{mAcm}^{-2}\text{mg}^{-1}$), which indicates that introduction of a certain amount of Au to the nanocomposites endows the catalyst with much higher stable current

density. In Fig.5.6b, the steady states of the currents of all the electrodes are reached in 30s. In the initial 70s, the current densities of the electrodes follow the order of Pt-Au33% > Pt-Au50%, Pt-Au25% > Pt > Pt-Au67%, which is in agreement with the results of the aforementioned CV. At the same time, the Pt-Au33% maintains the highest current density among all electrodes. This is mainly due to the more facilitative direct oxidation of formic acid on the electrode. It is worth noting that the current densities of the Pt and Pt-Au25% electrodes were continually increasing instead of slow decaying, which is different from the Pt-Au dispersed on other substrates such as carbon.^{23-24,44} At the end of the test, the oxidation current values on the Pt, Pt-Au25%, Pt-Au50% and Pt-Au67% were 22.8, 19.4, 24.1, 14.3 and 7.9 mA cm⁻² mg⁻¹, respectively. Fig.5.6c shows the chronoamperometric curves (*i-t*) on the Pt-Au33% electrode at different potentials. The steady state current density first reaches the highest value at the potential of 360mV. This result, combined with cyclic voltammetry (CV) measurements above, further confirms the superior catalytic activity and stability of Pt-Au33% toward HCOOH oxidation.

In order to investigate the electrochemical reaction resistance of formic acid oxidation, electrochemical resistance spectroscopic measurements were carried out. Fig.5.7 illustrates five Nyquist plots of the Pt and Pt-Au at the potential of 100mV vs. SCE in the 0.1M HCOOH and 0.5M H₂SO₄ solution, where Z_r and Z_i represent the real and imaginary components of the impedance, respectively. The equivalent circuit shown in the inset was used to fit the experimental data. R_s represents the uncompensated solution resistance, R_{ct} denotes the charge transfer resistance and CPE, defined as CPE_T and CPE_P, represents the constant phase element which takes into account formic acid adsorption and oxidation. The corresponding data

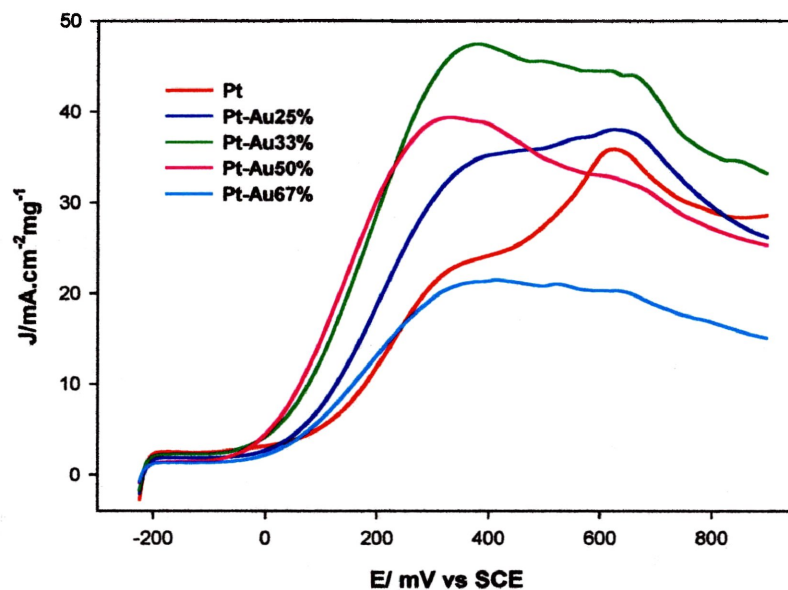


Fig.5.5 Anodic sweeps of cyclic voltammograms of different ratios of the Pt-Au electrodes in 0.5M H_2SO_4 and 0.1M HCOOH at a scan rate of 20 mV/s.

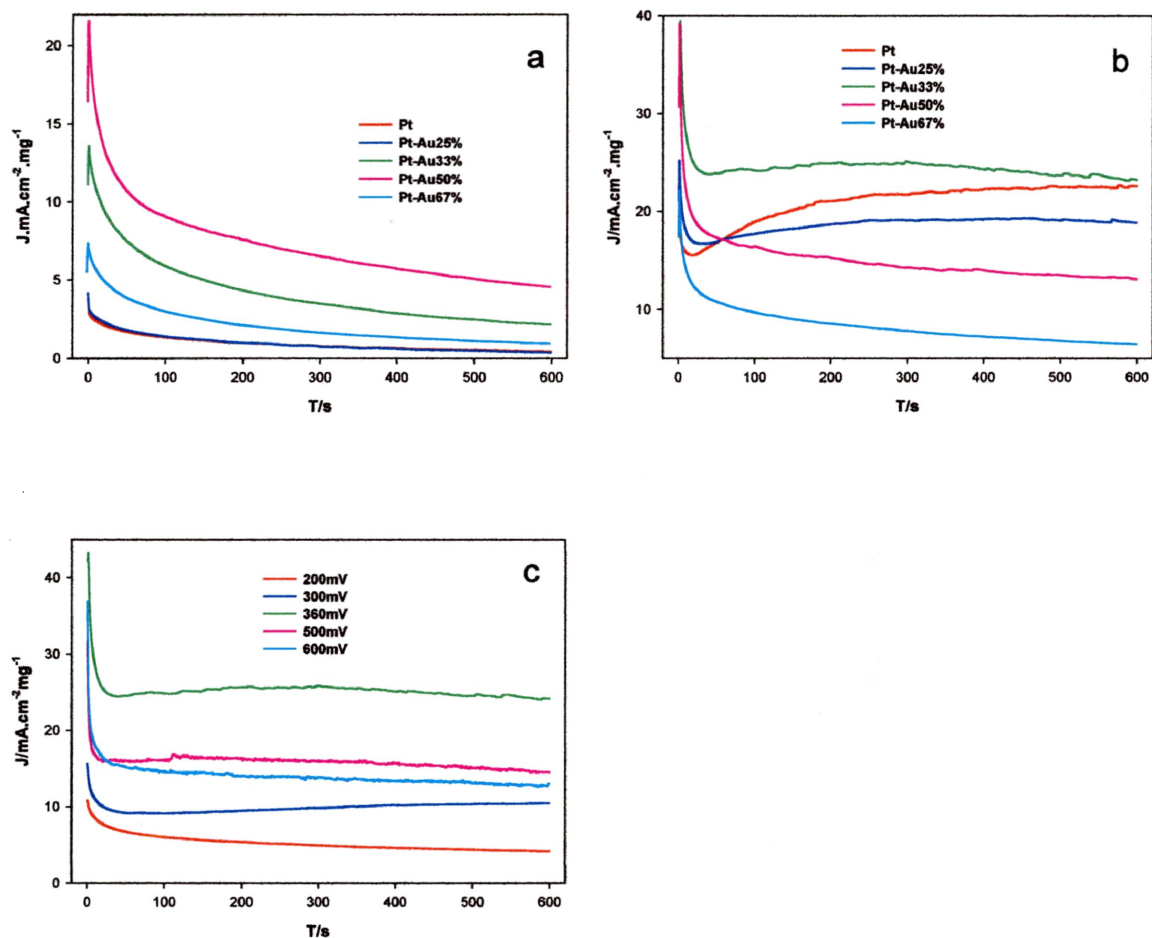


Fig.5.6. Amperometric $i-t$ curves of HCOOH electro-oxidation on the Pt and Pt-Au catalysts in 0.1M HCOOH and 0.5M H₂SO₄ at a potential of 100mV and 360 mV vs SCE shown in (a) and (b), respectively. (c) shows amperometric $i-t$ curves of HCOOH electro-oxidation on the Pt-Au33% catalysts in 0.1M HCOOH and 0.5M H₂SO₄ at different potentials.

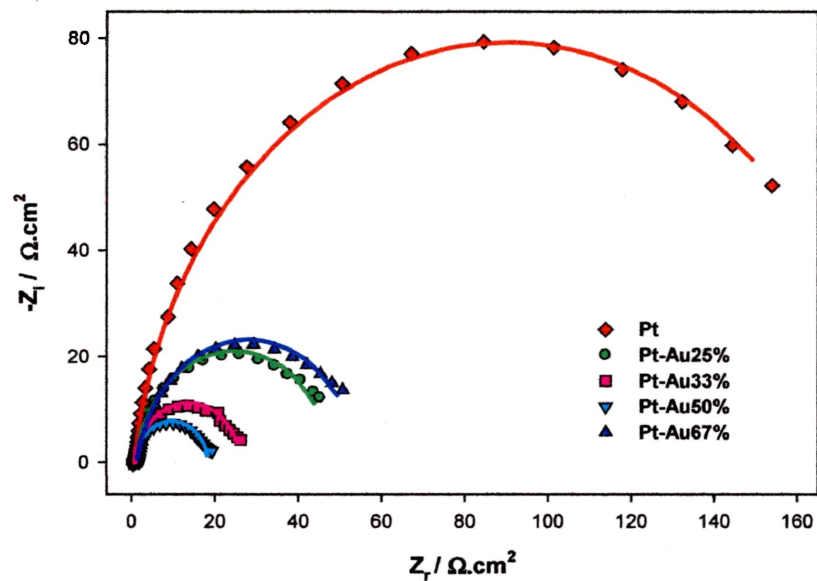


Fig.5.7 Nyquist diagrams (dotted line) of Pt and Pt-Au electrodes at a potential 100 mV in 0.5M H_2SO_4 + 0.1M HCOOH and corresponding fitted curves (solid line). The amplitude of modulation potential was 10 mV. Frequency was changed from 40 kHz to 40 mHz. The inset is the corresponding equivalent electric circuit compatible with the Nyquist diagram.

Table 5.1 Values of the elements in equivalent electric circuit fitted in the Nyquist plots of Fig.5.7

Samples	R_s (Ωcm^2)	R_{ct} (Ωcm^2)	CPE1-T	CPE1-P
Pt	0.99	171	0.0077	0.95
Pt-Au25%	0.87	43	0.0084	0.94
Pt-Au33%	0.91	25	0.0095	0.93
Pt-Au50%	0.75	18	0.0069	0.92
Pt-Au67%	1.47	53	0.0080	0.91

for each element is listed in Table 1. R_s is in the range ca.0.75-1.47 Ωcm^2 at different potentials due to the same supporting electrolyte. As shown in Fig.5.7, the proposed model fits the EIS data very well. Additionally, Pt-Au50% has the lowest charge transfer resistances, approximately 18 $\Omega\cdot\text{cm}^2$, which is 10 times smaller than that of Pt (171 $\Omega\cdot\text{cm}^2$). These results demonstrate that the synthesized Pt-Au exhibits much higher activity compared to the Pt.

5.6 Conclusion

In summary, novel TiO_2NTs supported Pt-Au nanoparticles have been successfully synthesized by anodization followed by photo-assisted deposition. This synthesis method has allowed easy and relatively precise control of the compositions of the Pt-Au nanoparticles. The XRD results show that Pt-Au bimetallic alloyed structures have been formed and the small average sizes of the particles in the Pt-Au alloys have been obtained. Electrochemical studies show that, compared to pure Pt, the fabricated Pt-Au33% electrode exhibits not only a more negative onset potential but also a higher current density for formic acid oxidation. In the EIS, these two electrodes show very smaller charge transfer resistances and a much higher activity for formic acid oxidation.

References

- (1) Wang, Y. J., Wu, B., Gao, Y., Tang, Y. W., Lu, T. H., Xing, W. and Liu, C. P., *J. Power Sources*, **2009**, *192*, 372.
- (2) Liu, Z. L. and Zhang, X. H., *Electrochem. Commun.*, **2009**, *11*, 1667.
- (3) Zhang, S. X., Qing, M., Zhang, H. and Tian, Y. N., *Electrochem. Commun.*, **2009**, *11*, 2249.
- (4) Zhang, S., Shao, Y. Y., Yin, G. P. and Lin, Y. H., *Angew. Chem.-Int. Edit.*, **2010**, *49*, 2211.

- (5) Chen, C. H., Liou, W. J., Lin, H. M., Wu, S. H., Borodzinski, A., Stobinski, L. and Kedzierzawski, P., *Fuel Cells*, **2010**, *10*, 227.
- (6) Zhang, H. X., Wang, C., Wang, J. Y., Zhai, J. J. and Cai, W. B., *J. Phys. Chem. C*, **2010**, *114*, 6446.
- (7) Winjobi, O., Zhang, Z. Y., Liang, C. H. and Li, W. Z., *Electrochim. Acta*, **2010**, *55*, 4217.
- (8) Lu, Y. and Chen, W., *J. Phys. Chem. C*, **2010**, *114*, 21190.
- (9) Park, I.-S., Lee, K.-S., Choi, J.-H., Park, H.-Y. and Sung, Y.-E., *J. Phys. Chem. C*, **2007**, *111*, 19126.
- (10) Xu, W. F., Gao, Y., Lu, T. H., Tang, Y. W. and Wu, B., *Catal. Lett.*, **2009**, *130*, 312.
- (11) Lee, Y. W., Oh, J. K., Kim, H. S., Lee, J. K., Han, S. B., Choi, W. and Park, K. W., *J. Power Sources*, **2010**, *195*, 5896.
- (12) Park, I. S., Lee, K. S., Yoo, S. J., Cho, Y. H. and Sung, Y. E., *Electrochim. Acta*, **2010**, *55*, 4339.
- (13) Zhou, Y., Liu, J. G., Ye, J. L., Zou, Z. G., Ye, J. H., Gu, J., Yu, T. and Yang, A. D., *Electrochim. Acta*, **2010**, *55*, 5024.
- (14) Wang, J. P., Thomas, D. F. and Chen, A. C., *Chem. Commun.*, **2008**, 5010.
- (15) Antolini, E., Salgado, J. R. C. and Gonzalez, E. R., *Appl. Catal. B-Environ.*, **2006**, *63*, 137.
- (16) Koczur, K., Yi, Q. F. and Chen, A. C., *Adv. Mater.*, **2007**, *19*, 2648.
- (17) Chen, D. J., Zhou, Z. Y., Wang, Q., Xiang, D. M., Tian, N. and Sun, S. G., *Chem. Commun.*, **2010**, *46*, 4252.
- (18) Liu, Y., Wang, L., Wang, G., Deng, C., Wu, B. and Gao, Y., *J. Phys. Chem. C*, **2010**, *114*, 21417.
- (19) Ghosh, T., Leonard, B. M., Zhou, Q. and DiSalvo, F. J., *Chem. Mat.*, **2010**, *22*, 2190.

- (20) Park, I. S., Lee, K. S., Jung, D. S., Park, H. Y. and Sung, Y. E., *Electrochim. Acta*, **2007**, *52*, 5599.
- (21) Diaz, V., Ohanian, M. and Zinola, C. F., *Int. J. Hydrog. Energy*, **2010**, *35*, 10539.
- (22) Irissou, E., Laplante, F., Garbarino, S., Chaker, M. and Guay, D., *J. Phys. Chem. C*, **2010**, *114*, 2192.
- (23) Zhang, S., Shao, Y. Y., Yin, G. P. and Lin, Y. H., *J. Power Sources*, **2010**, *195*, 1103.
- (24) Zhang, S., Shao, Y., Liao, H.-g., Liu, J., Aksay, I. A., Yin, G. and Lin, Y., *Chem. Mat.*, **2011**.
- (25) Tian, M., Malig, M., Chen, S. and Chen, A., *Electrochem. Commun.*, **2011**, *13*, 370.
- (26) Cheng, F. L., Dai, X. C., Wang, H., Jiang, S. P., Zhang, M. and Xu, C. W., *Electrochim. Acta*, **2010**, *55*, 2295.
- (27) Wang, Y., Nguyen, T. S., Liu, X. W. and Wang, X., *J. Power Sources*, **2010**, *195*, 2619.
- (28) Shao, Y. Y., Yin, G. P., Gao, Y. Z. and Shi, P. F., *J. Electrochem. Soc.*, **2006**, *153*, A1093.
- (29) Morales-Acosta, D., Ledesma-Garcia, J., Godinez, L. A., Rodriguez, H. G., Alvarez-Contreras, L. and Arriaga, L. G., *J. Power Sources*, **2010**, *195*, 461.
- (30) Ji, X. L., Lee, K. T., Holden, R., Zhang, L., Zhang, J. J., Botton, G. A., Couillard, M. and Nazar, L. F., *Nat. Chem.*, **2010**, *2*, 286.
- (31) Zhou, Z. Y., Huang, Z. Z., Chen, D. J., Wang, Q., Tian, N. and Sun, S. G., *Angew. Chem.-Int. Edit.*, **2010**, *49*, 411.
- (32) Uhm, S., Lee, H. J., Kwon, Y. and Lee, J., *Angew. Chem.-Int. Edit.*, **2008**, *47*, 10163.
- (33) Chuangchote, S., Jitputti, J., Sagawa, T. and Yoshikawa, S., *ACS Appl. Mater. Interfaces*, **2009**, *1*, 1140.
- (34) Kar, A., Smith, Y. R. and Subramanian, V., *Environ. Sci. Technol.*, **2009**, *43*, 3260.
- (35) Liu, D., Yang, P. and Luscombe, C. K., *J. Phys. Chem. C*, **2008**, *112*, 7886.

- (36) Yoriya, S., Paulose, M., Varghese, O. K., Mor, G. K. and Grimes, C. A., *J. Phys. Chem. C*, **2007**, *111*, 13770.
- (37) Bavykin, D. V., Lapkin, A. A., Plucinski, P. K., Torrente-Murciano, L., Friedrich, J. M. and Walsh, F. C., *Top. Catal.*, **2006**, *39*, 151.
- (38) Mori, K., Araki, T., Takasaki, T., Shironita, S. and Yamashita, H., *Photochem. Photobiol. Sci.*, **2009**, *8*, 652.
- (39) Mohamed, R. M., *J. Mater. Process. Technol.*, **2009**, *209*, 577.
- (40) Xiong, Y. J. and Xia, Y. N., *Adv. Mater.*, **2007**, *19*, 3385.
- (41) Uhm, S., Lee, H. J. and Lee, J., *Phys. Chem. Chem. Phys.*, **2009**, *11*, 9326.
- (42) Luo, J., Maye, M. M., Petkov, V., Kariuki, N. N., Wang, L. Y., Njoki, P., Mott, D., Lln, Y. and Zhong, C. J., *Chem. Mat.*, **2005**, *17*, 3086.
- (43) Zhou, W. Q., Du, Y. K., Zhang, H. M., Xu, J. K. and Yang, P., *Electrochim. Acta*, **2010**, *55*, 2911.
- (44) Bai, Y.-C., Zhang, W.-D., Chen, C.-H. and Zhang, J.-Q., *J. Alloys Compd.*, **2011**, *509*, 1029.

Chapter 6 Summary and future work

Possessing unique catalytic and hydrogen absorbing properties, Pd- and Pt-based nanomaterials are considered to be the most favorable candidates for the development of PEMFC. Particularly, Pd- and Pt-based nanomaterials show great promise for hydrogen purification, hydrogen storage, and fuel cell catalysis. Two different methods, hydrothermal reduction and photo-assisted reduction, were used for the synthesis of the nanomaterials utilized in this work. All of the fabricated nanomaterials were characterized via surface analysis and electrochemical techniques. The major results obtained during the course of this M. Sc. project are summarized below.

6.1 Hydrogen Electrosorption into Pd-Ag Nanostructures

Hydrogen absorbing materials are crucial for both the purification and the storage of hydrogen. Pd and Pd-based alloys have been studied extensively for their use as both hydrogen dissociation catalysts and hydrogen selective membrane materials. It is known that the incorporation of metal atoms of different dimensions into the Pd lattice has a major impact on the hydrogen absorption process. In Chapter 3, nanoporous Pd-Ag alloys were successfully synthesized with an Ag content that varied from 0 to 40% using a facile hydrothermal method. This method is very effective and can easily control the composition of the formed Pd-Ag nanostructures. XRD analysis shows that the lattice constant of the nanoporous Pd-Ag alloys is increased relative to increases in the amount of added Ag. Electrochemical methods have been employed to systematically study the fabricated nanoporous Pd-Ag electrodes, showing that hydrogen sorption into the nanoporous Pd-Ag alloys strongly depends on both the composition of the Pd-Ag and the applied sorption potential. Hydrogen sorption into nanoporous Pd occurs in two distinct phases (α phase and β phase). The addition of Ag greatly increases the α phase hydrogen

sorption capacity and diminishes the α and β phase transition due to the dilation of the lattice constant. The nanoporous Pd-Ag alloy with a 20% silver content possesses the highest capacity for the α phase hydrogen sorption at -225 mV, which is over four fold higher than pure nanoporous Pd. Our study has also shown that the phase transition is the rate limiting step in the hydrogen absorption process and, therefore, with the addition of Ag, the speed of the kinetics can be significantly augmented. The combination of the enhanced α phase hydrogen sorption capacity and the diminishment of the α and β -phase transition makes the nanoporous Pd-Ag alloys attractive for utility in hydrogen selective membranes and for hydrogen dissociation catalysts.

6.2 Hydrogen sorption in TiO₂NT/Pd

In chapter 4, the electrochemical hydrogen sorption behaviors of Pd dispersed on TiO₂NT electrodes are investigated. Nanotubular TiO₂ may be easily synthesized via an electrochemical anodic oxidation technique. Nanotubular TiO₂ possesses a very large surface area with high stability. As an advanced material for hydrogen storage, TiO₂NT supported palladium nanoparticles, were successfully synthesized through photo-reduction. The hydrogen sorption performance of the as-prepared TiO₂NT/Pd was subsequently compared with Ti/Pd. This study demonstrates that the TiO₂NT substrate significantly improves the properties and stability of the formed Pd nanoparticles. Electrochemical measurements show that the Pd/TiO₂ nanostructures possess a higher capacity for hydrogen sorption under different potentials; faster kinetics for both hydrogen sorption and desorption as well as lower cost and excellent stability. These advantages make TiO₂ NT/Pd attractive for practical use.

6.3 Electrochemical activity of TiO₂NT/Pt-Au

In chapter 5, novel TiO₂NT supported Pt-Au nanoparticles were successfully synthesized via anodization, followed by photo-assisted deposition. This synthesis method has allowed for the easy and relatively precise control of the compositions of the Pt-Au nanoparticles. XRD results show that Pt-Au bimetallic alloyed structures were formed, and the average dimensions of the nanoparticles within the Pt-Au alloys were obtained. Electrochemical studies show that, in comparison to TiO₂NT/Pt, the fabricated TiO₂NT/Pt-Au33% electrode exhibit (i) a more negative onset potential, but also (ii) a higher current density for formic acid oxidation. In the EIS, these two electrodes exhibit (iii) markedly reduced charge transfer resistance and (iv) much higher activity for the oxidation of formic acid.

6.4 Closing Remarks and Future work

In summary, Pd-Ag nanostructures have been fabricated, and for the first time, their hydrogen electro sorption properties have been examined. The α to β phase transition was determined to be the slowest step in the absorption process, which was practically eliminated by the incorporation of 20% Ag. This resulted in the presence of higher volumes of hydrogen in the α phase region along with faster sorption kinetics.

The performance of the Pd catalyst, when combined with different substrates for hydrogen sorption has been investigated. TiO₂NT supported Pd materials have been fabricated by the anodization of a Ti plate followed by a photoreduction method. Larger hydrogen capacities and higher stabilities were obtained in comparison with bare Ti supported Pd electrodes, indicating the significant influence that substrates have on catalyst functionality.

The electrochemical activity of TiO₂NT supported Pt-Au catalysts for the oxidation of formic acid has been studied. The electrochemical catalytic activity of Pt-Au toward the oxidation of formic acid, at 34%, has been significantly enhanced.

It appears that electrochemical catalysts dominate in applications for PEMFCs. Hydrogen storage and purification remain as two significant, albeit not insurmountable challenges that are likely to delay the widespread commercial implementation of hydrogen fuel cells. Materials with high solubility will play critical kinetic roles in these applications. Specific molecular composition appears to be very important in modifying the surface structures of Pt- and Pd-alloys. Other factors, such as support materials, are also instrumental in varying the number of active sites and for stabilizing the surface structure, thus preventing metal dissolution. Future work may focus on the following aspects: (i) optimization of the geometry, composition and structure of the Pt and Pd alloys to further improve their catalytic activity and stability; (ii) further exploring new catalyst morphologies to enhance catalytic activity; (iii) development of nanostructured catalysts supported by materials with low cost and high stability to avoid noble metal dissolution; and (iv) development of cost-effective catalyst synthesis processes to meet the necessary requirements for fuel cell commercialization.